UNIVERSITY OF MICHIGAN
JUN 14 1956
CHEMISTRY LIBRARY

Journal of Research

of the National Bureau of Standards

MAY 1956

VOLUME 56 NUMBER 5

U. S. DEPARTMENT OF COMMERCE
Sinclair Weeks, Secretary
NATIONAL BUREAU OF STANDARDS
A. V. Astin, Director

MAY • 1956
VOLUME • 56
NUMBER • 5

JOURNAL OF RESEARCH
of the
NATIONAL BUREAU OF STANDARDS

PERIODICALS OF THE NATIONAL BUREAU OF STANDARDS
(Published monthly)

The National Bureau of Standards is engaged in fundamental and applied research in physics, chemistry, mathematics, and engineering. Projects are conducted in fifteen fields: electricity and electronics, optics and metrology, heat and power, atomic and radiation physics, chemistry, mechanics, organic and fibrous materials, metallurgy, mineral products, building technology, applied mathematics, data processing systems, cryogenic engineering, radio propagation, and radio standards. The Bureau has custody of the national standards of measurement and conducts research leading to the improvement of scientific and engineering standards and of techniques and methods of measurement. Testing methods and instruments are developed; physical constants and properties of materials are determined; and technical processes are investigated.

JOURNAL OF RESEARCH

The Journal presents research papers by authorities in the specialized fields of physics, mathematics, chemistry, and engineering. Complete details of the work are presented, including laboratory data, experimental procedures, and theoretical and mathematical analyses. Annual subscription: domestic, $4.00; $1.25 additional for foreign mailing.

TECHNICAL NEWS BULLETIN

Summaries of current research at the National Bureau of Standards are published each month in the Technical News Bulletin. The articles are brief, with emphasis on the results of research, chosen on the basis of their scientific or technologic importance. Lists of all Bureau publications during the preceding month are given, including Research Papers, Handbooks, Applied Mathematics Series, Building Materials and Structures Reports, Miscellaneous Publications, and Circulars. Each issue contains 12 or more two-column pages; illustrated. Annual subscription: domestic, $1.00; 35 cents additional for foreign mailing.

BASIC RADIO PROPAGATION PREDICTIONS

The Predictions provide the information necessary for calculating the best frequencies for communication between any two points in the world at any time during the given month. The data are important to all users of long-range radio communications and navigation, including broadcasting, airline, steamship, and wireless services, as well as to investigators of radio propagation and ionosphere. Each issue, covering a period of one month, is released three months in advance and contains 16 large pages, including pertinent charts, drawings, and tables. Annual subscription: domestic, $1.00; 25 cents additional for foreign mailing.

Order all publications from the Superintendent of Documents
U. S. Government Printing Office, Washington 25, D. C.

The printing of this publication has been approved by the Director of the Bureau of the Budget, May 12, 1953.

Journal of Research of the National Bureau of Standards Vol. 56, No. 5, May 1956 Research Paper 2672

Characteristics of an Image-Forming System

Roland V. Shack

Two general approaches to the analysis of an image-forming system are considered. One depends on the image of a point object and the other on the Fourier transform of this image. The two are developed independently and then coordinated, a practical characteristic function being determined for each approach. The relative merits of the two approaches are considered.

1. Introduction

For the past few years considerable energy has been expended in the search for an objective procedure for evaluating the quality of images formed by optical instruments. Existing procedures have been found to be not entirely satisfactory, and much work has been done in measuring previously unused physical parameters, which are objectively determinable, for the purpose of correlating them with the existing quality criteria.

The objection to this is that such an empirical, and therefore much limited, correlation eliminates only one of the faults of the existing criteria, and this is the subjectivity of their determination. Any other weakness is ignored.

A better approach is to analyze the image-forming process as a phenomenon, the aim being to characterize the process in as general and inclusive a way as possible, consistent with practical instrumentation. New criteria of image quality would of course be expected to be developed. Many approaches have been made in this direction also, and the present paper is to be included among them. However, in contrast to some of the published material, the emphasis here is on the practicality and usefulness of the results obtained rather than on mathematical rigor, although the treatment should be rigorous enough to include all essential factors.

Let us consider this matter of practical instrumentation. The heart of the test instrument is the photosensitive detector, for it is this which provides the data by which the tested instrument is evaluated. Three practical photosensitive detectors are available—the eye, the photographic emulsion, and the photocell.

The only test of image quality for which the eye is capable of making quantitative measurements is the resolving-power test. This test is rapid and relatively inexpensive, but the information obtained is incomplete, the precision is low, and the results are subject to variation from individual to individual.

A photographic detector allows quantitative measurements to be made under nonthreshold conditions, but time is required for processing, the processing conditions must be rigidly standardized, the granularity and diffusion in the emulsion affect the results, the response of the film is nonlinear with respect to incident flux, and, in the end, an additional sensing mechanism, such as a microdensitometer, is needed to reduce the emulsion properties to numerical values.

The photocell is probably the most satisfactory photosensitive detector for the test instrument. Within its proper operating range, its characteristics remain reasonably constant, its response is linear with respect to incident flux, its spectral response can be adjusted so as to approximate that of the eye, and its output can very easily produce graphical or numerical results. However, it must be used in conjunction with an aperture that limits the spatial integration of the detail in the image being examined, and there must be provision for relative displacement between the aperture and the image so that various portions of the image may be sampled.

It should also be pointed out that the report is illustrated throughout by the characteristics of an aberration-free system with a circular aperture in monochromatic light, diffraction being the sole source of image degradation, and the light from various points in the object space being noncoherent. This has been selected as an interesting and informative type of system, which real systems tend to approximate as their quality improves. It must be emphasized,

379949—56——1

however, that this is used for illustration only. The material covered applies to all types of images, assuming noncoherence.

There are two viewpoints from which image evaluation can be approached. One, the classical viewpoint, considers the point image to be the most fundamental element in an image process. Any object can be regarded as a summation of points, and its image as the summation of the corresponding point images. An evaluation of the point image would be sufficient to characterize the system.

The other viewpoint involves the concepts of Fourier analysis. Here the object is considered to be the summation of a set of sinusoidal waves distributed in the object plane. These component waves, differing from each other in amplitude, frequency, phase, and direction, are spatially distributed waves. That is, they are spatial, not temporal, sinusoidal variations in brightness throughout the object plane. The image consists of the summation of the images of these component waves. A description of the manner in which the optical system forms images of these component waves would also be sufficient to characterize the system.

In section 2 a way of describing the point image is developed, which can be obtained, at least in principle, from a variety of test objects, namely, a point, a fine line, a variable slit, and a knife edge. Data from any or all of these objects can be represented by a single common curve, which can be interpreted in terms of any of the objects.

Section 3 deals with the Fourier type of approach. An imaging system does not affect the frequency, direction, or sinusoidal character of the component waves. It can only affect their amplitudes and phase relationships. The function that describes these modifications as a function of the frequency and direction of the component waves is also characteristic of the imaging system. The test object required to obtain this information consists of a series of patterns in which the luminance varies sinusoidally, each pattern having a different spatial frequency and all oriented in the same direction. The directional variation can be obtained by rotating the test object with respect to the system being tested.

Section 4 is concerned with the coordination between the two viewpoints. It is shown that it is possible to obtain from either approach the characteristics for a periodic test object consisting of alternate dark and light stripes of equal width, such as is commonly used in resolving-power work. It is also shown that it is possible to transform the characteristics of either approach into those of the other.

Section 5 discusses the application to practice, the interpretation of the results and the relative merits of the two approaches.

The appendix gives the mathematical formulation of the diffraction images used as illustrations.

In the following mathematical statements, constant coefficients are ignored in the integrations unless otherwise indicated. The functions are assumed to be normalized after integration. Also, the object-plane coordinates are reduced to the image plane by application of the magnification.

2. Evaluation of the Point Image

2.1. General Image Formation with the Point Image

The point image is the flux-density distribution in the image plane when the object is a point source (figs. 1, 2). A general object can be considered to consist of a summation of points, and its image the summation of the corresponding point images.

Let $O(x,y)$ = general object function,
$\varphi(x,y)$ = point image function,
$I(x,y)$ = general image function.

Then

$$I(x',y')=\int_{-\infty}^{\infty}\int_{-\infty}^{\infty} O(x,y)\varphi(x'-x,y'-y)dxdy. \tag{1}$$

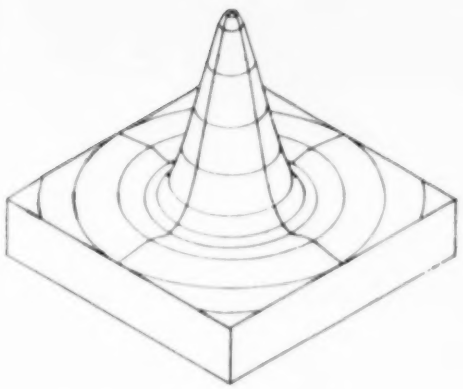

FIGURE 1. *Point-image model.*

In this model the vertical dimension represents flux density (per unit area). It is understood that the rings actually continue indefinitely, whereas only the first bright ring is shown completely.

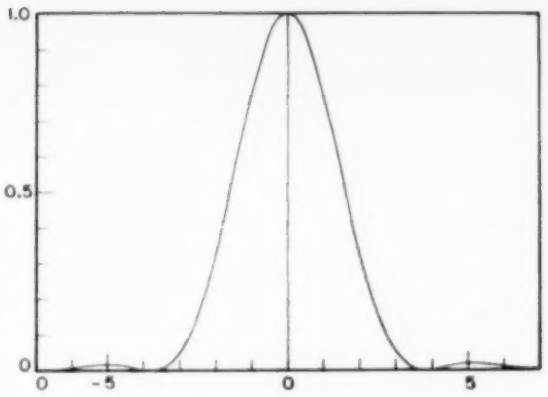

FIGURE 2. *Section of point image.*

The normalized distance in the image plane is measured in z-units, as explained in appendix 1.

The primed variables represent the displacement between the O and φ functions required for the integration. For each displacement, the integral, being a definite integral, establishes a specific value for I. The image function, I, then, is a function of the displacement involved in the integration. The space described by x',y', however, is the same as that described by x,y. O and I can be compared point for point.

The integration can also be written in such a form that the object function is the displaced function, that is,

$$I(x',y')=\int_{-\infty}^{\infty}\int_{-\infty}^{\infty}\varphi(x,y)O(x'-x,y'-y)dxdy. \tag{2}$$

Either of these forms is perfectly valid, and either may be transformed into the other, provided one recognizes that x,y in eq (1) is not the same as x,y in eq (2). To distinguish them, one might use subscripts on the symbols, but this would make the equations more confusing, and is not necessary if one understands the situation.

The image function is to be sampled with a space-integrating detector in the image plane, that is, a photocell behind an aperture.

Let $A(x,y)$ = detector aperture transmission function,
$E(x,y)$ = total flux passing through A as a function of the position of A.

Then

$$E(x'',y'')=\int_{-\infty}^{\infty}\int_{-\infty}^{\infty}I(x',y')A(x''-x',y''-y')dx'dy'. \tag{3}$$

Combining this with eq (2) we obtain

$$E(x'',y'')=\int\int\int\int_{-\infty}^{\infty}\varphi(x,y)O(x'-x,y'-y)A(x''-x',y''-y')dxdydx'dy'. \tag{4}$$

From this it can be seen that the functional characteristics of O and A can be interchanged without affecting the measured flux, E. For example, suppose the object were a point source and the aperture a circular hole centered on the point image. The output from the photocell will indicate amount of flux passing through the hole. Then interchange the object and aperture. Now the object is a uniformly luminous disk with a reduced diameter equal to that of the previous aperture, and the new aperture is a minute hole, equal in size to the reduced geometric size of the previous point source. The output from the photocell will be the same as before.

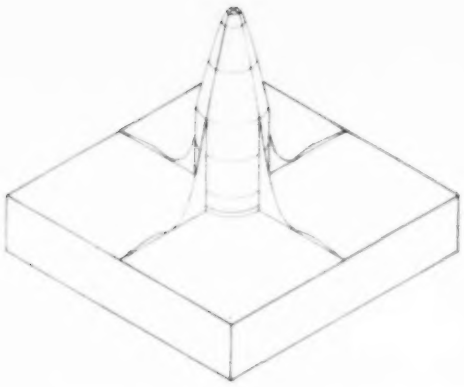

FIGURE 3. *Point-image evaluation—Hopkins' method.*

The solid represents the portion of the total flux that passes through the circular aperture.

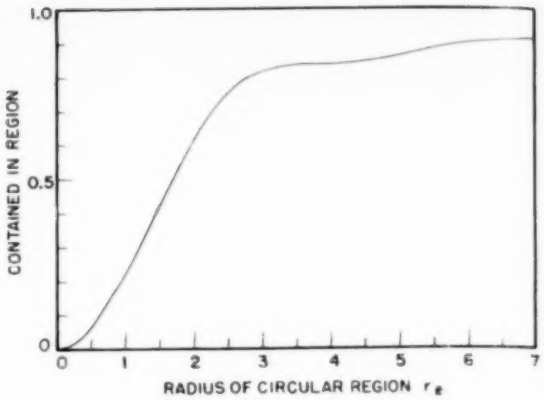

FIGURE 4. *Radial flux distribution of point image.*

This curve shows the normalized volume of the solid of figure 3 as a function of the radius of the limiting cylinder.

Mathematically, and in a more general sense, this situation is as follows: If O is a point source, then

$$E(x'',y'')=\int_{-\infty}^{\infty}\int_{-\infty}^{\infty}A(x''-x',y''-y')\left[\int_{-\infty}^{\infty}\int_{-\infty}^{\infty}\varphi(x,y)O(x'-x,y'-y)dxdy\right]dx'dy'$$
$$=\int_{-\infty}^{\infty}\int_{-\infty}^{\infty}\varphi(x',y')A(x''-x',y''-y')dx'dy', \tag{5}$$

and the flux detected depends on the nature of A.

On the other hand, if A is a point aperture, then

$$E(x'',y'')=\int_{-\infty}^{\infty}\int_{-\infty}^{\infty}\varphi(x,y)\left[\int_{-\infty}^{\infty}\int_{-\infty}^{\infty}O(x'-x,y'-y)A(x''-x',y''-y')dx'dy'\right]dxdy$$
$$=\int_{-\infty}^{\infty}\int_{-\infty}^{\infty}\varphi(x,y)O(x''-x,y''-y)dxdy, \tag{6}$$

which is identical in form with eq (5), except that A is replaced by O. If O in eq (6) had the same functional characteristics as A in eq (5), then they would be mathematically indistinguishable, and the same E will be obtained from either. Also note that eq (6) has the same form as eq (2). As one would expect, the use of a point aperture would produce an undistorted map of the flux-density distribution in the image plane.

2.2. Determination of a Characteristic Function of the Point Image

It should be clear from the above that the function which distinguishes one image-forming system from another is the point-image function φ. The problem is to find some way of describing φ, which can be obtained experimentally and which provides significant information to the user.

The direct mapping of the flux-density distribution in the image of a point object with a point aperture is impractical because of the very low-energy levels involved. A practical method must involve in some manner the integration of the flux over an area.

One method, used by Hopkins [7] [1] is to measure the flux contained within successive concentric circular regions about the center of the point image (fig. 3). The ratio of the flux contained within a circular region to the total flux of the point image is plotted as a function of the radius of the circle (fig. 4).

[1] Figures in brackets indicate the literature references at the end of this paper.

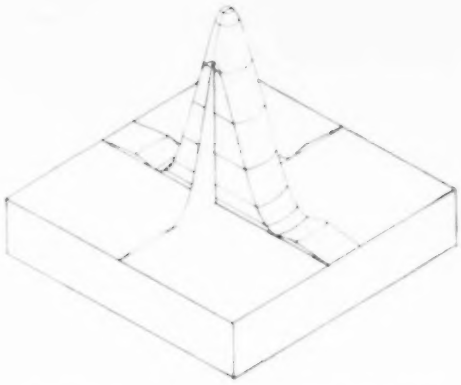

FIGURE 5. *Determination of point-image characteristic.*

The solid represents the portion of the total flux that passes through the receiver slit, the point image being centered on the slit.

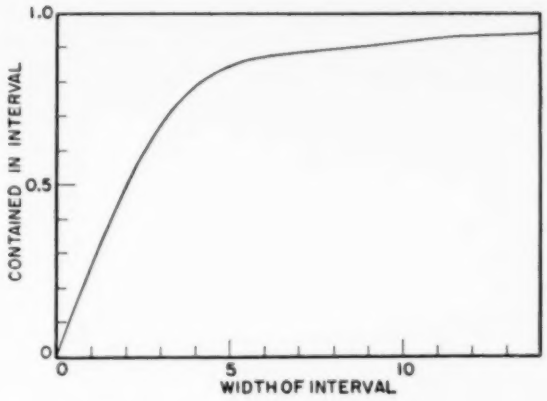

FIGURE 6. *Point-image characteristic.*

This curve shows the normalized volume of the solid in figure 5 as a function of the width of the slab.

This method has several advantages over mapping the flux-density distribution directly. Of course, there is an increase in the energy involved, which increases the signal-to-noise ratio of the measurements. Also, there is a reduction of a three-dimensional function to two dimensions, which is more convenient. Further, this method provides the user with an idea of the contrast with which small detail will be imaged, for, by the interchangeability of the object and aperture function, the resulting curve (fig. 4) can be considered to represent the flux density at the center of the image of a disk as a function of the size of the disk. This disk corresponds to a small object in the scene, later observed by the user.

This method does have disadvantages, however. It is satisfactory for systems in which the point image is radially symmetrical, but is insensitive to the presence of radial asymmetry, such as exists in an astigmatic or comatic image. It also presents the practical difficulty of locating the centers of the apertures or disks in two dimensions with precision.

A different integrative method that allows a considerable increase in the available energy is one in which the integration is limited in one direction only. This is done by measuring the flux contained in successive widths about the center of the point image (fig. 5). The normalized flux contained in a region as a function of the width of the region (fig. 6) is the function that is here proposed as the most useful and practical characteristic function describing the point image. It will hereafter be called the point-image characteristic $K(w)$, where w represents the width of the region. For example, if the integration is limited in the x-direction, then

$$K(w_x)=\int_{-w_x/2}^{w_x/2}\int_{-\infty}^{\infty}\varphi(x,y)\,dy\,dx. \tag{7}$$

It should be noticed that this function does not actually involve a reduction of three dimensions to two, because the curve obtained is a function of the direction in which the integration is taken. This makes the data somewhat less convenient than is true of the previous method, but this is not objectionable because of the additional information obtained. The new method will detect a lack of radial symmetry. However, the inconvenience involved is not too great because most images are bilaterally symmetrical, or nearly so, and two mutually perpendicular orientations are all that are necessary to characterize the image.

The point-image characteristic has other virtues beyond the relatively large amount of available energy and the ability to detect lack of radial symmetry. These arise out of the unidirectional limitation of the integration.

For example, the point-image characteristic is closely connected with the fine-line image. The fine-line image is the image of a line of infinite length but infinitesimal width. The flux density is constant along the length of the line image and varies in a direction perpendicular

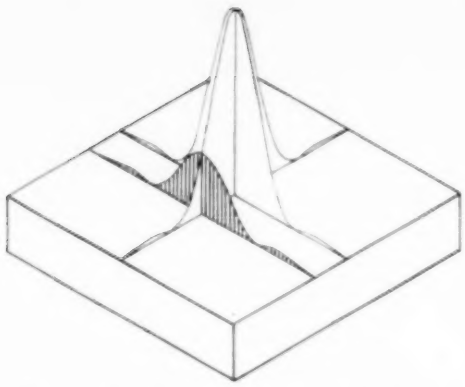

FIGURE 7. *Generation of fine-line image.*

The flux density at a point in a fine-line image is proportional to the area of the section of the point image orientated in the direction of the line.

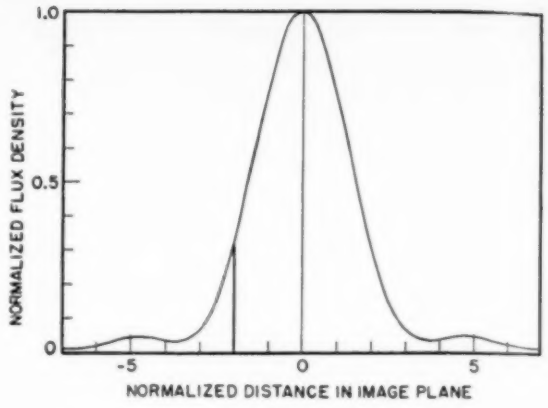

FIGURE 8. *Cross section of fine-line image.*

The vertical line corresponds to the area of the section shown in figure 7.

to the length. It is obtained by integrating the point image in one direction only. For example, the image function for a fine line, the length of which is in the y-direction, is given by

$$L(x)=\int_{-\infty}^{\infty}\varphi(x,y)dy. \tag{8}$$

This is illustrated in figures 7 and 8.

The point-image characteristic can be obtained from the fine-line image by

$$K(w_x)=\int_{-w_x/2}^{w_x/2}L(x)dx. \tag{9}$$

This is illustrated in figure 9.

Up to this point we have been considering the object to be a point or a fine line and the detector aperture to be a variable slit, the operating mechanism that produces the variation in w. But, because of the interchangeability of the object and aperture, an illuminated variable slit could be used as an object and a fine slit centered on the variable slit image as the detector aperture. This method of obtaining the point-image characteristic is illustrated in figure 10.

The point-image characteristic is also closely connected with the knife-edge image. The latter is related to the point image as follows:

$$S(x')=\int_{-\infty}^{x'}\int_{-\infty}^{\infty}\varphi(x,y)\,dydx. \tag{10}$$

This is shown in figures 11 and 12.

The relationship between the knife-edge image and the fine-line image is given by

$$S(x')=\int_{-\infty}^{x'}L(x)dx. \tag{11}$$

The point-image characteristic is obtainable from $S(x)$ by observing the values of $S(x)$ at $x=-w_x/2$ and $x=+w_x/2$. Then

$$K(w_x)=S(w_x/2)-S(-w_x/2)=\int_{-\infty}^{w_x/2}L(x)dx-\int_{-\infty}^{-w_x/2}L(x)dx=\int_{-w_x/2}^{w_x/2}L(x)dx. \tag{12}$$

These relationships are illustrated in figures 13 and 14.

In summary, it may be pointed out that the point-image characteristic provides a simple yet practical and informative way of evaluating an imaging system. It may be obtained from a variety of test objects, namely, a point, a fine line, a variable-width line, or a knife edge.

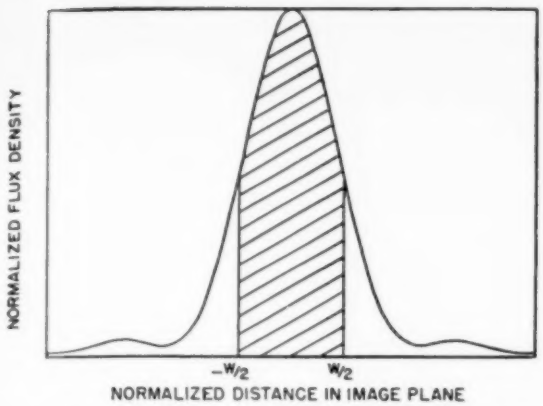

FIGURE 9. *Determination of point-image characteristic from fine-line image profile.*

The cross-hatched area corresponds to the solid in figure 5.

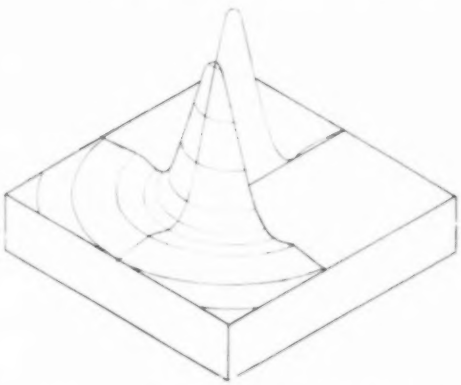

FIGURE 11. *Generation of knife-edge image from point image.*

The flux density at a point in the knife-edge image is proportional to the volume of the solid indicated where the limiting plane has the same orientation as the knife edge and passes through the point in question.

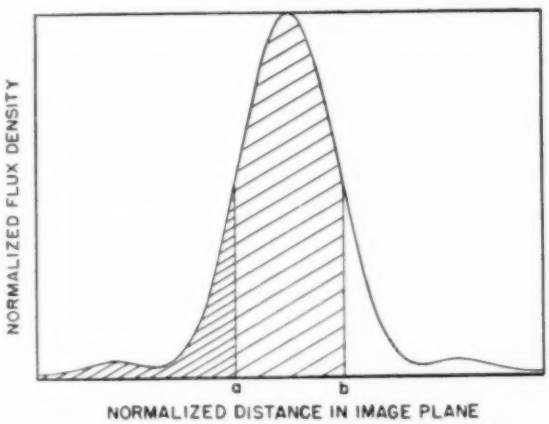

FIGURE 13. *Generation of knife-edge image from fine-line image.*

The flux density at a point in the knife-edge image is proportional to the area under the fine-line image to the left of the corresponding abscissa. The area under the fine-line image between any two abscissa values is proportional to the difference between the corresponding ordinate values of the knife-edge image.

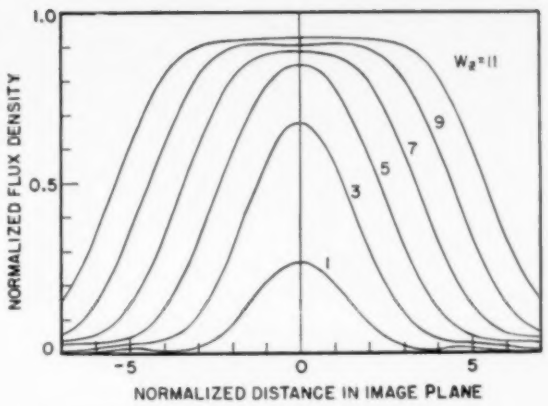

FIGURE 10. *Cross sections of images of finite-width object lines.*

The reduced object line widths are 1, 3, 5, 7, 9, and 11 x-units. Plotting the central flux density as a function of the reduced object line width results in the point-image characteristic curve shown in figure 6.

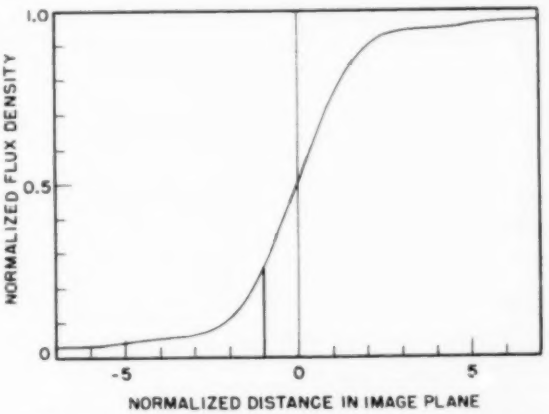

FIGURE 12. *Cross section of knife-edge image.*

The vertical line corresponds to the solid shown in figure 11.

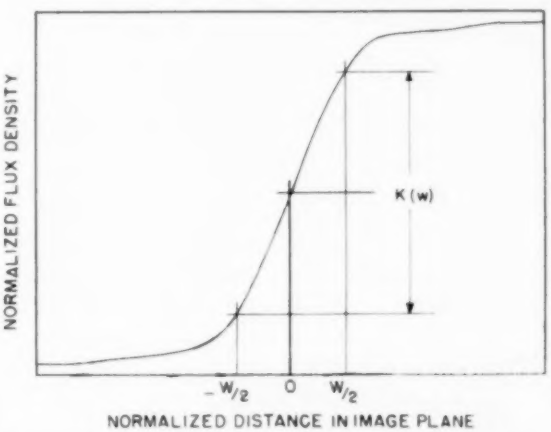

FIGURE 14. *Determination of point-image characteristic from knife-edge image.*

If the abscissa values a and b in figure 13 are made equal to $-w/2$ and $+w/2$ as in this figure, then the ordinate difference shown here is proportional to the corresponding area in figure 13, which itself is proportional to the corresponding value of the point-image characteristic, as indicated in figure 9.

Furthermore, regardless of which way it is obtained, it can be interpreted in terms of any of the objects. This is discussed further in a later section.

3. Evaluation by Fourier Analysis

A general object $O(x,y)$ can be analyzed into a continuum of sinusoidal spatial waves, differing from each other in direction, frequency, amplitude, and phase. The characteristics of these waves are given by the Fourier transform of the object,

$$T_o(\omega_x,\omega_y)=\int_{-\infty}^{\infty}\int_{-\infty}^{\infty} O(x,y)\exp\left[-i(\omega_x x+\omega_y y)\right]dxdy, \tag{13}$$

where $T_o(\omega_x,\omega_y)$ is complex, containing both amplitude and phase factors, and ω_x and ω_y are directional frequency components of the component waves.

A component wave itself is represented by

$$W_c=T_o(\omega_x,\omega_y)\exp\left[i(\omega_x x+\omega_y y)\right]. \tag{14}$$

Consider this to be an object. Then by applying eq (2),

$$I_W(x',y')=\int_{-\infty}^{\infty}\int_{-\infty}^{\infty}\varphi(x,y)T_o(\omega_x,\omega_y)\exp\left[i\{\omega_x(x'-x)+\omega_y(y'-y)\}\right]dxdy$$

$$=T_o(\omega_x,\omega_y)\exp\left[i(\omega_x x'+\omega_y y')\right]\int_{-\infty}^{\infty}\int_{-\infty}^{\infty}\varphi(x,y)\exp\left[-i(\omega_x x+\omega_y y)\right]dxdy. \tag{15}$$

The integral is the Fourier transform $\Phi(\omega_x,\omega_y)$ of $\varphi(x,y)$, and therefore

$$I_W(x',y')=\Phi(\omega_x,\omega_y)T_o(\omega_x,\omega_y)\exp\left[i(\omega_x x'+\omega_y y')\right]. \tag{16}$$

The function modified by Φ is seen to be simply the component object wave. Each component image wave then will be the product of Φ and the corresponding component object wave. Therefore,

$$T_I(\omega_x,\omega_y)=\Phi(\omega_x,\omega_y)T_o(\omega_x,\omega_y), \tag{17}$$

where T_I is the Fourier transform of the image.

If $I(x,y)$ can be considered to be the object of a second imaging process, then

$$T_{I_2}(\omega_x,\omega_y)=\Phi_2(\omega_x,\omega_y)T_{I_1}(\omega_x,\omega_y)=\Phi_2\Phi_1 T_o. \tag{18}$$

This can be extended to as many imaging processes as desired.

The transform

$$\Phi(\omega_x,\omega_y)=\int_{-\infty}^{\infty}\int_{-\infty}^{\infty}\varphi(x,y)\exp\left[-i\omega_x x+\omega_y y)\right]dxdy \tag{19}$$

is seen to be characteristic of the imaging process. Let us examine it in more detail.

The transform is the double integral of the product of two functions, one being the point image $\varphi(x,y)$ and the other a two-dimensional wave $exp[-i(\omega_x x+\omega_y y)]$.

This two-dimensional wave is sinusoidal in one direction and constant in the perpendicular direction, like a corrugated roof. The direction of the sinusoidal variation is inclined to the x-axis by an angle θ, where $\tan\theta=\omega_y/\omega_x$, and the frequency is given by $\omega_\theta=\sqrt{\omega_x^2+\omega_y^2}$ (see fig. 15). The transform can then be considered to be $\Phi(\theta,\omega_\theta)$.

For $\theta=0$, $\omega_y=0$ and the transform becomes

$$\Phi(\omega_x)=\int_{-\infty}^{\infty}\int_{-\infty}^{\infty}\varphi(x,y)\exp[-i(\omega_x x)]dydx=\int_{-\infty}^{\infty}L(x)\exp[-i(\omega_x x)]dx, \tag{20}$$

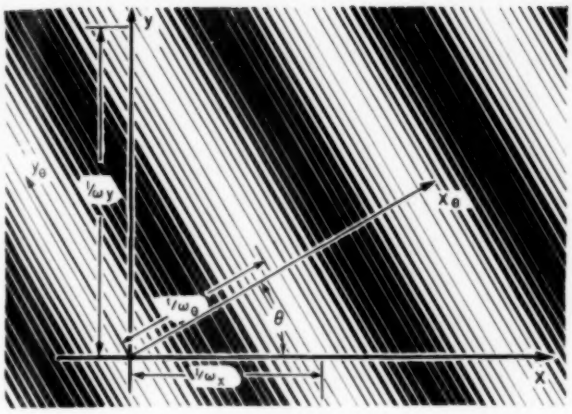

FIGURE 15. *Transformation of coordinates.*

If the direction of the pattern is inclined to the original x-axis by an angle θ, then, in the new coordinate system in line with the pattern, $\omega=\sqrt{\omega_x^2+\omega_y^2}$ and $\tan\theta=\omega_y/\omega_x$.

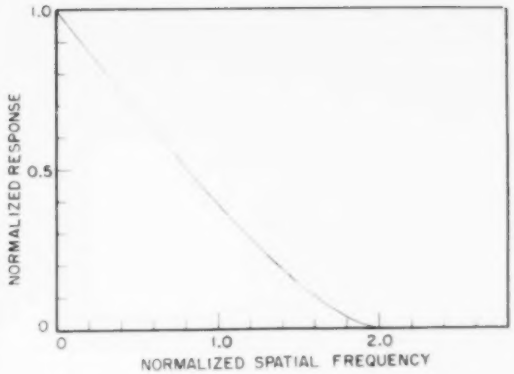

FIGURE 16. *Sine-wave response curve.*

This is the positive side of the cross-section of the Fourier transform of the point image shown in figure 1. It is also the Fourier transform of the fine-line image shown in figure 8.

where $L(x)=\int_{-\infty}^{\infty}\varphi(x,y)dy$ is the fine-line image (fig. 16).

If the x, y coordinates are rotated in x_θ, y_θ through the angle θ (fig. 15), then eq (20) can be generalized into

$$\Phi(\theta,\omega_\theta)=\int_{-\infty}^{\infty}L(x_\theta)\exp[-i(\omega_\theta x_\theta)]dx_\theta. \tag{21}$$

For any θ, the transform Φ of eq (21) is the cross section in the θ-direction of the solid representing the transform $\Phi(\omega_x, \omega_y)$. This is shown in figure 17.

Equation (21) serves as the basis for the experimental determination of Φ, since for each θ it is the transform of the fine-line image oriented with its length perpendicular to the θ-direction. The object can be one in which the flux density varies sinusoidally in one direction, and the detector aperture can be a fine slit.

The object can be represented by

$$O(x_\theta)=A+B\exp[i\omega_\theta x_\theta], \quad A\geq B. \tag{22}$$

The constant term is necessary because all flux densities must be positive. The image is given by

$$I(x_\theta)=A+\Phi(\omega_\theta)B\exp[i\omega_\theta x_\theta]. \tag{23}$$

Let $M_o=B/A$ be defined as the modulation in the object. The corresponding modulation in the image is $M_I=\Phi B/A$. The transform Φ is obtained by

$$\Phi=\frac{M_I}{M_o}. \tag{24}$$

The use of the modulation automatically compensates for any factor that changes the signal output of the testing device proportionally, such as the transmission factor of the lens, change in brightness of the source, change in gain of the detector amplifier, etc.

It must be remembered that Φ is actually complex, involving both an amplitude and a phase factor. However, if the origin of $\varphi(x,y)$ is properly selected, the phase shift is small. If $\varphi(x,y)$ is symmetrical about its origin, then there is no phase shift involved. In most cases, for evaluation purposes, the phase-shift factor can be neglected.

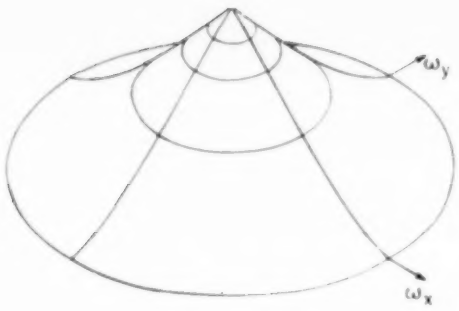

FIGURE 17. *Three-dimensional model of Fourier transform of point image.*

Each radial cross section is the sine-wave response in that direction. Note that the space is frequency space.

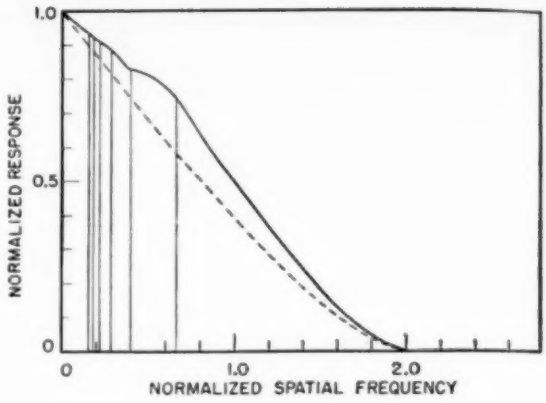

FIGURE 18. *Square-wave response curve.*

The dashed line is the sine-wave response curve from which this was derived. The vertical lines separate regions in which the square-wave image contains different numbers of harmonic components, each region having one more component than its neighbor to the right. In the region farthest to the right, the square-wave image contains only the fundamental.

4. Coordination

If $\Phi(\omega)$ is given, it is possible to predict a similar response curve in which the test object consists of alternate dark and light stripes, a spatial square wave. The square-wave test object can be analyzed into its component harmonics, each of which is attenuated by the value of Φ corresponding to its frequency, and the image is obtained by adding together these attenuated harmonics. For the response curve we are only interested in the peak-to-peak values that are obtained from the values at the centers of the lines and spaces. The square-wave response curve then is given by

$$\psi(\omega)=\frac{4}{\pi}\left[\Phi(\omega)-\frac{1}{3}\Phi(3\omega)+\frac{1}{5}\Phi(5\omega)-\cdots\right]. \tag{25}$$

It should be noticed that there will be only a finite number of terms in the sum because there is a limiting value of ω beyond which Φ remains at zero. This limit exists because of the finite dimensions of the aperture of the system; the larger the aperture the higher the limiting frequency.

Because of the finite range in ω, it is possible to obtain $\Phi(\omega)$ from $\psi(\omega)$ by the inverse process. Here it is necessary to start at the limiting value of ω and work backward. From this limiting value ω_c back to $\omega_c/3$ the sine-wave response is given by

$$\Phi(\omega)=\pi/4\ \psi(\omega) \tag{26}$$

because Φ and ψ are both zero for the odd multiples of ω for ω greater than $\omega_c/3$.

From $\omega_c/3$ to $\omega_c/5$,

$$\Phi(\omega)=\pi/4\ \psi(\omega)+\tfrac{1}{3}\Phi(3\omega), \tag{27}$$

where $\Phi(3\omega)$ may not be zero, and has already been found.

From $\omega_c/5$ to $\omega_c/7$,

$$\Phi(\omega)=\pi/4\ \psi(\omega)+\tfrac{1}{3}\Phi(3\omega)-\tfrac{1}{5}\Phi(5\omega), \tag{28}$$

and so forth.

The relationship between the square-wave response and the sine-wave response is illustrated in figure 18.

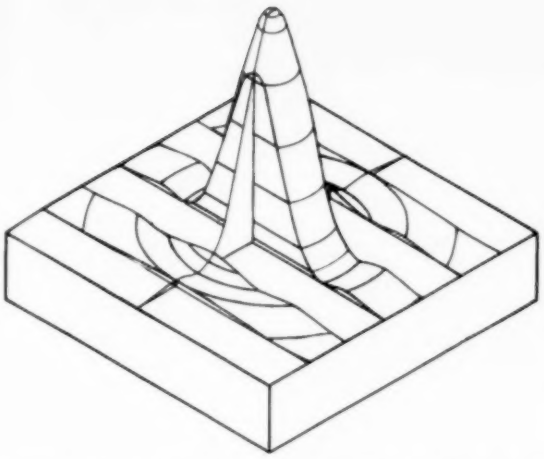

FIGURE 19. *Generation of square-wave response from point image.*

The sum of the volumes of the slabs is proportional to the flux density at the center of a bright line in the image. The sum of the volumes of the slabs that have been removed corresponds to the dark line. The difference between the two is proportional to the square-wave response.

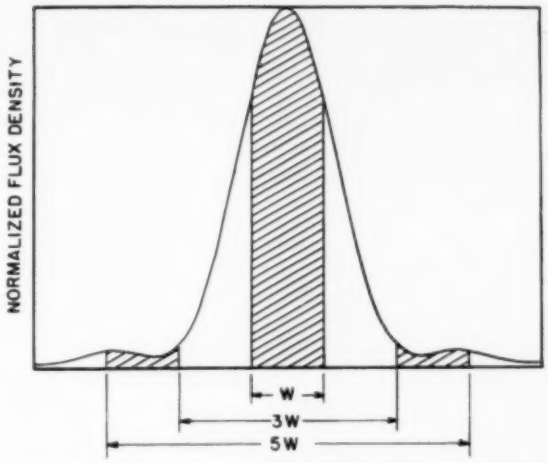

FIGURE 20. *Generation of square-wave response from fine-line image.*

The cross-hatched areas correspond to the slabs in figure 19. The marked widths indicate how the square-wave response can be obtained from the point-image characteristics.

The square-wave response may also be obtained from the point-image characteristic. If we consider the imaging of a square-wave test object as a point-image integration, then the flux density at the center of the image of a bright line in the pattern is proportional to the sum of the volumes of the slabs illustrated in figure 19, or the areas of the stripes in figure 20. The flux density at the center of the image of a dark line is proportional to the sum of the volumes of the slabs (or areas of the stripes) which lie between those illustrated. The sum of these two flux densities is proportional to the total flux in the point or fine-line image, and the square-wave response is given by

$$\Psi(\omega)=E\left(\frac{1}{2\omega}\right)-\left[1-E\left(\frac{1}{2\omega}\right)\right]=2E\left(\frac{1}{2\omega}\right)-1, \tag{29}$$

where $E(1/2\omega)$ is the flux density at the center of the image of a bright line and $1/2\omega=w$ is the width of a line, bright or dark, in the pattern.

It can be seen from figure 20 that

$$E\left(\frac{1}{2\omega}\right)=E(w)=K(w)+[K(5w)-K(3w)]+[K(9w)-K(7w)]+\ldots, \tag{30}$$

where $K(w)$ is the point-image characteristic, so

$$\Psi(\omega)=2\{K(w)+[K(5w)-K(3w)]+\ldots\}-1. \tag{31}$$

It is now apparent that $\Phi(\omega)$, the sine-wave response, may be obtained from $K(w)$, the point-image characteristic. This is done by determining $\psi(\omega)$, the square-wave response, from $K(w)$ and then applying the procedure indicated in eq (26), (27), and (28) to obtain the sine-wave response.[2]

To obtain the point-image characteristic from the sine-wave response is more direct. Consider the test object to be a variable-width line. The transform of the image of this object is obtained by multiplying the transform of the object by the sine-wave response of the system.

[2] This calculation for the case of the unaberrated image was made by the author before he was aware of Steel's equation (see appendix). It was done for 30 different spatial frequencies, using the tabulated values for the knife-edge image given by Struve (see appendix) as well as his approximation for values beyond those tabulated. The agreement between this calculated sine-wave response and Steel's equation is well within the error of calculation.

The transform of this object is of the form

$$T_o = w \frac{\sin \pi \omega w}{\pi \omega w} \tag{32}$$

shown in figure 21, and the transform of the image is given by $T_I = \Phi T_o$. The image itself would be given by the inverse transform

$$I(x_\theta) = \int_{-\infty}^{\infty} \Phi T_o \exp\left[i(\omega_\theta x_\theta)\right] d\omega_\theta, \tag{33}$$

but we are interested only in the value at the center of the line image where $x_\theta = 0$, so

$$K(w_\theta) = I(O) = \int_{-\infty}^{\infty} \Phi T_o d\omega_\theta = 2w \int_0^{\infty} \Phi(\omega_\theta) \frac{\sin \pi \omega w}{\pi \omega w} d\omega_\theta. \tag{34}$$

This equation shows the direct manner in which $K(w)$ may be obtained from $\Phi(\omega)$. For each w selected, the sine-wave response is multiplied by the proper calculated function of the form $\sin x/x$, and the product is integrated graphically or numerically. The result is then multiplied by $2w$, and the value obtained is the desired $K(w)$.

5. Application

It has been shown that an imaging system can be evaluated by means of a description of the point image or, alternatively, a description of its Fourier transform. Each of them has its advantages.

The Fourier approach allows us to combine several systems or to analyze a system into its components, under certain conditions. The principal condition is that each intermediate image formed by each component must be equivalent to a real luminous object having the same flux-density distribution in the image plane. Thus the combining or analyzing process can be applied to a photographic process, a television system, or a system in which each intermediate image is formed on a diffusing surface. It cannot be applied to a telescopic system because the light emerging from the primary image still contains the wave-front deformations produced by the objective and is subject to aberration correction by the ocular.

This does not mean that the Fourier approach cannot be applied to the entire telescopic system. It is just that the whole telescope cannot be precisely evaluated by simply evaluating the components.

Using the Fourier approach also enables one to apply the concepts developed in information and communication theory to imaging processes.

Another virtue of the Fourier approach is that the transform determined for any orientation of the sine-wave pattern in the image plane is a true section of the solid representing the entire transform in the image plane. A similar property does not hold for the point-image characteristic.

It should be noticed also that the sine-wave response of a lens has a finite boundary determined by the aperture of the system, whereas the point-image characteristic is unbounded.

The point-image characteristic, on the other hand, directly provides two basic types of information about the performance of the system, apart from the distribution of flux in the point image. These are the contrast at which an isolated object will be imaged as a function of the object size, and the gradient in the image of the edge of an extended object. The first holds because the point-image characteristic can be obtained by measuring the flux densities at the centers of finite-width line images. The second holds because the characteristic can also be obtained from the image of a knife-edge object.

However, if one knows either the point-image characteristic or the sine-wave response, he can calculate the other, as has been shown. It would probably be preferable to have a research instrument that would determine the sine-wave response, because the transformation to the point-image characteristic is more direct and more suitable for calculating machines than the reverse transformation.

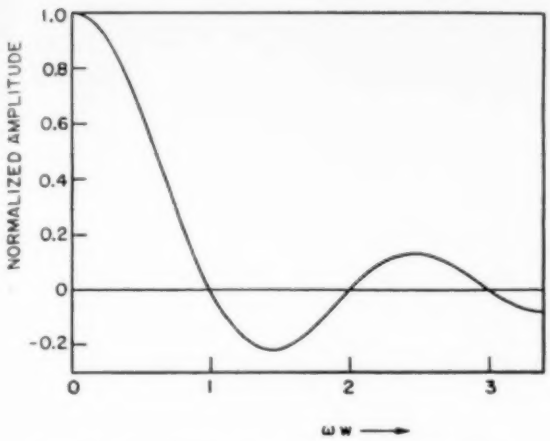

FIGURE 21. *Transform of finite-width line object.*

ω is the frequency of the component wave, and w is the reduced object-line width.

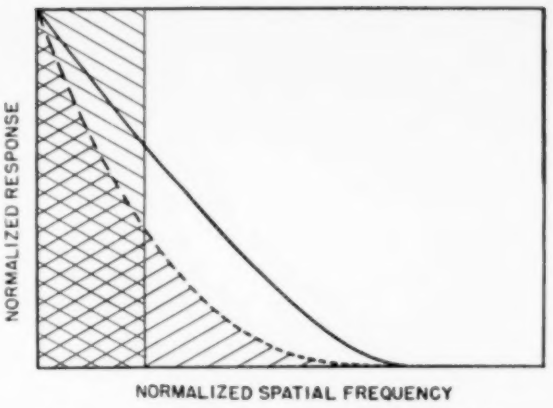

FIGURE 22. *Schade's equivalent bandwidth.*

The solid curve is the sine-wave response curve; the dashed curve is the square of the solid curve; and the rectangular area is equal to the area under the dashed curve. This rectangular area is measured by a single number, its limiting frequency, thereby providing a single number to describe the sine-wave-response curve.

Another problem that comes up is one that is involved in routine testing. It would be desirable to reduce the evaluating curve to a single number with as little loss of significant information as possible, and it would be desirable that this reduction be done automatically in the test procedure.

With respect to the sine-wave response curve, Schade has suggested a reduction in which the curve is squared, ordinate by ordinate, and then integrated. The resulting number is equal to the limiting frequency of a rectangular "response" curve having the same area as the squared sine-wave response curve. This establishes an equivalent bandwidth, shown in figure 22.

The mechanism that would permit this determination directly would be similar to the sine-wave response mechanism, except that a "noise" pattern instead of a sinusoidal pattern would be used. The ideal noise pattern contains all frequencies at equal amplitude but with random phase relations. The fluctuations in the photoelectric output produced by this pattern are fed through a squaring circuit and then integrated. The resulting steady current, indicated on a meter, is proportional to Schade's equivalent bandwidth. One trouble with this system is the difficulty involved in producing an acceptable noise pattern.

Equation (34) indicates another approach to the problem of representing the sine-wave response curve with a single number. The object transform T_0 in this equation can be considered to be a weighting factor for the sine-wave response curve, and the integral to represent the equivalent bandwidth Ω. Then this equivalent bandwidth can be determined by the use of a variable slit or a knife edge, for

$$\Omega=\frac{K(w)}{2w}. \tag{35}$$

For this to be single-valued, w must be fixed, and two convenient possible values appear evident. One is to set $w=1/\omega_c$, where ω_c is the limiting frequency for a theoretically perfect lens having the same aperture as the lens under test. Then the weighting function goes to its first zero at ω_c. This method is illustrated in figure 23.

The other convenient value for w is zero, for the limit of $K(w)/w$ as w goes to zero is the slope at the center of the knife-edge image, as can be seen with the aid of figure 14. As indicated in eq (35), this equivalent bandwidth is given by one-half the slope at the center of the knife-edge image. The weighting function approaches unity for small values of ω as w approaches zero, so this equivalent bandwidth is given by the area under the sine-wave response curve itself. This is illustrated in figure 24. It might be emphasized that this latter relationship is an important and fundamental condition. The slope at the center of a knife-edge image is exactly proportional to the area under the sine-wave response curve.

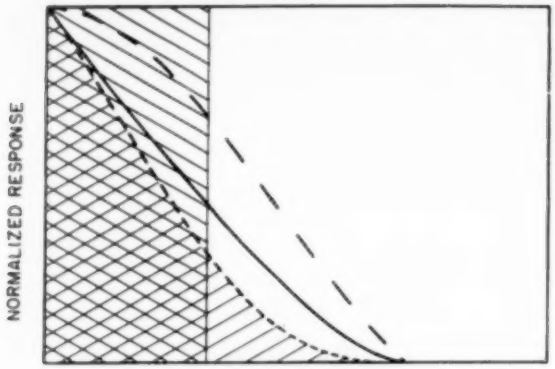

FIGURE 23. *Another equivalent bandwidth.*

The solid curve is the sine-wave response curve; the long-dashed curve is the transform of the finite-width-line object; the short-dashed curve is the product of the other two; and the rectangular area is equal to the area under the short-dashed curve. This provides a different single characteristic number, which can be obtained more easily than Schade's equivalent bandwidth.

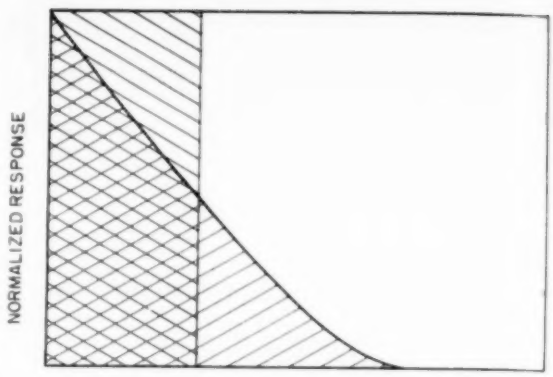

FIGURE 24. *A third equivalent bandwidth.*

This bandwidth is measured by the area under the sine-wave-response curve itself. The area is exactly proportional to the slope at the center of a knife-edge image.

The idea of measuring an equivalent bandwidth may be a good way of reducing the sine-wave response curve to a single number, but this process eliminates one of the advantages of the sine-wave approach, and that is the ability to combine directly a sequence of imaging processes. For most telescopic systems this may be unimportant, but if such a combination is desirable, then perhaps the sine-wave response curve can be characterized well enough by some particular frequency. If the response to some such frequency were established as a measure of quality, then the measure of the quality of the combination is simply the product of the measures of quality of the components.

To summarize, the Fourier approach seems to be more desirable for research and detailed testing, but the determination of the point-image characteristic lends itself to rapid routine testing.

6. Appendix

6.1. Images Produced by an Aberration-Free System With a Circular Aperture in Monochromatic Light

The extended objects are assumed to be illuminated noncoherently. In the following expressions, the unit of displacement in the image is:

$$z=\frac{2\pi a x}{\lambda d}, \tag{36}$$

where a is the radius of the circular aperture, x is the distance in the image plane from the center of the image, d is the distance from the image plane to the aperture, and λ is the wavelength of light.

a. Point Image

This is well known, and its section is given by

$$\varphi(z)=4\left(\frac{J_1(z)}{z}\right)^2. \tag{37}$$

It is illustrated in figures 1 and 2.

b. Fine-Line Image

An expression for the cross section of the fine-line image, implicit in the original work of Struve [1], is explicitly given by Steel [2] as

$$L(z)=\frac{3\pi}{8}\frac{H_1(2z)}{(2z)^2}, \tag{38}$$

where H_1 is what is known as the Struve function, and has been tabulated.[3] The cross section of the fine-line image is illustrated in figure 8.

c. Knife-Edge Image

Struve [1] developed this in a series expansion and tabulated it for z up to 15. If the edge is oriented so that the gradient for the image is positive, then the image is given by

$$S(z)=\frac{1}{2}+\frac{2}{\pi^2}\left\{\frac{3}{1}\frac{2^2z}{1^2\cdot3^2}-\frac{5}{3}\frac{2^4z^3}{1^2\cdot3^2\cdot5^2}+\frac{7}{5}\frac{2^6z^5}{1^2\cdot3^2\cdot5^2\cdot7^2}-\cdots\right\}. \tag{39}$$

Struve also gave a simple approximation, which is in error by less than 0.1 percent for $Z>7$ and 1.0 percent for $Z>3$.

$$S(z)\cong1-\frac{2}{\pi^2z}. \tag{40}$$

The knife-edge image is illustrated in figure 12.

d. Finite-Width Line Image

If the width of the Gaussian image is w_z, then

$$\overline{L(z)}=S\left(z+\frac{w_z}{2}\right)-S\left(z-\frac{w_z}{2}\right). \tag{41}$$

This family of images is illustrated in figure 10.

e. Point-Image Characteristic

This is given by

$$K(w_z)=S\left(\frac{w_z}{2}\right)-S\left(-\frac{w_z}{2}\right)=2S\left(\frac{w_z}{2}\right)-1. \tag{42}$$

Combining this with eq (39) gives

$$K(w_z)=\frac{4}{\pi^2}\left\{\frac{3}{1}\frac{2w_z}{1^2\cdot3^2}-\frac{5}{3}\frac{(2w_z)^3}{1^2\cdot3^2\cdot5^2}+\frac{7}{5}\frac{(2w_z)^5}{1^2\cdot3^2\cdot5^2\cdot7^2}-\cdots\right\}. \tag{43}$$

This is illustrated in figure 6.

f. Sine-Wave Response

Steel [2] gives the following expression for the sine-wave response:

$$\Phi(\omega)\begin{cases}=\frac{2}{\pi}\left(\arccos\frac{\omega}{2}-\frac{\omega}{2}\sqrt{1-\frac{\omega^2}{4}}\right), & 0<\omega<2\\ =0 \qquad\qquad\qquad\qquad\quad ; & \omega>2,\end{cases} \tag{44}$$

where $\omega=\pi/w_z$ and w_z is the wavelength of the sinusoid. Notice that there is an absolute limit to the frequency of the pattern that a lens can form, this limit being where the wavelength of the pattern in z units is equal to π.

The frequency, ν, in the image plane is given by

$$\nu=\frac{\omega}{2N\lambda}, \tag{45}$$

where $N=d/2a$ and λ is the wavelength of light. If λ is in millimeters, ν is in cycles per millimeter.

Figures 16 and 17 show the sine-wave response.

---

[3] E. Jahnke and F. Emde, Tables of functions with formulas and curves, 4th ed. (Dover Publications, New York, N. Y., 1945).

7. References

The data for the curves in the illustrations were calculated from the information contained in the following references:

[1] H. Struve, Beitrag zur theorie der diffraction an fernrohren, Ann. Physik Chemie **17,** 1008 (1882).

[2] W. H. Steel, Étude des effets combinés des aberrations et d'une obturation centrale de la pupille sur le contraste des images optiques. Premiére Partie, Rev. opt. **32,** 4 (1953).

Steel provides information on the point, disk, fine-line, knife-edge, sine wave, and square wave images. Material on the sine wave or Fourier transform approach is contained in the following references.

[3] O. H. Schade, A new system of measuring the specifying image definition, NBS Circular 526 (April 29, 1954).

[4] O. H. Schade, Image gradation, graininess, and sharpness in television and motion picture systems. Part II, J. Soc. Motion Picture Television Engrs. **58,** 181 (1952).

[5] P. Elias, D. S. Grey, and D. Z. Robinson, Fourier treatment of optical processes, J. Opt. Soc. Am. **42,** 127 (1952).

[6] E. W. H. Selwyn, The photographic and visual resolving power of lenses. I. Visual resolving power, Phot. J. **88B,** 6 (1948).

Schade is the first to build a practical machine for obtaining a sine-wave analysis of an optical system. Selwyn applies the Fourier treatment to the prediction of resolving power.

Work on the photoelectric examination of point images through circular apertures is reported in the following paper:

[7] R. E. Hopkins, Measurements of the energy distribution of optical images, NBS Circular 526 (April 29, 1954).

Interest in the knife edge is shown in the following references:

[8] W. Weinstein, Criteria of image-forming quality in photographic objectives, Phot. J. **91B,** 138 (1951).

[9] R. V. Shack, A proposed approach to image evaluation, NBS Circular 526 (April 29, 1954).

Shack also discusses the variable slit. Hopkins is now using knife edges in his work.

WASHINGTON, June 1, 1955.

Journal of Research of the National Bureau of Standards Vol. 56, No. 5, May 1956 Research Paper 2673

Advances in the Design and Application of the Radio-frequency Permeameter

Alvin L. Rasmussen, Albert W. Enfield, and Alfred Hess

Improvements are described for increasing the frequency coverage, accuracy, and ease of application of the radiofrequency permeameter developed at the National Bureau of Standards to measure initial complex permeability of toroidally shaped ferromagnetic materials of low conductivity. A brief review of the development of the permeameter is also presented. These improvements include (1) calibration of a permeameter, using a transfer permeability standard, (2) design of permeameter primaries for the frequency range of 0.05 to 50 megacycles, (3) modifications of the short of the permeameter secondary, (4) analysis and modifications of loss equations, (5) graphical methods of obtaining dissipation factor and permeability from measurement data, and (6) capacity calibration of a Q meter.

1. Definition of Symbols

μ_0' = Initial real permeability.
μ_0'' = Initial magnetic-loss factor.
L_a = Geometric inductance of test core.
μ_1 = Initial permeability of primary core.
L_{a1} = Geometric inductance of primary core.
μ_2 = Initial permeability of auxiliary core.
L_{a2} = Geometric inductance of auxiliary core.
L_s' = Geometric inductance of the empty coaxial enclosure of the permeameter.
R_0, L_0, X_0, Z_0 = Input resistance, inductance, reactance, and impedance, respectively, with permeameter secondary shorted.
R_1, L_1, X_1, Z_1 = Input resistance, inductance, reactance, and impedance, respectively, with permeameter secondary open.
R_f, L_f, X_f, Z_f = Input resistance, inductance, reactance, and impedance, respectively, with permeameter secondary shorted and a sample enclosed.
C_0 = Capacity required to resonate L_0.
C_1 = Capacity required to resonate L_1.
C_f = Capacity required to resonate L_f.
Q_0, Q_1, Q_f = Q's corresponding with C_0, C_1, and C_f, respectively.
C_{01}, C_{0f}, C_{f1} = C_0-C_1, C_0-C_f, and C_f-C_1, respectively.
ω, f = Angular frequency and frequency, respectively.
N = Effective turns ratio of primary to secondary.
X_2, Q_2 = Reactance and Q of secondary without test core, respectively.
R_u, X_u, Z_u = Additional secondary resistance, reactance, and impedance due to sample, respectively.
M = Mutual inductance between primary and secondary.
Tan δ_m = Magnetic-dissipation factor.
R_w, X_w = Wire resistance and wire reactance of the winding on the permeameter primary, respectively.
R_p = Effective series resistance of the primary core.
X_p, Z_p = Effective series reactance and impedance, respectively, of the primary core.
Z_{1f}, Z_{10} = Z_1-Z_f, Z_1-Z_0, respectively.
X_{1f}, X_{10} = X_1-X_f, X_1-X_0, respectively.
L_{1f}, L_{10}, L_{f0} = L_1-L_f, L_1-L_0, L_f-L_0, respectively.
R_{1f}, R_{10} = R_1-R_f, R_1-R_0, respectively.

2. Introduction

Advances in the design and application of the radiofrequency permeameter are presented.

The permeameter was developed for use in measuring initial permeability (μ_0') and dissipation factor (tan δ_m) of toroidally shaped ferromagnetic materials at radiofrequencies. It is an impedance transformer, the primary of which is wound on a powdered-iron toroid. The secondary is a shorting enclosure that envelops both the primary and the toroidal test-sample core, as shown in figure 1. Connections to the primary are brought out to terminals at the bottom of the enclosure. A number of different interchangeable primaries are provided, mounted in plastic cases. One of the shorting ends of the enclosure or section of coaxial line is removable to permit insertion of a toroidal test-sample core. The latter is usually half a centimeter or more above the primary. Thus, a nearly uniform sheet of current surrounds the test sample.

To make measurements, the primary of the permeameter is placed in one arm of an rf impedance bridge or across the terminals of a Q meter. Input impedances of the primary are then measured with: (1) permeameter secondary open, (2) permeameter secondary shorted without sample, and (3) permeameter secondary shorted with a sample enclosed. From these data μ_0' and tan δ_m are derived.

In order to increase the accuracy, precision, ease of application, and frequency coverage of this instrument, the following actions were undertaken, and are discussed in detail.

1. Calibration of a permeameter, using a transfer permeability standard, was introduced.
2. Primaries of the permeameter were designed for the frequency range 0.05 to 50 Mc.
3. The quality of the short at the end of the coaxial section was improved.
4. The loss equations were analyzed and proper modifications introduced.
5. Graphical methods of obtaining dissipation factor and permeability from measurement data were developed.
6. Q-meter capacitor increments were accurately calibrated in terms of an external precision capacitor.

The accuracies obtained with the original rf permeameter were not determined exactly [1].[1] With the above improvements, the accuracy of permeability obtained from reference to a primary standard

[1] Figures in brackets indicate the literature references at the end of this paper.

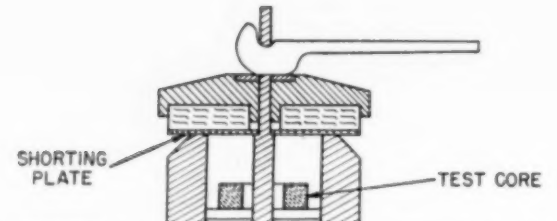

FIGURE 1. *Schematic drawing of type C radiofrequency permeameter.*

was ± 2 percent, and the estimated accuracy of the dissipation factor was ±10 percent ±0.003. These accuracies applied to the range 0.100 to 35 Mc. Low-loss and low-permeability powdered-iron materials, ordinarily difficult to evaluate, have been successfully measured in the improved permeameter.

3. Discussion

3.1. Calibration of a Permeameter, Using a Transfer Permeability Standard

The equation for initial permeability [1], using the parallel resonance method, is

$$\mu_0' - 1 = \frac{K}{L_a} \frac{C_{0f}}{C_{f1}}. \tag{1}$$

Permeameter calibration may be defined as an accurate determination of K at a given frequency. This K was formerly determined to an accuracy of 1 percent by means of National Bureau of Standards attenuation and voltage standards and measurement procedures based upon the relationship

$$K = \frac{1}{\omega^2 C_{01} N^2}. \tag{2}$$

The effective turns ratio, N, of the primary to the secondary was determined from voltage ratios measured with the piston attenuator [2] or the micropotentiometer [3]. Furthermore, K could be determined with reduced accuracy from vacuum-tube voltmeter measurements of the ratio N, or from the geometric inductance of the empty space in the permeameter secondary. Above 15 Mc the latter method appeared to be unreliable.

With the newly adopted calibration method, standard permeability cores were used as transfer inductance standards. The real initial permeability, μ_0', of a specially ground carbonyl E coaxial sample was determined to an accuracy much better than 1 percent with the primary standard of rf permeability [4] at the National Bureau of Standards. If the value of $(\mu_0' - 1)L_a$ is such that for the given permeameter C_{0f}/C_{f1} approaches unity, then it can be shown that the most accurate determination of K may be made. This condition was met. Also, for best accuracy, high-accuracy bridges were employed. Once a standard sample is available, numerous other secondary standard samples may be obtained from it by means of a permeameter and an accurately capacity-calibrated Q meter. Permeability values determined by means of secondary standard samples at the National Bureau of Standards were within 1 percent of the values obtained from the primary standard of rf permeability. Standard toroidal samples made from powdered-iron materials are best in this application because they usually are quite stable with time, and many have nearly a flat frequency response of real permeability. The method is relatively simple, more accurate, and more reliable.

3.2. Design of Permeameter Primaries for the Frequency Range 0.05 to 50 Mc

Re-entrant cavity techniques are used at the National Bureau of Standards down to 50 Mc to measure initial permeability and dissipation factor. The first permeameters were usable at 1 to 5 Mc with either Q meters or rf bridges, whereas at 0.05 to 1 Mc, bridges were employed because the inductances of the primaries were too low for application with Q meters. Therefore, high-inductance, high-Q coils were designed to remove this limitation. Additional primaries were designed for the frequency range 0.05 to 50 Mc. The following procedure was applied in this design work:

It can be shown [1] that, to a close approximation

$$K = L_2' - L_{a1} = \frac{1}{\omega^2 N^2 C_{01}}, \tag{3}$$

and

$$\mu_1 L_{a1} = \frac{1}{\omega^2 N^2 C_1}. \tag{4}$$

Therefore,

$$\frac{L_2' - L_{a1}}{\mu_1 L_{a1}} = \frac{C_1}{C_{01}}. \tag{5}$$

Appropriate values of C_1 and C_{01} were chosen to fall within the range of the instrument applied in the measurement technique. L_2' was selected after considering the sizes and permeabilities of the materials to be measured in the permeameter; μ_1 and L_{a1} of the primary were determined from eq 5; and L_{a1} was determined from the size of the permeameter. A material with the corresponding μ_1, good stability, and relatively high Q for the frequency was selected. A reasonable number of turns (approximately N, as determined from eq (4)) was chosen. As the required conditions could not always be met, parameters frequently were adjusted by successive approximations. The secondary inductance was sometimes increased by adding a relatively high permeability

loading toroid permanently to the secondary. Occasionally, fewer turns than ordinarily used at a frequency were chosen, and a loading toroid was possibly added when measuring very-high-permeability materials. A low-loss external capacitor was sometimes required in this case. The size of the wire on the primary was determined by the frequency of application, by the space available on the primary core, by the number of turns required, and by the best Q's obtainable.

Parameter restrictions are summarized as follows: When a permeameter–Q-meter combination was employed, C_0 was usually kept below 400 $\mu\mu$f at all frequencies to help obtain optimum Q values. For better accuracy, the capacitance difference, C_{01}, was made to be 50 $\mu\mu$f or more. Q values were high enough to give proper precision. Based on experience, the minimum values for Q_1 and Q_0 were selected as 100 and 25, respectively; and N decreased with frequency. Typical values of L_2', L_{a1}, μ_1, and N are given in tables 1 and 2 of the appendix.

It can be shown that approximately

$$Q_0 = \frac{X_1 - \dfrac{\omega^2 M^2}{X_2}}{R_1 + \dfrac{\omega^2 M^2}{X_2 Q_2}}. \qquad (6)$$

As X_2 and Q_2 are relatively small at the low frequencies, Q_0 also becomes very small at these frequencies.

The design of the 0.100-Mc primary (fig. 2) is cited as an example. Six hundred turns of machine-wound, extra-heavy-enameled No. 34 wire, banked every 2 or 3 turns to reduce the distributed capacitance and to have the winding extend only 360° around the toroid, resulted in the most satisfactory Q and a high self-inductance. The toroid [2] had a μ_1 approximately equal to 49. Because, for this case, C_0 was too large and Q_0 too small, an auxiliary toroidal core was mounted permanently next to the primary. This core increased X_2 and resulted in new and usable values of C_0 and Q_0.

Therefore, from eq (3)

$$K = L_2' - L_{a1} + (\mu_2 - 1) L_{a2}. \qquad (7)$$

Another example (fig. 2) is the 35-Mc primary, which had five turns of a thin pair of copper strips, ⅛ in. wide, wound 360° around a toroidal core;[3] μ_1 was about 4.8. A thin insulator was applied between turns. To reduce leakage, thin strips were used. Parameters N and μ_1 had to be small because of the relatively high frequency involved.

A rather comprehensive list of primary characteristics is given in the appendix, table 2. Each primary covers a limited frequency range about its calibrated frequency, so that measurements are possible practically anywhere over the entire frequency range of the permeameter. The primaries were especially designed for use with the Boonton Q meter 260A, which has a low-Q scale. The low-Q scale, obviously, is convenient for measuring high-loss materials. When rf impedance bridges are used, the frequency range of a primary may be increased many fold because a bridge may have a larger impedance range than a Q meter.

[2] Stackpole Carbon Co., St. Marys, Pa., material type S60.
[3] Polydoroff and Associates, Washington, D. C., material carbonyl Super J.

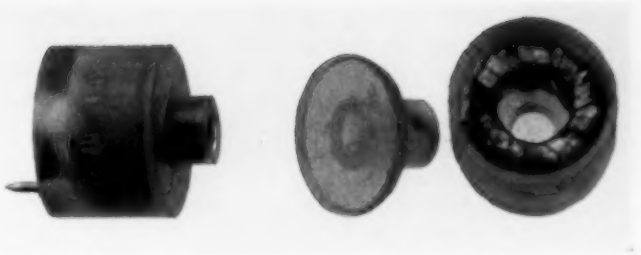

FIGURE 2. *Radiofrequency primaries, 0.100 Mc encased, and 35 Mc disassembled.*

3.3. Improvements of the Short at the End of the Coaxial Secondary

This section includes a brief description of all the shorts tested, before discussing the one finally adopted.

Beryllium plate and fingers. The first short, a beryllium-copper plate with a hole in the center, had thick fingers to fit snugly around the center conductor and the inside wall of the outer conductor of the coaxial. A nut pressed this plate against the flat surface of the conductor. The rf resistance of this short was much higher in magnitude than the resistance due to most magnetic materials to be tested, and was nonreproducible, especially for use in the measurement of materials with relatively low permeabilities and dissipation factors.

Thin beryllium fingers (0.010 in. thick) had similar disadvantages in addition to permanent bending with use. Commercially made folded fingers were no better.

Nonlocking tapers. Two nonlocking 9° tapers met with some success. Two concentric plates (ref. [1], fig. 1) were used to minimize wear. The larger plate was made of beryllium copper, and the other plate and the rest of the permeameter were made of brass. Furthermore, surface friction between similar metals was reduced. The smooth contact surfaces were lapped circumferentially so that surfaces would fit into each other and make improved electrical contact.

Disadvantages of this shorting method, appearing after the measurement of a few hundred toroids, were contact surface wear and poor reproducibility. Metal from the rubbing contacts would burr and scar the surfaces. However, relapping and cleaning contact surfaces with acetone did slow down this wearing process.

Continuous-surface short. The ideal condition for a reproducible secondary short is for the two faces of the tapers always to meet to form a continuous

surface from the center conductor to the outer conductor walls inside the permeameter at the same plane. Unusual wear and the stretching of threads cannot be tolerated because they result in electrical contact occurring at numerous places along the threads of the center conductor.

A superior shorting plate was therefore designed. The design principles are applicable to numerous impedance-measuring devices. Figure 1 and figures 3, 4, and 5 show the permeameter assembly details. The stainless-steel clamp exerts downward pressure upon the brass cap, the rubber, and the thin shorting plate, which is made of phosphorus-bronze. The shorting plate is pressed against ledges of the outer conductor and the center conductor. The short is a continuous surface, and the resistance remains as constant as the pressure.

When used with a coaxial line, at 1 Mc, the short was reproducible to three ten-thousandths of an ohm, and no variations of inductance were observed with a bridge capable of measuring differences as small as 1 mμh. Contact surfaces were kept clean with acetone and polished occasionally with crocus cloth to maintain such a high degree of reproducibility.

After several thousand measurements, changes of the input impedance of the empty shorted permeameter resulted from the wearing of the surfaces of the center conductor above the clamp. Also, the thin plate showed a very slight impression around the center conductor. These brass surfaces of the center conductor were then replaced with stainless steel. The rubber [4] in the cap, brass-resistant natural rubber of near Shore hardness 45, was made suitable for frequent use over a period of at least 2 years.

The rubber and the plate are replaceable, and the permeameter may be easily calibrated with a standard core. The shorting plate pressure must be sufficient to assure good reproducibility. The construction of the center conductor above the shorting plate may be improved by using a stainless-steel section attached to the rest of the center conductor.

Below 0.300 Mc slight variations of pressure appeared to cause more noticeable changes in the input impedance. However, the reproducibility over a long time was still much better than any other shorting arrangement developed thus far at the National Bureau of Standards. Above several hundred kilocycles, the reproducibility of Q's above 40 may be as good as ± 1 percent, and of C's, ± 0.15 $\mu\mu$f. In this design, the narrowed electric-contact surfaces reduced the amount of surface irregularity and assisted in maintaining the good reproducibility.

3.4. Analysis and Modifications of Loss Equations

In a former analysis of the permeameter [1] the transformer was implicitly represented by an equivalent network, which included primary core losses with the wire losses, as shown in figure 6,a. They are separated in the network shown in figure 6,b,

[4] Made by F. L. Roth, of Organic and Fibrous Materials Division of the National Bureau of Standards.

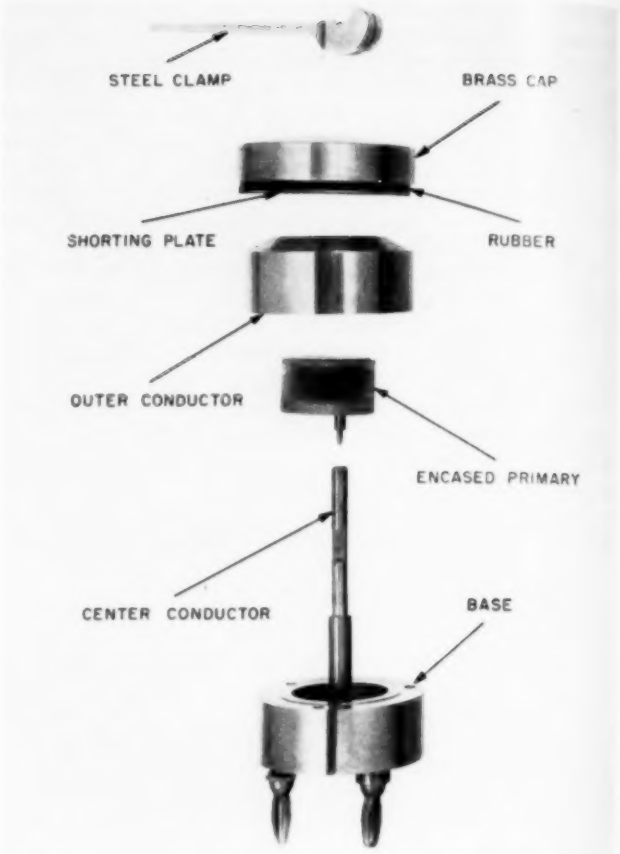

FIGURE 3. *Type C radiofrequency permeameter disassembled.*

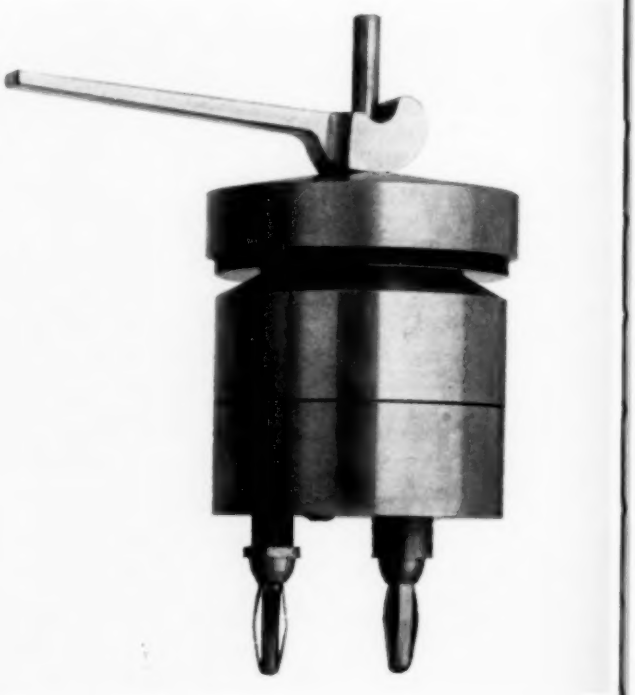

FIGURE 4. *Type C radiofrequency permeameter assembled.*

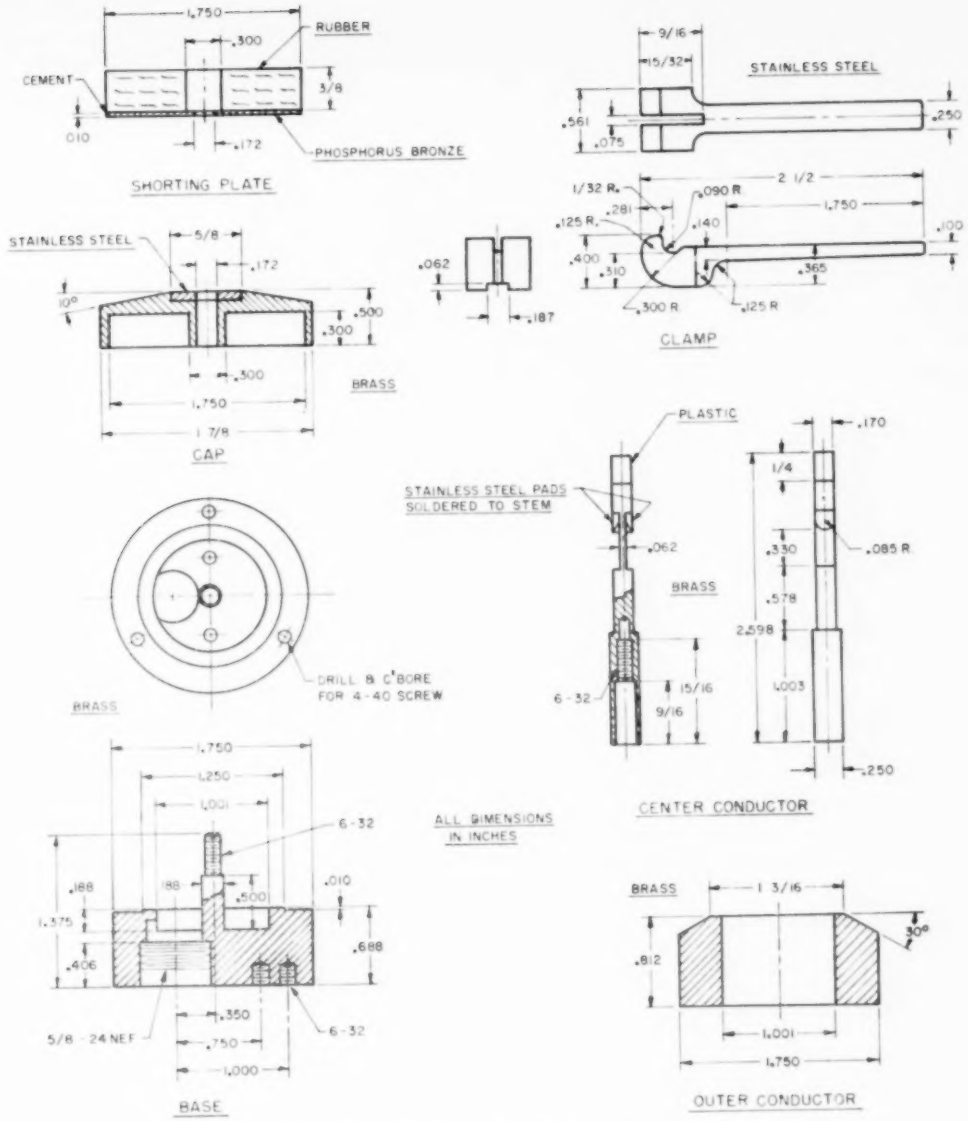

FIGURE 5. *Details of type C radiofrequency permeameter.*

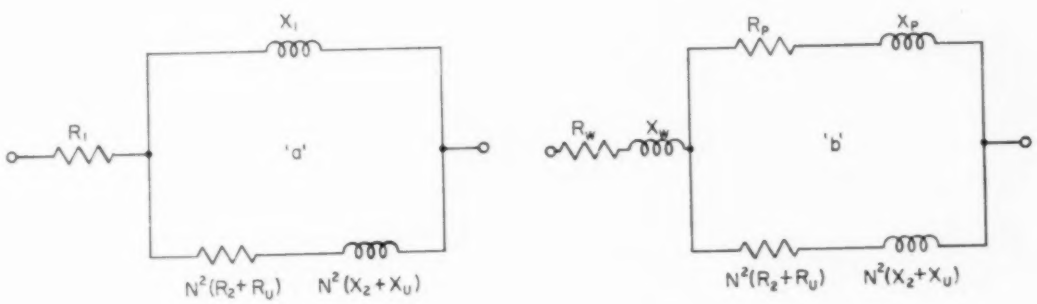

FIGURE 6. *Transformer network representations of radiofrequency permeameter.*

in the same manner as used by Kelsall in his original paper [5]. An analysis of the latter network is

$$Z_1 = jX_w + R_w + Z_p \tag{8}$$

$$Z_0 = jX_w + R_w + N^2\left(\frac{Z_p Z_2}{Z_p + N^2 Z_2}\right). \tag{9}$$

Subtracting eq (9) from eq (8) and substituting (Z_2+Z_u) for Z_2 and Z_f for Z_0, we have

$$\frac{Z_p^2}{Z_{1f}} - Z_p = N^2(Z_2 + Z_u). \tag{10}$$

Then, eliminating Z_2, we obtain

$$Z_u = \frac{Z_p^2}{N^2}\left(\frac{1}{Z_{1f}} - \frac{1}{Z_{10}}\right). \tag{11}$$

Experimentally, it is known that Z_{1f} and Z_{10} are very nearly equal to X_{1f} and X_{10}, respectively.

Thus, simplifying eq (11) gives the equations

$$N^2 R_u = (R_p^2 - X_p^2)A + 2R_p X_p B, \tag{12}$$

and also

$$N^2 X_u = 2R_p X_p A + X_p^2 B, \tag{13}$$

where A and B are defined as

$$A = \frac{R_{1f}}{X_{1f}^2} - \frac{R_{10}}{X_{10}^2} \tag{14}$$

$$B = \frac{1}{X_{1f}} - \frac{1}{X_{10}}. \tag{15}$$

Now, dissipation factor is defined as

$$\frac{\mu_0''}{\mu_0'} = \frac{R_u}{\omega \mu_0' L_u} = \frac{R_u}{X_u}\left(\frac{\mu_0' - 1}{\mu_0'}\right). \tag{16}$$

Therefore,

$$\tan \delta_m' = \left[\frac{\left(\frac{R_p^2}{X_p^2} - 1\right)\frac{A}{B} + 2\frac{R_p}{X_p}}{1 + 2\frac{R_p}{X_p}\frac{A}{B}}\right]\left(\frac{\mu_0' - 1}{\mu_0'}\right), \tag{17}$$

where the prime is used to designate a closer approximation than given in reference [1].

The expression A/B may be written as

$$\frac{A}{B} = \frac{L_{10}L_{1f}}{\omega L_{f0}}\left(\frac{R_{1f}}{L_{1f}^2} - \frac{R_{10}}{L_{10}^2}\right). \tag{18}$$

This expression is exactly the negative of the expression for tan δ_m [1], which is

$$\tan \delta_m = \frac{L_{10}L_{1f}}{\omega L_{f0}}\left(\frac{R_{f1}}{L_{1f}^2} - \frac{R_{01}}{L_{10}^2}\right). \tag{19}$$

Furthermore, R_p/X_p is of the order of magnitude of the dissipation factor of the primary core. For low-loss material, tan $\delta_m \ll 1$, therefore,

$$2\frac{R_p}{X_p}\tan \delta_m \ll 1. \tag{20}$$

Consequently, the dissipation factor (tan δ_m') may be expressed in terms of tan δ_m and of the dissipation factor of the primary core as follows:

$$\tan \delta_m' = \left(\tan \delta_m + 2\frac{R_p}{X_p}\right)\left(\frac{\mu_0' - 1}{\mu_0'}\right). \tag{21}$$

When materials with a dissipation factor of the same order of magnitude as the primary core are measured, eq (21) should obviously be used.

3.5. Graphical Methods of Obtaining Dissipation Factor and Permeability from Measurement Data

When the permeameter is used with a Q meter, it can be shown that [5]

$$\tan \delta_m = \frac{C_{01}C_{f1}}{C_{0f}}\left[\frac{1}{C_{f1}^2}\left(\frac{C_f}{Q_f} - \frac{C_1}{Q_1}\right) - \frac{1}{C_{01}^2}\left(\frac{C_0}{Q_0} - \frac{C_1}{Q_1}\right)\right] - \frac{2}{Q_1}. \tag{22}$$

Computing tan δ_m from this equation is obviously a lengthy process. It would be more convenient to obtain values of tan δ_m from graphs. The graphs could be used over a long period because, as stated before, the application of the improved permeameter results in measurements with a high degree of reproducibility.

One may, by using permeameter data obtained in conjunction with a Q meter at some given frequency, plot C_f/Q_f versus C_f by using a family of tan δ_m curves [6]. Tan δ_m values (fig. 7) are easily derived through

[5] Equation (22) is a simplification of dissipation factor eq (26) in ref. [1].

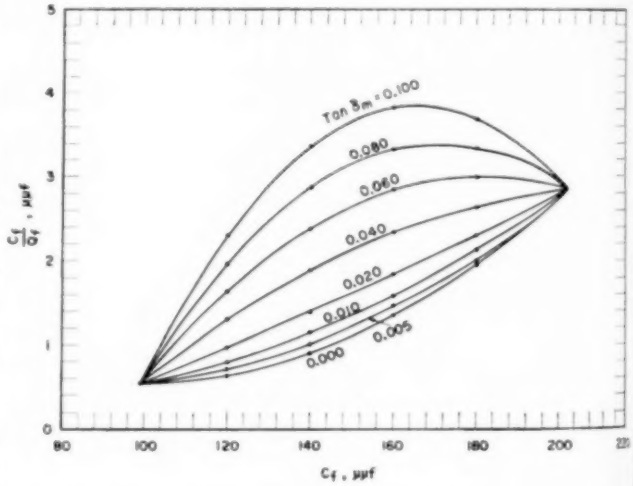

FIGURE 7. *C_f/Q_f versus C_f, using a family of tan δ_m curves for permeameter and Q meter at one frequency.*

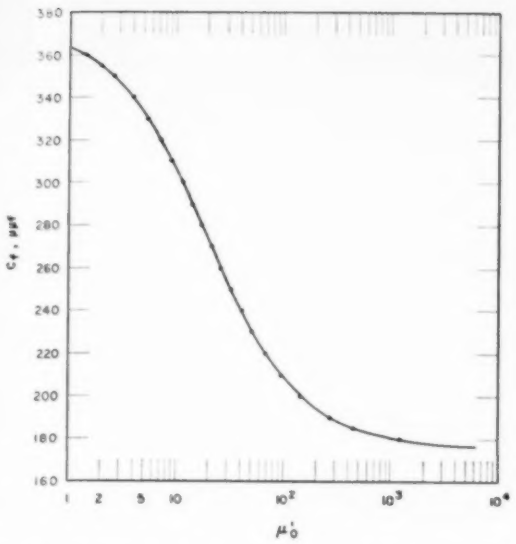

FIGURE 8. *C_f versus μ_0' for permeameter $K/L_a=20$ and Q meter at one frequency.*

interpolation between tan δ_m curves after locating coordinates on a graph. Several graphs at other frequencies may be constructed to cover effectively the desired frequency range.

If a large number of cores, having approximately the same value of L_a, are to be measured at one frequency on a calibrated Q meter, considerable time may be saved by again using a graph (fig. 8). C_f versus μ_0' is plotted on semilogarithmic paper, with C_f as the linear coordinate. The end points on the graph are determined from the values of C_1 and C_0, and C_f is plotted in 10-$\mu\mu$f steps over the center part of the range and in 5-$\mu\mu$f steps near the ends. The point of inflection of the curve occurs when the ratio C_{0f}/C_{f1} equals unity. The shape of the curve will vary according to L_a value used.

3.6. Capacity Calibration of a Q Meter

The capacitance of a Q meter, while corresponding to the dial reading to good accuracy, is not a smooth function of the dial reading; hence capacitance differences as read can be in error by a large amount and may even be opposite in the direction of change.

To reduce this error, the Q-meter capacitor was calibrated against a more precise capacitor by using a direct substitution method. To facilitate this calibration and subsequent measurements, an enlarging lens with a vertical hairline was mounted in front of the dial to eliminate parallax and enable more precise reading.

It was found that sufficient accuracy could be obtained by using a 2.5-mh coil at 130 kc and a 100- to 1100-$\mu\mu$f precision rf capacitor connected with short leads. This combination gave high Q for precise reading, and the frequency was low enough that corrections were not necessary for lead inductance.

The radiofrequency permeameter described in this paper has been modified for measuring complex permeability as a function of temperature and direct-current bias. Other modifications have been considered.

4. References

[1] P. H. Haas, A radiofrequency permeameter, J. Research NBS **51**, 221 (1953) RP2454.

[2] R. E. Grantham and J. J. Freeman, A standard of attenuation for microwave measurements, Trans. Am. Inst. Elec. Engrs. **67**, 535 (1948).

[3] M. C. Selby, Accurate radio-frequency microvoltages, Communication and Electronics, No. 6, 158 (May 1953).

[4] High frequency calibration of magnetic materials, NBS Tech. News Bul. **36**, 158 (Oct. 1952).

[5] G. A. Kelsall, Permeameter for alternating current measurements at small magnetizing forces, J. Opt. Soc. Am. and Rev. Sci. Instr. **8**, 334 (Feb. 1924).

[6] G. P. McKnight, Permeameter for radio frequencies, Elec. Mfg. **52**, No. 4, 150 (Oct. 1953).

5. Appendix. Permeameter Dimensions and Description of Primaries

TABLE 1. *Dimensions of five permeameters*

	Type of permeameter				
	A (tapered shunt)		*B* (tapered shunt)		*C* [a] (Pressure shunt)
	a [a]	*b*	*a*	*b*	
Height (*H*), in	1.032	1.188	1.188	1.288	1.000
Inside diameter (2*A*), in	0.188	0.188	0.250	0.250	0.250
Outside diameter (2*B*), in	1.000	1.000	1.600	1.600	1.001
Geometric inductance of the empty secondary (L_2') [b], h	8.76×10^{-9}	10.1×10^{-9}	11.2×10^{-9}	12.1×10^{-9}	7.05×10^{-9}

[a] Designed especially for measuring powdered-iron materials.

[b] $L_2'=2H(\ln B/A)\times10^{-7}$ h, where H is in meters.

TABLE 2. *Examples of wound primaries in various permeameters*

Calibration frequency, f	Core material [a]	Approximate value of permeability, μ_i	Number of turns [b] and kind of wire	Permeameter applied [c]	Remarks	Permeameter with characteristics given in columns at right	Approximate values of capacitance and Q			
							C_1	Q_1	C_2	Q_2
Mc							*μμf*		*μμf*	
0.100	Stackpole S60, with auxiliary S60 core.[d]	49	600; No. 34 Formex	All five	Machine wound, with frequent banking of turns.	*C*	169	169	377	41
.300	Stackpole S60, with auxiliary S60 core.[d]	49	250; No. 34 Formex	*C*	Machine wound, with about 0.1-in. spacing between every group of 40 or 50 turns around the core.	*C*	118	143	329	44
.675	Carbonyl E	8.9	180; 10-strand Litz No. 38.	*Aa* and *Ab*		*Aa*	209	146	431	30
1	do	8.9	164; No. 34 Formex	All five		*C*	140	167	289	36
1	do	8.9	140; 10-strand Litz No. 41.	do	Occasional banking of turns	*C*	189	242	388	40
1.5	do	8.9	100; 10-strand Litz No. 41.	do		*C*	177	200	364	41
2.5	Carbonyl SF	7.8	62; No. 24 Formex	do		*Aa*	157	194	286	53
3	Carbonyl E	8.9	50; No. 24 Formex	do		*C*	164	195	351	53
3	Carbonyl SF	7.8	50; No. 24 Formex	do		*C*	186	232	359	76
5	do	7.8	36; No. 24 Formex	do		*C*	99	183	202	70
10	do	7.8	15; No. 20 Formex	do		*C*	157	167	317	80
15	do	7.8	15; No. 20 Formex	do		*C*	67	139	139	90
30	Polydoroff Super J	4.8	5; thin pairs of copper strips, $\frac{1}{8}$ in. wide.	*C*	Dimensions affect values at right more than at lower frequencies.	*C*	179	123	252	93
35	do	4.8	5; thin pairs of copper strips, $\frac{1}{8}$ in. wide.	*C*	do	*C*	130	126	184	99

[a] The size of all primary cores was approximately: $2A=0.505$ in., $2B=0.795$ in., and $H=0.325$ in., where $L_{ai}=0.75\times10^{-9}$ h.
[b] Number of turns is approximately equal to the turns ratio N.
[c] See table 1 for specifications.
[d] At 0.100 Mc the sizes of the auxiliary core were approximately:
Permeameters *A* and *C*: $2A=0.255$ in., $2B=0.345$ in., and $H=0.430$ in.
Permeameter *B*: $2A=1.000$ in., $2B=1.570$ in., and $H=0.250$ in.
At 0.300 Mc with permeameter *C*, the size of the auxiliary core was approximately:
$2A=0.255$ in., $2B=0.345$ in., and $H=0.220$ in.

BOULDER, August 19, 1955.

Journal of Research of the National Bureau of Standards Vol. 56, No. 5, May 1956 Research Paper 2674

A New Computer for Calculating the Water Content of Gases

A. W. Diniak and E. R. Weaver

A new computer designed to reduce the labor in computing the water content of gases is described, and details of construction and use are given. The computer is of the circular slide-rule type with an accuracy of about that of a 10-inch slide rule. The computer consists of three disks with appropriate circular scales, which automatically correct for all deviations from ideality. It is a completely new design of an earlier model, and it is based on newly determined values for the corrections. The primary function of the computer is to calculate the water content and dewpoint of gases at pressures up to 6,000 pounds per square inch quickly, accurately, and with a minimum of effort, but it may be used for many other computations. Attention should be called to the fact that deviations from ideality are not dependent on methods of measurement and that they affect many measurements and computations in which they are usually ignored.

1. Introduction

Determining the water content of gases by the Weaver-electrical method [1, 2, 3] [1] involves the solution of the general equation

$$W_x = W_s \frac{P_w P_c (1 - KP_c + K'P_c^2)}{P_s(1 - KP_s + K'P_s^2) P_x (1 - KP_x + K'P_x^2)} \quad (1)$$

where W_x is the unknown concentration (weight per unit volume) of water vapor in the gas being tested, W_s is the concentration of water in the comparison gas at pressure P_s (usually W_s is the concentration of water vapor in equilibrium with liquid water or with ice, and P_s is the pressure of saturation), P_c is the absolute pressure of the comparison gas at which the fugacity of its water vapor is equal to that of the unknown gas at pressure P_x, P_w is the pressure at which W_x is to be expressed—usually 1 atm, and K and K' are constants, the values of which were determined experimentally [4] to be $K = 1.9 \times 10^{-4}$, $K' = 1.4 \times 10^{-8}$ for air and other gases (like oxygen and nitrogen) that behave similarly. All pressures in this equation are expressed in pounds per square inch absolute.

To solve the equation by longhand takes much more time than to make the measurements needed for a determination. To reduce the labor in making the necessary computations, a simple computer designed for the purpose may be used. The principle of the computer is not new; but it is a completely new design of an earlier model described by Weaver and Riley [1]. The computer is a circular slide rule consisting of three disks with appropriate circular scales inscribed on them. The several multiplications and divisions required for the solution of eq (1) are made by adding and subtracting angles proportional to the logarithms of the numbers indicated by the scales. Although the primary function of the computer is to solve the general equation for W_x quickly, accurately, and with a minimum of effort, it may also be used for many other computations. The deviation from ideality that makes necessary the corrections involving K and K' is, of course, a natural phenomenon that should not be ignored in work at high pressures, whatever the method of determining water vapor.

[1] Figures in brackets indicate the literature references at the end of this paper.

2. General Arrangement of the Computer

The computer consists of a base disk and two rotating disks with protruding tabs. Circular scales are arranged on the three disks in such a way that the general equation can be solved for W_x with a minimum of manipulation. The computer is shown in figure 1.

3. Base Disk

The base disk (fig. 2) contains two scales, a logarithmic scale near its outer rim and a temperature scale near its center. Concentrations of water vapor are marked in milligrams per liter on the outer scale. Because this scale is a logarithmic scale like that of the ordinary slide rule, it can be used for a variety of computations involving, particularly, conversions from one unit to another. Data used in constructing the scale, and other details, are given in table 1.

On a relatively small circle on the base disk is a scale of Fahrenheit temperature, covering the range of −30° to +120° F. This scale is read through windows in the two upper disks. On it, angles are proportional to the logarithm of the vapor pressure of water at saturation at the temperatures marked on the scale. The arrangement of the temperature scale in relation to the outside scale and the markings on the latter require explanation.

It is the purpose of the computer to solve problems involving the compositions of gas mixtures (relative quantities of water vapor and of other gases), and it is convenient to express all compositions in terms of the weight of water in the quantity of mixture that would occupy unit volume under some standard condition, in this case 1 atm and 70° F. If p_{70} represents the vapor pressure of water at 70° F, W_{70} its density, and p_t and W_t the vapor pressure

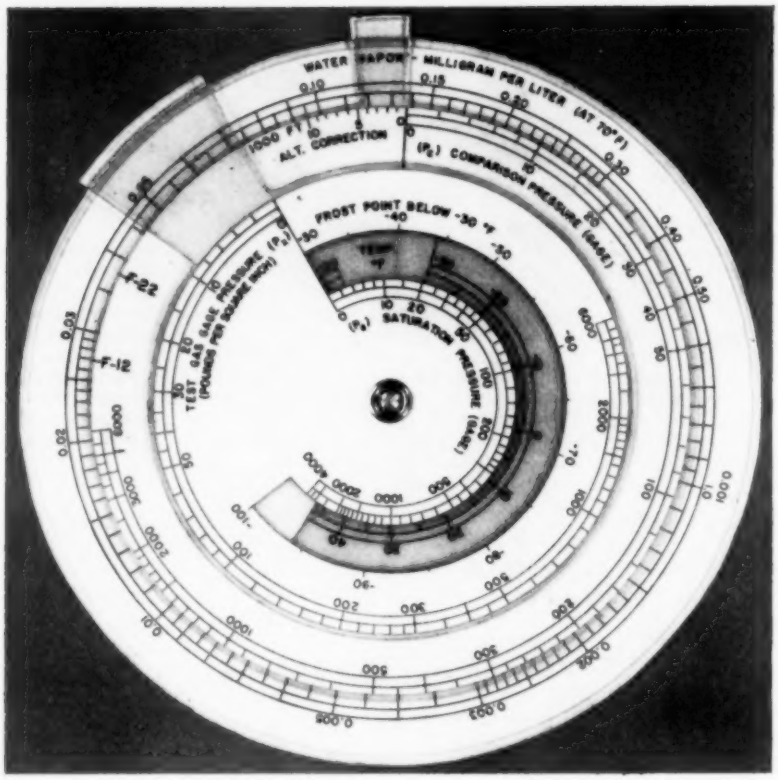

FIGURE 1. *Assembled computer (approximately full size).*

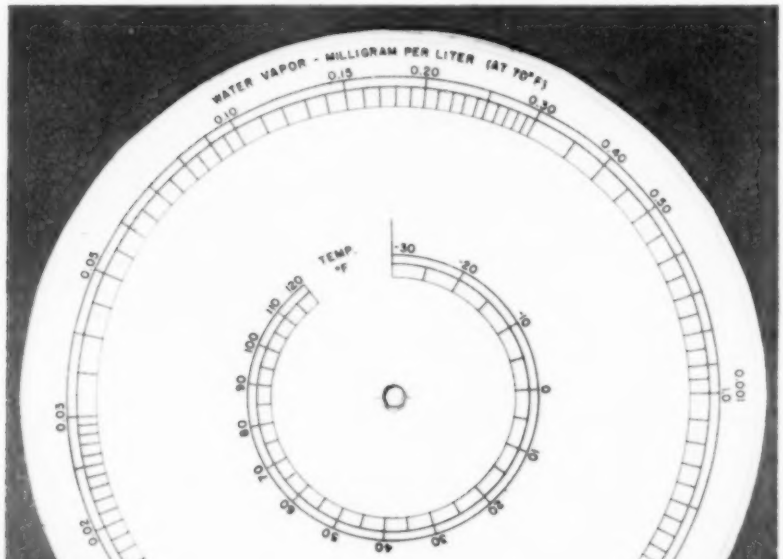

FIGURE 2. *Base disk.*

TABLE 1. *Data for outer logarithmic scale on base disk*

(The scale is marked in milligrams of water vapor per liter at 70° F.)

No.	Logarithm	1st cycle		2d cycle		3d cycle	
		Angle [a]	Label	Angle	Label	Angle	Label on scale
		deg		*deg*		*deg*	
1.0	0.0000	0.0	1.0, 0.001[b]	120.0	0.01	240.0	0.10
1.1	.0414	5.0		125.0		245.0	
1.2	.0792	9.5		129.5		249.5	
1.3	.1139	13.7		133.7		253.7	
1.4	.1461	17.5		137.5		257.5	
1.5	.1761	21.1		141.1		261.1	0.15
1.6	.2041	24.5		144.5		264.5	
1.7	.2304	27.6		147.6		267.6	
1.8	.2553	30.6		150.6		270.6	
1.9	.2788	33.4		153.4		273.4	
2.0	.3010	36.1	0.002	156.1	0.02	276.1	0.20
2.1	.3222	38.7		158.7		278.7	
2.2	.3424	41.1		161.1		281.1	
2.3	.3617	43.4		163.4		283.4	
2.4	.3802	45.6		165.6		285.6	
2.5	.3979	47.7		167.7		287.7	
2.6	.4150	49.8		169.8		289.8	
2.7	.4314	51.8		171.8		291.8	
2.8	.4472	53.7		173.7		293.7	
2.9	.4624	55.5		175.5		295.5	
3.0	.4771	57.2	0.003	177.2	0.03	297.2	0.30
3.5	.5441	65.3		185.3		305.3	
4.0	.6021	72.2		192.2		312.2	
4.5	.6532	78.4		198.4		318.4	
5.0	.6990	83.9	0.005	203.9	0.05	323.9	0.50
5.5	.7404	88.8		208.8		328.8	
6.0	.7782	93.4		213.4		333.4	
6.5	.8129	97.5		217.5		337.5	
7.0	.8451	101.4		221.4		341.4	
7.5	.8751	105.0		225.0		345.0	
8.0	.9031	108.4		228.4		348.4	
8.5	.9294	111.5		231.5		351.5	
9.0	.9542	114.5		234.5		354.5	
9.5	.9777	117.3		237.3		357.3	
10.0	1.0000	120.0	0.01	240.0	0.10	360.0	1.0, 0.001[b]

[a] The angles for the three cycles were calculated as follows:
For the 1st cycle: Angle = 120×log of each number.
For the 2d cycle: Angle = angle used in 1st cycle plus 120.
For the 3d cycle: Angle = angle used in 1st cycle plus 240.

[b] There are two labels on this mark.

and density at temperature t, and if the water vapor at this low pressure behaves as an ideal gas,

$$\frac{W_t}{W_{70}}=\frac{p_t}{p_{70}}\frac{70+460}{t+460}. \tag{2}$$

However, we are concerned not with the density (or concentration) of the water vapor at temperature t but with its concentration, W_x, in the gas mixture at 70° F if the temperature is changed without gain or loss of vapor.

$$\frac{W_x}{W_t}=\frac{t+460}{70+460}, \tag{3}$$

combining eq (2) and (3)

$$\frac{W_x}{W_{70}}=\frac{p_t}{p_{70}}\frac{70+460}{t+460}\frac{t+460}{70+460}=\frac{p_t}{p_{70}}. \tag{4}$$

Because of this direct proportionality, it is only necessary to arrange the two scales so that the logarithm of vapor pressure at 70° F is on the same radius as the logarithm of the concentration of water vapor at that temperature multiplied by a convenient power of 10, and any other concentration "reduced" to 70° will then be found on the same radius as its corresponding temperature. Because familiarity with the ideal gas law might make the reduction to 70° easier to follow, that law was assumed in the derivation given. Actually, the result would have been the same had any other relation been assumed between temperature and gas density because, in the two steps of the reduction, the temperature factors cancel out. The reduction to 70° only puts all measurements on the basis of a common unit of composition; it does not imply that gas saturated at a higher temperature can be cooled to 70° without condensing some of the water.

Because the concentrations to be read in practice cover 5 or 6 orders of magnitude, whereas the circle is divided into only three decades, only values of the concentration (reduced to 70° F) below 1 mg/liter (at about 0° F) are marked with their correct decimals. Above 1 mg/liter the values of concentration opposite a given temperature are to be multiplied by 1,000.

Detailed directions for laying off the temperature scale are given in table 2. The number 1.017 in the fifth column is that by which vapor pressure in millimeters of mercury at 70° F must be divided to obtain concentration in milligrams per liter.

TABLE 2. *Data for inner scale on base disk*

Temperature ° F. The scale is marked with the temperatures at which saturated vapors, after reducing to 70° F, have the density marked at the same radius as the outer scale. See table 1.

Temperature		Vapor pressure[a]	Log vapor pressure[b]	Conversion factor	Log conversion factor	Log mg/liter at 70° F[c]	Angle	Label on scale
° *F*	° *C*	*mm*					*deg*	
−30.0	−34.4	0.180	2.2553	1.017	0.0073	2.2480	269.8	−30
−25.0	−31.7	.240	2.3802	.....	.....	2.3729	284.7	.....
−20.0	−28.9	.320	2.5052	.....	.....	2.4979	299.7	−20
−15.0	−26.1	.426	2.6294	.....	.....	2.6221	314.6	.....
−10.0	−23.3	.563	2.7505	.....	.....	2.7432	329.2	−10
−5.0	−20.5	.740	2.8692	.....	.....	2.8619	343.4	.....
0	−17.7	.966	2.9850	.....	.....	2.9777	357.3	0
5.0	−15.0	1.241	0.0938	.....	.....	0.0865	10.4	.....
10.0	−12.2	1.602	.2047	.....	.....	.1974	23.7	10
15.0	−9.5	2.039	.3094	.....	.....	.3021	36.2	.....
20.0	−6.7	2.603	.4155	.....	.....	.4082	49.0	20
25.0	−3.9	3.308	.5196	.....	.....	.5123	61.5	.....
30.0	−1.1	4.182	.6214	.....	.....	.6141	73.7	30
35.0	1.7	5.181	.7144	.....	.....	.7071	84.8	.....
40.0	4.4	6.274	.7975	.....	.....	.7902	94.8	40
45.0	7.2	7.617	.8817	.....	.....	.8744	104.9	.....
50.0	10.0	9.209	.9642	.....	.....	.9569	114.8	50
55.0	12.8	11.08	1.0445	.....	.....	1.0372	124.5	.....
60.0	15.6	13.29	1.1135	.....	.....	1.1062	132.7	60
65.0	18.4	15.87	1.2006	.....	.....	1.1933	143.2	.....
70.0	21.1	18.76	1.2732	.....	.....	1.2659	151.9	70
75.0	23.9	22.24	1.3471	.....	.....	1.3398	160.8	.....
80.0	26.6	26.12	1.4170	.....	.....	1.4097	169.2	80
85.0	29.4	30.74	1.4877	.....	.....	1.4804	177.6	.....
90.0	32.2	36.07	1.5572	.....	.....	1.5499	186.0	90
95.0	35.0	42.18	1.6251	.....	.....	1.6178	194.1	.....
100.0	37.8	49.16	1.6916	.....	.....	1.6343	202.1	100
105.0	40.6	57.11	1.7567	.....	.....	1.7494	209.9	.....
110.0	43.3	65.82	1.8184	.....	.....	1.8111	217.3	110
115.0	46.1	76.04	1.8810	.....	.....	1.8737	224.8	.....
120.0	48.9	87.58	1.9424	.....	.....	1.9351	232.2	120

[a] Obtained from International Critical Tables, vol. 3, p. 210–12 (1926 ed.).
[b] In the first 7 entries 3.0000 was added to the logarithm for easier mathematical handling.
[c] Log milligrams per liter at 70° F = log vapor pressure minus log conversion factor.

4. Middle Disk

The middle disk is shown in figure 3. On the outer rim of the disk are located a pressure scale, an altitude scale, and two marks labeled F-12 and F-22. The pressure scale, which is marked Comparison Pressure (P_c), extends about three-quarters of the way around the disk. Intervals of this scale are proportional to the effect of a gage pressure on the fugacity [2] of water in the gas, and include corrections for the reduction of the fugacity of water vapor in the gas phase at high pressure and for the differences between gage pressure and absolute pressure. The scale was constructed by laying off angles corresponding to the logarithms of the adjusted absolute pressures, i. e., $P(1-KP+K'P^2)$ instead of P. Each point is marked with the corresponding gage pressure (absolute pressure minus 14.7 psi). Data used in the construction of the pressure scale and other details are given in table 3.

The altitude scale is used to correct the value of W_x when P_c is atmospheric pressure at a high altitude and is not directly measured. The correction is accomplished by subtracting an angle that corresponds nearly to the logarithm of the ratio of atmospheric pressure at the elevated altitude to to atmospheric pressure at sea level. The construction and use of the scale will be explained more fully later.

The two marks labeled F-12 and F-22 are used in connection with moisture determinations in Freon-12 and in Freon-22. Their use is explained in section 8, dealing with conversion of units.

5. Small Disk

The small disk (fig. 4) contains two pressure scales, indentical in angular intervals with the comparison pressure scale on the middle disk. The inner, or saturation pressure (P_s), scale is adjacent to the temperature scale on the base disk. The outer, or test gas pressure (P_x), scale is arranged for convenient use in connection with the comparison pressure scale on the middle disk, but the sequence of numbers and their logarithms runs in the opposite direction. Each scale is the reciprocal of the other; that is, an angular displacement in the direction of increasing readings of one scale produces multiplication, and angular displacement in the direction of increasing numbers of the other scale results in division. The small disk also carries a scale of temperatures from −30° to −100° F marked Frost Point below −30° F. It is, in effect, an extension of the temperature scale on the base disk and is used

[2] For the water vapor in two phases to be in equilibrium, it must have the same fugacity in each. For ideal gases fugacity is proportional to partial pressure.

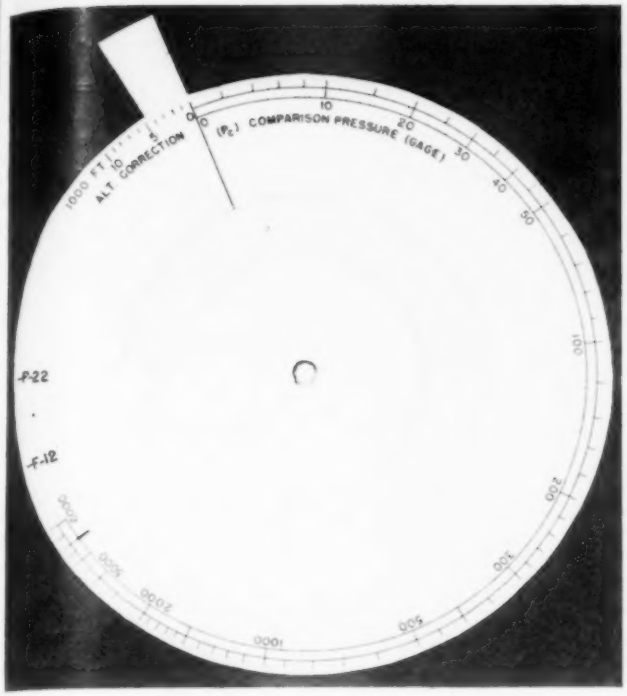

FIGURE 3. *Middle disk.*

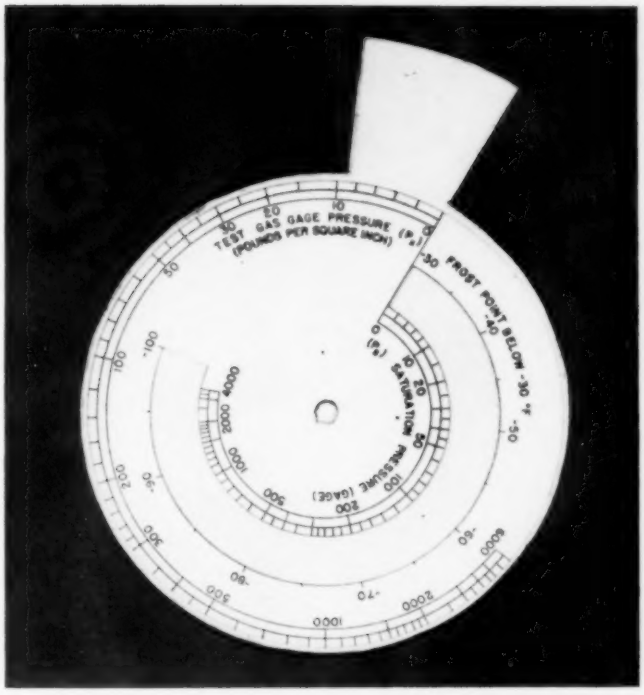

FIGURE 4. *Upper (small) disk.*

by setting the temperature of interest at the −30 mark of the temperature scale and reading the −30 mark of the frost point scale. Data and other details for the three scales of the small disk are given in table 4.

6. Mathematical Operations

The actual mathematical operations involved in solving eq (1) for W_x with the computer are (a) divide W_s by P_s by subtracting the angle corresponding to the logarithm of P_s from the angle corresponding to the logarithm of W_s, (b) multiply by P_w/P_x by adding the angle corresponding to the difference between the logarithm of 14.7 (if P_w is atmospheric pressure) and the logarithm of P_x, and, (c) multiply by P_c by adding the angle corresponding to the logarithm of P_c. (All pressures involved in this operation are the adjusted pressures obtained by multiplying the absolute pressure in pounds per square inch by the factor $[1-KP+K'P^2]$.) When P_w is greater than atmospheric pressure, multiply by $P_w/14.7$ by adding the angle corresponding to the difference between the logarithms of P_w (not adjusted)[3] and 14.7.

Problem 1 will serve to illustrate the most common use of the computer.

Problem 1: A high-pressure test gas containing an unknown amount of water (W_x) is matched with a comparison gas that is saturated at a pressure of 1,000 psig [4] (P_s) and at a temperature of 60° F (T_s). Identical readings of the indicator show that the two gases have the same fugacity, that is, each is in equilibrium with the same third phase, when the test gas is at a pressure of 6,000 psig (P_x) and the gas from the saturator is at a comparison pressure of 40 psig (P_c). What is the water content (W_x) of the test gas when expanded to one atmosphere at 70° F? *Solution:* Opposite the saturation temperature (T_s) of 60° F set the saturation pressure (P_s) of 1,000 psig. Without disturbing the previous setting, set the 0 of the comparison pressure scale (P_c) opposite the test gas pressure (P_x) of 6,000 psig. Opposite the comparison pressure (P_c) of 40 psig read the water content (W_x) of 0.0058 mg/liter at 70° F. A second use of the computer is in the determination of temperatures of condensation (dewpoints or frost points), as will be illustrated by problems 2 and 3:

Problem 2: What is the frost point of the gas considered in problem 1 when (a) discharged at atmospheric pressure, (b) reduced to a pressure of 100 psig? *Solution:* (a) Bring the right-hand edge of the wide tab to the water content at atmospheric pressure and 70° F, 0.0058 mg/liter. Opposite −30° on the temperature scale, read −81° on the scale indicating "frost point below −30° F." (b) Bring the zero of the P_c scale (the right-hand edge of the narrow tab) to 0.0058 mg/liter. Bring the right-hand edge of the wide tab to 100 psig on the P_c scale. Opposite −30° of the temperature scale

[3] Fugacity does not enter the correction of density for pressure, and the change can usually be assumed to be ideal. When dewpoints are calculated, the effect of gas pressure on fugacity must be considered, and P_w is to be "adjusted" like the other pressures [4].

[4] Psig is the abbreviation for pounds per square inch gage i. e., above barometric pressure.

TABLE 3. *Data for comparison pressure scale on middle disk*

The scale is proportional to the logarithms of the absolute pressures corrected for deviations from the ideal gas laws, but is marked with uncorrected gage pressures when the barometric pressure is 14.7 psi.

Pressure		$P^2\times10^{-5}$	KP $(1.9\times10^{-4}P)$	$(1-KP)$	$K'P^2$ $(1.4\times10^{-5}P^2)$	$(1-KP+K'P^2)$	Adjusted pressure	Log of adjusted pressure −1.0000	Angle	Label on scale
psig	*psia*						*psia*		°	
0	14.7	0.00000216	0.0028	0.9972	0	0.9972	14.7	0.1673	20.1	0
2	16.7	.00000279	.0032	.9968	0	.9968	16.6	.2201	26.4	.....
4	18.7	.00000350	.0036	.9964	0	.9964	18.6	.2695	32.3	.....
6	20.7	.00000428	.0039	.9961	0	.9961	20.6	.3139	37.7	.....
8	22.7	.00000515	.0043	.9957	0	.9957	22.6	.3541	42.5	.....
10	24.7	.00000610	.0047	.9953	0	.9953	24.6	.2909	46.9	10
15	29.7	.00000882	.0056	.9944	0	.9944	29.5	.4698	56.4	.....
20	34.7	.0000120	.0066	.9934	0	.9934	34.5	.5378	64.5	20
25	39.7	.0000158	.0075	.9925	0	.9925	39.4	.5955	71.5	.....
30	44.7	.0000200	.0085	.9915	0	.9915	44.3	.6464	77.6	30
35	49.7	.0000247	.0094	.9906	0	.9906	49.2	.6920	83.0	.....
40	54.7	.0000299	.0104	.9896	0	.9896	54.1	.7332	88.0	40
45	59.7	.0000356	.0113	.9887	0	.9887	59.0	.7708	92.5	.....
50	64.7	.0000419	.0123	.9877	0	.9877	63.9	.8055	96.7	50
60	74.7	.0000558	.0142	.9858	0	.9858	73.6	.8669	104.0	.....
70	84.7	.0000717	.0161	.9839	0	.9839	83.3	.9206	110.5	.....
80	94.7	.0000897	.0180	.9820	0.0001	.9821	93.0	.9685	116.2	.....
90	104.7	.000110	.0199	.9801	.0002	.9803	102.6	1.0112	121.3	.....
100	114.7	.000132	.0218	.9782	.0002	.9786	112.2	1.0500	126.0	100
120	134.7	.000181	.0256	.9744	.0002	.9746	131.2	1.1179	134.1	.....
140	154.7	.000239	.0294	.9706	.0003	.9709	150.2	1.1767	141.2	.....
160	174.7	.000305	.0332	.9668	.0004	.9672	169.0	1.2279	147.3	.....
180	194.7	.000379	.0370	.9630	.0005	.9635	187.6	1.2732	152.8	.....
200	214.7	.000461	.0408	.9592	.0006	.9598	206.1	1.3141	157.7	200
220	234.7	.000574	.0446	.9554	.0008	.9562	224.4	1.3510	162.1	.....
240	254.7	.000648	.0484	.9516	.0009	.9525	242.6	1.3849	166.2	.....
260	274.7	.000755	.0522	.9478	.0011	.9489	260.7	1.4161	169.9	.....
280	294.7	.000868	.0560	.9440	.0012	.9452	278.6	1.4450	173.4	.....
300	314.7	.000990	.0598	.9402	.0014	.9416	296.3	1.4717	176.6	300
350	364.7	.00133	.0693	.9307	.0019	.9326	340.1	1.5316	183.8	.....
400	414.7	.00172	.0788	.9212	.0024	.9236	383.0	1.5832	190.0	.....
450	464.7	.00216	.0883	.9117	.0030	.9147	425.1	1.6285	195.4	.....
500	514.7	.00265	.0978	.9022	.0037	.9059	466.4	1.6687	200.2	500
600	614.7	.00378	.1168	.8832	.0053	.8885	546.2	1.7374	208.5	.....
700	714.7	.00511	.1358	.8642	.0072	.8714	622.8	1.7944	215.3	.....
800	814.7	.00664	.1548	.8452	.0093	.8545	696.2	1.8427	221.1	.....
900	914.7	.00837	.1738	.8262	.0117	.8379	766.8	1.8847	226.2	.....
1000	1015	.01030	.1928	.8072	.0144	.8216	833.9	1.9211	230.5	1000
1100	1115	.01243	.2118	.7882	.0174	.8056	898.2	1.9534	234.4	.....
1200	1215	.01476	.2308	.7692	.0207	.7899	959.8	1.9822	237.9	.....
1300	1315	.01729	.2498	.7502	.0242	.7744	1018	2.0078	240.9	.....
1400	1415	.02002	.2688	.7312	.0280	.7592	1074	2.0310	243.7	.....
1500	1515	.02295	.2878	.7122	.0321	.7443	1128	2.0523	246.3	.....
1600	1615	.02608	.3068	.6934	.0365	.7299	1179	2.0715	248.6	.....
1700	1715	.02941	.3258	.6742	.0412	.7154	1227	2.0888	250.6	.....
1800	1815	.03294	.3448	.6552	.0461	.7013	1273	2.1048	252.6	.....
1900	1915	.03667	.3638	.6362	.0513	.6875	1317	2.1196	254.4	.....
2000	2015	.04060	.3828	.6172	.0568	.6740	1358	2.1329	255.9	2000
2500	2515	.06325	.4778	.5222	.0886	.6108	1536	2.1864	262.4	.....
3000	3015	.09090	.5728	.4272	.1273	.5545	1672	2.2232	266.8	3000
3500	3515	.1236	.6678	.3322	.1730	.5052	1776	2.2494	269.9	.....
4000	4015	.1612	.7628	.2372	.2257	.4629	1858	2.2690	272.3	.....
4500	4515	.2038	.8578	.1422	.2853	.4275	1930	2.2856	274.3	.....
5000	5015	.2515	.9528	.0472	.3521	.3993	2002	2.3015	276.2	.....
5500	5515	.3042	1.0478	−.0478	.4259	.3781	2085	2.3191	278.3	.....
6000	6015	.3618	1.1428	−.1428	.5065	.3637	2188	2.3400	280.8	6000

[a] 1.0000 was subtracted from the logarithm for easier mathematical handling.

read −52° on the scale indicating "frost point below −30° F."

Problem 3: Gas at a pressure of 100 psig is saturated with water vapor at 90° F. What will be its dewpoint if expanded to 4 psig? *Solution:* Set 100 psig of the saturation pressure scale opposite 90° of the Temperature scale. Opposite 4 psig on the saturation pressure Scale, read 40° F, the dewpoint of the gas at 4 psig.

In a problem like those above, the test gas can be air, oxygen, nitrogen, or even Freon-12 at a pressure nearly up to its point of liquefaction, and the comparison gas can be any of the first three gases. These four gases have negligibly different properties insofar as they affect moisture determinations. Further, the test gas can also be Freon-22, which does not behave like the others except at low pressures, provided certain restrictions are observed. For Freon-22 at pressures up to 30 psig, the computer will give moisture readings directly with negligible error. Above 30 psig, the readings become progressively erroneous with increase of pressure, but they can be corrected for any single pressure, as explained below in the section on conversion of units.

TABLE 4. *Data for scales on the small disk*

Saturation Pressure, P_s, Scale

The saturation pressure, P_s, scale is the same as the comparison pressure, P_c, scale except that it reads only to 4,000 psi, and some of the labels are omitted. Labels: 0, 10, 20, 50, 100, 200, 500, 1000, 2000, 4000.

Test Gas Pressure, P_x, Scale

The test gas pressure, P_x, scale is the reverse of the P_c and P_s scales. The P_x scale starts at the same point as the P_s scale (20.1°) but it is laid out counterclockwise. Some labels are omitted.
Labels: 0, 10, 20, 30, 50, 100, 200, 300, 500, 1000, 2000, 6000.

Frost Point Below −30° F Scale

The scale is a continuation of the temperature scale arranged for convenient subtraction of angles from the point −30° F of that scale.

Temperature		Vapor pressure	Log vapor pressure[a]	Conversion factor	Log conversion factor	Log mg per liter[b]	Angle A	Angle B[c]	Label on scale
$-°F$	$-°C$	*mm* Hg					*deg*	*deg*	
30	34.5	0.1777	2.2497	1.02	0.0086	2.2411	269	21	−30
35	37.2	.1323	2.1216	.....	.....	2.1130	254	36	.....
40	40.0	.0996	1.9850	.....	.....	1.9764	237	53	−40
45	42.8	.0682	1.8338	.....	.....	1.8252	219	71	.....
50	45.6	.0497	1.6964	.....	.....	1.6878	202	88	−50
55	48.4	.0360	1.5563	.....	.....	1.5477	186	104	.....
60	51.1	.0258	1.4116	.....	.....	1.4030	167	123	−60
65	53.9	.0180	1.2553	.....	.....	1.2467	150	140	.....
70	56.8	.0124	1.0934	.....	.....	1.0848	130	160	−70
75	59.4	.0087	0.9395	.....	.....	0.9309	112	178	.....
80	62.2	.0059	.7708	.....	.....	.7622	92	198	−80
85	65.0	.0040	.6021	.....	.....	.5935	71	219	.....
90	67.7	.0027	.4314	.....	.....	.4228	51	239	−90
95	70.5	.0018	.2553	.....	.....	.2467	30	260	.....
100	73.2	.0012	.0792	.....	.....	.0706	8	282	−100

[a] 3.000 was added to logarithm for easier mathematical handling.
[b] Log milligrams per liter = log vapor pressure − log conversion factor.
[c] The angles in this column are oriented with respect to the −30 mark on the temperature scale on the base disk. Angle B = 290° − angle A.

7. Correction for Altitude (or Abnormal Barometric Pressure)

The various pressure scales involve the reduction of gage pressures to absolute pressures and are correct only when the barometric pressures is 14.7 psia, the normal pressure at sea level. When the barometer differs significantly from normal, a correct result can be obtained by adding the barometric pressure to each pressure reading, subtracting 14.7 psi, and using the corrected pressures instead of the observed ones on the computer.

As an example of this correction and at the same time of the convenient use of the outside scale as a slide rule, assume that the gage readings of problem 1 were obtained when the barometer reading was 600 mm of mercury instead of the normal 760. The instrument will first be used as a slide rule to convert the pressure in millimeters of mercury to pounds per square inch. Set an edge of one of the tabs as a marker over 760 (multiplied by any convenient power of 10) and an edge of the other disk over 600. Rotate the two disks together until the first marker reads 14.7. The second marker reads 11.6, the barometric pressure in pounds per square inch. The difference between 14.7 and 11.6 is 3.1 and is to be subtracted from each gage reading. P_s becomes 996.9 psig, P_x becomes 5,996.9 psig, and P_c becomes 36.9 psig. When these corrected pressures are used and the setting otherwise made as before, the reading obtained is 0.0053 mg/liter. In this case the correction of P_c is the only significant one; the others are outside the limit of accuracy of gages or computer.

The ordinary variations of the barometer at any one place can usually be neglected. Often the difference between the prevailing pressure at a testing station and sea level cannot. Corrections to sea-level conditions can always be made by the method described above, but this takes too much time when routine tests for compliance with a specification are being made. In the most convenient procedure for testing the dryness of compressed gases, the "comparison" gas is saturated at about 500 psig and is passed over the detector at or only slightly above atmospheric pressure to obtain P_c. The sample is then passed over the detector and its pressure, P_x, is adjusted until the galvanometer reading is the same as that of the comparison gas at P_c.

Substantially all Government and many commercial specifications limit the water content of "dry" gases to 0.02 mg (20 μg) per liter after expansion to 1 atm at 70° F. A scale, marked Alt. Correction, has been added at the lower end of the P_c scale by the use of which a gas that just meets the requirement of 0.02 mg/liter will show the same analysis under average pressures at each altitude. The scale was obtained by comparing, for various altitudes, the concentration of water corresponding to the same set of gage readings when reduced to absolute pressures and entered in the general eq (1). For example, when a gas containing 0.02 mg/liter at 1 atm and 70° F is measured by the procedure described when the barometric pressure is normal for sea level and the temperature is 70° F, the gage readings

TABLE 5. *Altitude-correction scale*

Angles are measured to left of 0 of scale.

Altitude, A	Barometric pressure[5]	Ratio of pressures	Ratio R	Log $R+1$	Angle	Label on scale
ft	*mm* Hg				*deg*	
0	760	1.000	1.000	.....	0	0
1,000	732.9	0.964	0.966	0.985	1.8	.....
2,000	706.6	.930	.933	.970	3.6	.....
3,000	681.1	.896	.901	.955	5.4	.....
4,000	656.3	.864	.871	.940	7.2	.....
5,000	632.3	.832	.841	.925	9.0	5
6,000	609.0	.801	.811	.909	10.92	.....
7,000	586.4	.771	.782	.893	12.84	.....
8,000	564.4	.743	.754	.877	14.76	.....
9,000	543.2	.715	.727	.862	16.56	.....
10,000	522.6	.688	.701	.846	18.48	10

are P_z=500 psig, P_x=445 psig, P_c=0 psig. The normal barometric pressure at an altitude of 10,000 ft is 10.1 psig instead of the normal 14.7 psig at sea level. By substituting corrected absolute pressures for the same gage readings in eq (1), we obtain, for sea level,

$$(W_x)_0=\frac{W_x(14.7)(14.7)}{514.7(1-515K+26523K')(459.7)(1-460K+21160K')},$$

and for 10,000 ft,

$$(W_x)_0=\frac{W_x(10.1)(14.7)}{510.1(1-510K+26010K')(455.1)(1-455K+20703K')},$$

from which

$$\frac{(W_x)_{10000}}{(W_x)_0}=0.701.$$

Hence, the 10,000-ft mark of the altitude correction is placed at an angle below the zero of the correction scale corresponding to the logarithm of 1/0.701. Table 5 shows the water contents corresponding to identical sets of gage pressures expressed as fractions of the water content at sea level computed in this manner. The alt. correction scale can be used with sufficient accuracy for most purposes if the comparison pressure is kept near atmospheric. However, when the comparison pressure is large, the alt. correction scale should not be used, but the gage pressures should be corrected for the abnormal barometric pressure, as described in the illustrative problem.

Table 6 shows the errors that result from failure to correct for altitude and from the use of the alt. correction scale in a number of typical cases. The last column in the table shows the correct result, computed from the basic eq (1).

8. Conversion of Units

The quantity of water in a gas is designated at various times and for several reasons by a variety of systems and units. It is often necessary or convenient to convert from one system to another.

TABLE 6. *Corrected and uncorrected water content, W, of gases producing selected sets of gage readings at 10,000 feet and a temperature of 70° F*

Observed gage readings			Computed value of W (μg/liter)		
P_c	P_x	P_z	Uncorrected for altitude	Corrected by "Alt" scale	Corrected by equation
psig	*psig*	*psig*			
0	300	301	28.58	20.00	20.00
0	300	450	20.08	14.07	13.90
0	300	3,100	4.951	3.47	3.43
0	500	100	50.21	35.10	35.57
0	3,500	100	20.08	14.07	14.34
32.5	500	2,000	19.82	13.89	18.11
500	500	2,000	198.0	138.7	198.5

The computer is designed to facilitate, particularly, interconversions among the following:

1. Weight of water per unit volume of gas at a standard temperature:
   a. Milligrams per liter at 70° F (almost identical with ounces per 1,000 cubic feet).
   b. Pounds per 10,000 cubic feet.
2. Weight of water per weight of gas:
   a. Parts per thousand when the gas is air.
   b. Parts per thousand when the gas is Freon-12.
   c. Parts per thousand when the gas is Freon-22.
3. Vapor pressure of water.
4. Dewpoint (frost point below 32° F).
5. Relative humidity.
6. Percentage by volume of vapor in gas.

The angular width of the large tab, on the small disk, is such that when the right edge (the 0 of the P_x and P_z scales) reads milligrams per liter, the left edge reads pounds per 10,000 cubic feet of gas on the outer scale of the base disk. The angular width is 24.7°, which is the angle corresponding to the logarithm of the factor for the conversion (see table 6).

The angular width of the narrow tab, on the middle disk, is such (9.5°) that when the right edge (the 0 of the P_c scale) reads milligrams per liter of air, the left edge reads parts per thousand parts by weight of air.

The narrow tab can also be used for reading milligrams of water per liter of gas at a definite pressure when the gas is Freon-22. The angular width of the narrow tab is such that when the right edge reads the apparent water content in milligrams per liter at a pressure of 120 psig, the left edge reads the correct water content in the same units at the same pressure in Freon-22. This is an empirical relation discovered when using the computer for determining water in the refrigerant in question. Not contemplated in the design, it is nevertheless useful when working with this particular material. For pressures up to 30 psig, as mentioned above, the computer will give directly a close approximation to the correct moisture readings for Freon-22. When the zero of the comparison pressure scale indicates

TABLE 7. *Data for tabs and for window slots*

Middle Disk	
Narrow Tab:	
Converts milligrams per liter to parts per thousand by weight, if the gas is air. The conversion is accomplished by dividing milligrams per liter by 1.20.	
Conversion factor	1.20 (based on density)
Log Conv. factor	0.0792
Angle	9.5°
Width of tab	9.5°
Right edge	20.1°
Left edge	10.6°
Slot:	
Length	280°
From	10°
To	290°
F-12 mark:	
Converts milligrams per liter to parts per thousand by weight when the gas is Freon-12.	
Conversion factor	197 (based on specific volume)
Log conv. factor	2.2945
Angle	275°
F-22 mark:	
Converts milligrams per liter to parts per thousand by weight when the gas is Freon-22.	
Conversion factor	274 (based on specific volume)
Log conv. factor	2.4378
Angle	293°
Small Disk	
Wide Tab:	
Converts milligrams per liter to pounds per 10,000 cubic feet, if the gas is air. The conversion is accomplished by dividing milligrams per liter by 1.6.	
Conversion factor	1.60
Log conv. factor	0.2041
Angle	34.5°
Width of tab	24.5°
Right edge	20.1°
Left edge	355.6°
Slot:	
Length	261.9°
From	20.1°
To	282.0°

milligrams per liter at 70° F, the 5,000 mark of the same scale (elongated to aid the memory) indicates percentage of water vapor by volume. This is another fortuitous coincidence.

The two marks labeled F-12 and F-22 are used to convert milligrams per liter to parts per thousand by weight (and parts per million, by moving the decimal point mentally) when the gas is Freon-12 or Freon-22. The angular distance between each labeled mark and the 0 mark of the comparison pressure scale corresponds to the logarithm of the factor of conversion. When the 0 mark reads milligrams per liter, the appropriate labeled mark reads parts per thousand by weight.

The vapor pressure of water in millimeters of mercury is numerically equal to 1.017 times the number of milligrams of water per liter at 70° F. The difference between this factor and unity is readable on the computer, but is so small it can be neglected in many cases, and the outer scale read directly as vapor pressure.

If the water content is less than 1 mg/liter, the dewpoint is read directly on the temperature scale under milligrams per liter on the outer scale. If the water content is more than 1 mg/liter (at about 0° F), the numbers on the outer scale must be multiplied by 1,000 to correspond to the dewpoint (frost point below 32° F) on the adjacent temperature scale. If the right edge of the wide tab, on the upper disk, is brought to the water content in milligrams per liter on the outer scale, the frost point is read on the scale marked "Frost point below −30° F" at the lowest point (−30° F) on the temperature scale. The decimal point must be watched carefully in this operation; it is not taken care of automatically. Compare with problems 2 and 3.

The relative amount of water in gases under two conditions is ascertained by finding an angle between the points representing concentrations under each condition. This angle can be set readily as that between the edges of the two protruding tabs. Then, if the middle disk is rotated, the small disk is carried along without disturbing the angle until one tab is above 1.0 of the outer scale on the base disk. The other tab then reads directly the ratio of concentration of water in the two cases. If one of the two conditions represents saturation, the ratio found is "relative humidity" as the term is ordinarily used.

Data for constructing the two tabs and the slots through which the temperature scale on the base disk is read, and for laying off the two marks labeled F-12 and F-22, are given in table 7.

9. Construction of Computer

The initial step in constructing the computer involves the making of large-sized ink drawings of each disk of the computer. These drawings are reduced photographically to the desired size, and the negatives are used to prepare stencils for use in an offset-printing press. The sections are printed on heavy white bond paper, and are permitted to dry overnight. The dry prints are cut out and trimmed with the aid of a special cutting tool similar to a beam compass, but with a sharp cutting edge instead of a drawing point. The cutouts are sandwiched

379949—56——3

between two layers of plastic for better wearability and easy handling. The sandwiching is performed on a laminating press, which uses heat and pressure to effect the bonding. The laminated sections are cut out and trimmed with the special cutting tool. The center holes are drilled on a drill press, care being taken to center the holes accurately. The three disks are assembled and a metal rivet is used to hold them together.

10. References

[1] E. R. Weaver and R. Riley, J. Research NBS **40,** 169 (1948) RP1865.
[2] E. R. Weaver and R. Riley, Anal. Chem. **20,** 216 (1948).
[3] E. R. Weaver, Anal. Chem. **23,** 1076 (1951).
[4] A. W. Diniak and E. E. Hughes (publication pending).
[5] W. G. Brombacher, J. Wash. Acad. **34,** 277 (1944).

WASHINGTON, June 23, 1955.

Journal of Research of the National Bureau of Standards Vol. 56, No. 5, May 1956 Research Paper 2675

[1] Vibrational Constants of Acetylene-d_2

Harry C. Allen, Jr., L. R. Blaine, and Earle K. Plyler

The infrared spectrum of acetylene-d_2 has been investigated in the region from 1 to 5 microns. The new data have enabled a consistent interpretation of the 16 bands in which only the stretching modes are excited. It is shown that there is a resonance interaction present between the vibrational levels (v_1,v_2,v_3) and (v_1-2,v_2,v_3+2) analogous to that present in C_2H_2. The new vibrational constants enable the calculation of band centers that are in excellent agreement with the observed band centers. By combining the photographic infrared results with those obtained in this work it is found that $B_0=0.84770 \pm 0.00007$ cm^{-1} and $D=(7.04 \pm 0.63)\times 10^{-7}$ cm^{-1}.

1. Introduction

The infrared spectrum of C_2D_2 has been studied by several workers. Recently, Saksena [1] [2] has observed and measured 12 bands in the photographic infrared region. He obtained an excellent value of B_0, but his efforts to evaluate vibrational constants were hampered by an insufficient knowledge of the spectrum at longer wavelengths. Subsequently, Talley and Nielsen [2] have published, in detail, their measurements on the spectrum from 500 to 7,800 cm^{-1}. These workers observed 39 bands, which were more than enough to evaluate the constants in the quadratic expression for the vibrational energy. Unfortunately, the constants they deduced do not satisfactorily account for the frequencies in the photographic region. It is believed that the difficulty arises from a second-order resonance due to the near equality of ν_1 and ν_3, because such an effect has been found in the spectrum [3] of C_2H_2. Furthermore, a new analysis of the band, $\nu_1-\nu_5^1$, near 2,167 cm^{-1} places this band center one line spacing higher than the previous work [4]. As the determination of the frequency of ν_1, which is not active in the infrared, depends directly on the frequency of this band, a new band center for this band leads to a new frequency for ν_1. This work was undertaken in order to obtain a more complete understanding of the C_2D_2 spectrum in view of the new value obtained for ν^1 and the suspected resonance interaction.

2. Experimental Procedure

The spectra were recorded on the two grating instruments of the Radiometry Section [5, 6]. The gas was prepared by M. Hellman of the Polymer Structure Section of the Bureau. The gas contained a small amount of C_2HD (<1 percent), which was not sufficient in quantity to interfere with the observations of the C_2D_2 bands. The region 1 to 2.8 μ was scanned with a 6-m cell and a pressure of 62 cm (Hg), and the region 3 to 5 μ was scanned with a 1-m cell and 28-cm pressure (Hg). Seventeen regions of absorption were observed, and some sections contained several overlapping bands. The pressure of the gas was varied for the different regions so that both the weak and the strong lines could be measured; the pressures in the slow-speed measurements ranged from 1 to 11 cm (Hg).

The frequencies of the rotational lines of the bands were measured by using the white-light fringes of a Fabry-Perot interferometer. The fringes served as a scale with a spacing of about 0.40 cm^{-1}. The maxima of the fringe system were determined in wavenumbers by using the wavenumbers of well-known emission lines of the noble gases. The emission lines, fringe system, and the absorption spectrum were recorded on a two-pen recorder. The absorption spectrum and the emission spectrum were detected by PbS and cooled PbTe cells, and the fringes were recorded with a 1P28 photomultiplier.

As an example of the spectrum of C_2D_2, a recorder trace on white paper was made of two regions. In figure 1 is shown the absorption band of one of the stretching vibrations, ν_3. The band center is at 2,439.24 cm^{-1}. It is overlapped by the weaker hot band at 2,433.76 cm^{-1}. Figure 2 is the trace obtained for the combination band $\nu_2+\nu_3$. It is overlapped by two weak bands.

3. Rotational Analysis

The bands were analyzed by first assigning J-values to the observed absorption peaks. An equation for each J-value was then obtained of the form

$$\nu=\nu_0+(B'+B'')m+(B'-B'')m^2+4Dm^3, \quad (1)$$

where $m=J+1$ for the R-branch and $m=-J$ for the P-branch. The set of equations for each band was solved by the method of least squares for the best estimates of ν_0, B', B'', and D. The calculations were carried out on SEAC, the NBS electronic computer. The observed line frequencies and rotational assignments are given for several of the stronger bands in table 1. Blank spaces correspond to lines too weak to measure precisely or to lines badly overlapped by lines of hot bands or atmospheric water-vapor absorption. The results of the analyses are given in table 2. The six strong bands in the photographic infrared region are also included. These bands were reanalyzed in order to have a consistent set of anal-

[1] This work was supported by the United States Atomic Energy Commission.
[2] Figures in brackets indicate the literature references at the end of this paper.

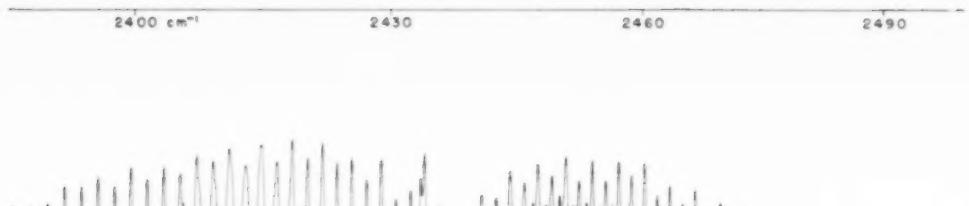

FIGURE 1. *Fundamental band ν_3 of C_2D_2.*
The pressure was 4 cm (Hg), and the cell length was 1 m.

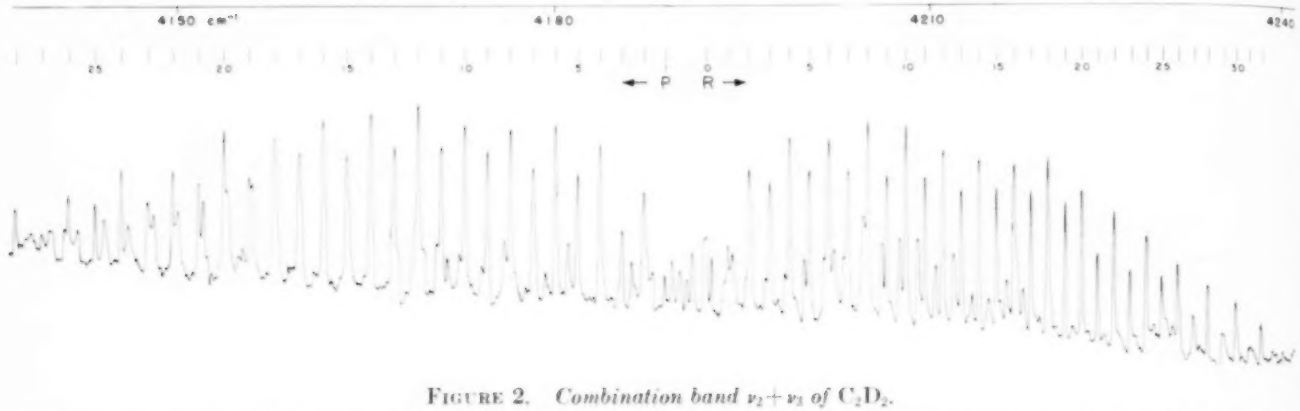

FIGURE 2. *Combination band $\nu_2+\nu_3$ of C_2D_2.*
The pressure was 11 cm (Hg), and the cell length was 6 m. Nonlabeled peaks belong to $\nu_2+\nu_3+\nu_4^1-\nu_4^1$ at 4181.22 cm^{-1} and $\nu_2+\nu_3+\nu_3^1-\nu_4^1$ at about 4187.0 cm^{-1}.

yses for a determination of B_0 and D. The B_0 and D values varied somewhat from band to band as can be seen from table 2. This variation is believed to arise from blended lines that could not be completely eliminated. The B_0 estimates were combined to get a best estimate for the constant. An average estimate was obtained by weighing each value according to the reciprocal of its estimated variance [7]. Such an averaging process gives $B_0=0.84770\pm0.00007$ cm^{-1} as a best estimate where the quoted uncertainty represents one standard deviation. It should be emphasized that the uncertainties quoted here and in table 2 are essentially an indication of the internal consistency of the measurements. They do not mean that the absolute frequencies of the band centers are known to the precision indicated, although the fit for the over-all spectrum would seem to indicate that the absolute frequencies are known to better than 0.1 cm^{-1}.

There is a wide spread in the individual values obtained for D. The quantity D is extremely small and such a spread is to be expected, especially since the analyses could not be extended to high J-values. An average value of D was obtained in a manner analogous to that used for B_0, giving $D=(7.04\pm0.63)\times10^{-7}$ cm^{-1}.

From the bands at 2,439 cm^{-1}, 4,190 cm^{-1}, and 6,868 cm^{-1}, values for α_1, α_2, and α_3 were determined as 0.00588 ± 0.00003 cm^{-1}, 0.00316 ± 0.00003 cm^{-1}, and 0.00442 ± 0.00002 cm^{-1}, respectively. Unfortunately these constants do not predict the excited state inertial constants as well as those suggested by Saksena, even after the resonance correction has been applied. This is a bit puzzling because these values are apparently more reliable than his, for he did not allow for the effect of any resonance in his work, and the present values were determined from levels involving fewer quanta of excitation.

TABLE 1. *Wave numbers of lines in C_2D_2 bands (cm^{-1}_{vac})*

J	$\nu_3-\nu_4$ $\nu_0=1928.596$		$\nu_1-\nu_5$ $\nu_0=2167.481$		ν_3 $\nu_0=2439.236$		$\nu_2+\nu_3$ $\nu_0=4190.577$		$\nu_1+\nu_3$ $\nu_0=5097.17$		$\nu_1+\nu_2+\nu_3$ $\nu_0=6828.816$	
	$R(J)$	$P(J)$	$R(J)$	$P(J)$	$R(J)$	$P(J)$	$R(J)$	$P(J)$	$R(J)$	$P(J)$	$R(J)$	$P(J)$
0	.....	.....	.....	.....	2440.87	.....	4192.12	.....	.....	.....	6829.85	.....
1	.....	.....	.....	.....	.....	.....	4193.92	.....	5100.52	5094.98	6831.54	6826.59
2	1933.59	.....	.....	.....	2444.22	.....	4195.58	4187.15	5102.15	5093.46	6833.14	6824.78
3	1935.27	.....	.....	.....	2445.92	.....	4197.23	4185.48	5103.78	5092.02	6834.65	.....
4	1936.94	1921.78	2175.78	.....	2447.58	.....	4198.83	4183.72	5105.42	5090.38	6836.29	6821.24
5	1938.56	1919.99	2177.37	.....	2449.25	.....	4200.43	.....	5106.96	5088.52	6837.80	6819.40
6	1940.18	.....	2179.04	2157.20	2450.86	.....	4201.98	4180.17	5108.49	5086.73	6839.23	6817.57
7	.....	1916.50	2180.58	2155.34	2452.46	.....	4203.58	4178.40	5110.02	5084.88	6840.80	6815.72
8	1943.38	1914.78	2182.20	2153.56	2454.10	2425.42	4205.13	4176.60	5111.54	5083.04	6842.21	6813.84
9	1945.04	1912.97	2183.76	2151.74	2455.65	2423.66	4206.67	4174.78	5112.99	5081.20	6843.66	6811.94
10	.....	1911.18	2185.30	2149.94	2457.28	2421.88	4208.22	4172.99	5114.45	5079.31	6845.02	6810.00
11	1948.16	1909.42	2186.81	2148.12	2458.90	2420.16	4209.72	.....	5115.93	5077.36	6846.41	6808.01
12	1949.73	1907.62	2188.33	2146.26	2460.44	2418.36	4211.24	4169.26	5117.37	5075.46	6847.74	6806.02
13	1951.28	1905.78	2189.94	2144.46	2462.00	2416.61	4212.72	4167.38	5118.71	5073.55	6849.00	6804.02
14	1952.84	1903.96	2191.42	2142.54	2463.58	2414.80	4214.18	4165.47	5120.09	5071.51	6850.27	6801.99
15	1954.36	1902.14	2192.86	2140.70	2465.12	2412.90	4215.61	4163.56	5121.47	5069.58	6851.61	6799.95
16	1955.91	1900.28	2194.34	2138.82	2466.69	2411.12	4217.05	4161.68	5122.84	5067.55	6852.87	6797.79
17	1957.44	.....	2195.76	2136.92	2468.23	2409.25	4218.48	4159.75	5124.13	5065.61	6854.04	6795.74
18	1958.92	.....	2197.24	2134.97	2469.74	2407.38	4219.88	4157.77	5125.44	5063.54	6855.19	6793.52
19	1960.43	1894.73	2198.74	2133.08	2471.28	2405.47	4221.26	4155.80	5126.72	5061.40	6856.36	6791.36
20	1961.91	1892.82	2200.15	2131.10	2472.80	2403.67	4222.62	4153.81	5127.97	5059.32	6857.51	6789.15
21	1963.40	1890.94	2201.56	2129.20	2474.26	2401.74	4223.99	4151.85	5129.21	5057.16	6858.58	6786.96
22	1964.84	.....	.....	2127.20	2475.75	2399.87	4225.32	4149.79	5130.39	5055.03	6859.67	6784.70
23	.....	1887.13	2204.36	2125.24	2477.26	2397.98	4226.68	4147.76	5131.60	5052.91	6860.70	6782.46
24	.....	.....	2205.76	2123.26	2478.70	2396.09	4227.98	4145.72	5132.74	5050.86	6861.75	6780.09
25	1969.16	1883.28	.....	2121.30	2480.17	2394.20	4229.28	4143.68	5133.87	5048.56	6862.71	6777.76
26	1970.63	1881.29	.....	2119.29	2481.64	2392.38	4230.56	4141.60	5135.03	5046.40	6863.68	6775.38
27	1972.06	1879.33	.....	2117.24	2483.07	.....	4231.83	4139.52	5136.15	5044.26	6864.62	.....
28	1973.44	.....	.....	.....	2484.49	2388.48	4233.06	4137.48	5137.23	5041.82	6865.54	6770.55
29	1974.80	.....	.....	.....	2485.95	2386.58	4234.34	4135.39	5138.25	5039.50	6866.36	6768.16
30	1976.21	.....	.....	.....	2487.28	2384.72	.....	4133.20	5139.28	5037.30	6867.27	6765.74
31	.....	.....	.....	.....	2488.70	2382.55	.....	4131.04	.....	5035.04	6868.12	6763.27
32	.....	.....	.....	.....	2490.14	2380.71	.....	.....	.....	.....	6868.85	.....
33	.....	.....	.....	.....	2491.50	.....	.....	.....	.....	.....	.....	.....

TABLE 2. *Observed bands and rotational constants of C_2D_2*

Observed	Upper v_1	v_2	v_3	l_4^l	l_5^l	Lower v_1	v_2	v_3	l_4^l	l_5^l	B_0	$B'-B''$	$D\times10^7$	B''
cm^{-1}														0.84764 ±.00020
1928.596 ±.005			1						1^1					.84825 ±.00035
2167.481 ±.008	1									1^1				.84710 ±.00100
2433.76 ±.02			1	1^1					1^1					
2439.236 ±.009			1								0.84741 ±.00034	0.00442 ±.00002	5.98 ±2.32	
2944.49 ±.03			1	1^1										
3234.82 ±.02	1				1^1									
4190.577 ±.004		1	1								.84714 ±.00019	.00758 ±.00001	3.99 ±1.50	
5083.72 ±.04	1		1	1^1					1^1					
5097.17 ±.02	1		1								.84830 ±.00077	.01041 ±.00004	10.40 ±5.9	
5197.66 ±.02		1	1	1^1	1^1						.84508 ±.00099	.00131 ±.00009		
5907.64 ±.01	2				1^1						.84693 ±.00053	.01125 ±.00003		
6828.816 ±.007	1	1	1								.84759 ±.00029	.01346 ±.00002	9.73 ±2.14	
7733.85 ±.02	2		1								.84405 ±.00116	.01637 ±.00008		
8550.11 ±.03[a]	1	2	1								.84706 ±.00133	.01637 ±.00009	24.72 ±13.52	
8652.880 ±.006[a]		1	3								.84812 ±.00026	.01644 ±.00001	9.95 ±2.11	
9444.517 ±.004[a]	2	1	1								.84773 ±.00017	.01914 ±.00001	4.38 ±1.70	
9794.069 ±.003[a]	1		3								.84774 ±.00017	.01966 ±.00001	8.30 ±2.76	
10347.931 ±.004[a]	3		1								.84761 ±.00017	.02186 ±.00001	6.47 ±1.88	
11492.666 ±.002[a]	1	1	3								.84794 ±.00013	.022457 ±.000008	8.94 ±1.24	

[a] Data from reference [1].

4. Vibrational Analysis

The new band center of $\nu^1-\nu_5^1$, together with the previously measured value [2] of $\nu_5^1=537.81$ cm^{-1}, is sufficient to determine the infrared fundamental ν_1 as 2,705.29 cm^{-1}. In order to obtain enough band centers to evaluate the nine constants involving only the stretching modes in the vibrational energy expression,

$$\nu_0=\sum_{i=1}^{3}\omega_i^0 v_i-\sum_{i=1}^{3}\sum_{j\geq i}^{3}X_{ij}v_iv_j+\ldots, \qquad (2)$$

it is necessary to use some of the bands observed in the photographic infrared. However, with one exception, these are just the bands whose excited states were suspected of having resonance interactions. The criterion for resonance is that the two energy levels have quantum numbers (v_1, v_2, v_3) and (v_1-2, v_2, v_3+2). In order to eliminate the resonance effects so the X_{ij}'s could be determined, only the average of the levels suspected of resonating were used. In this way 9 equations can be formed to evaluate the 9 constants in (2). These equations are given in table 3. A straightforward evaluation of these constants leads to the values given in table 4.

If one calculates the observed energy levels by using these constants, it is found that the levels suspected of resonating are not predicted correctly, thus confirming the presence of the resonance interaction. The results of such a calculation are given for unperturbed levels in table 5, column 3.

TABLE 3. *Equations used to evaluate the vibrational constants of* C_2D_2

$$2705.29=\omega_1^0-X_{11}.$$
$$2439.24=\omega_2^0-X_{22}.$$
$$4190.58=\omega_3^0+\omega_2^0-X_{22}-X_{23}-X_{33}.$$
$$5097.17=\omega_1^0+\omega_3^0-X_{11}-X_{13}-X_{33}.$$
$$6828.82=\omega_1^0+\omega_2^0+\omega_3^0-X_{11}-X_{22}-X_{23}-X_{12}-X_{13}-X_{33}.$$
$$8550.11=\omega_1^0+2\omega_2^0+\omega_3^0-X_{11}-4X_{22}-X_{23}-2X_{12}-X_{13}-2X_{33}.$$
$$9198.70=\omega_1^0+\omega_2^0+2\omega_3^0-2X_{11}-X_{22}-5X_{33}-X_{12}-X_{13}-2X_{23}.$$
$$10071.00=2\omega_1^0+2\omega_3^0-5X_{11}-5X_{13}-3X_{33}.$$
$$11764.77=2\omega_1^0+\omega_2^0+2\omega_3^0-5X_{11}-X_{22}-5X_{13}-2X_{12}-3X_{33}-2X_{23}.$$

TABLE 4. *Vibrational constants of* C_2D_2 (cm^{-1})

$\omega_1^0=2717.74$	$X_{11}=12.45$	$X_{12}=19.64$
$\omega_2^0=1774.86$	$X_{22}=5.24$	$X_{13}=47.34$
$\omega_3^0=2452.14$	$X_{33}=12.90$	$X_{23}=18.28$
$\gamma=23.86\ (1-0.20\ v_2)$		$X_{14}=7.97$
		$X_{15}=8.28$
$\omega_4^0-X_{44}-g_{44}=510.64$ [a]		$X_{44}=5.48$

[a] Following G. Herzberg, Infrared and Raman spectra of polyatomic molecules (D. Van Nostrand Co., Inc., New York, N. Y., 1945). The additive constant from the rotational constant is absorbed into the g_{44} term.

The theory of this second-order resonance has been worked out adequately and is in the literature [3, 8]. It is found that the matrix element connecting the resonating levels, to a second order of approximation, is,

$$(v_1,v_2,v_3|E|v_1-2,v_2,v_3+2)=\tfrac{1}{2}\gamma[v_1(v_1-1)(v_3+1)(v_3+2)]^{\frac{1}{2}}, \qquad (3)$$

where to this degree of approximation, γ is a constant, which depends on the coefficients of the cubic and quartic terms in the potential-energy expansion. In the case of C_2D_2, it is found, as was found for water vapor [9] and hydrogen cyanide [10], that γ is also a function of the vibrational quantum numbers. The presence of $v_2>0$ in a pair of resonating levels seems to have a very marked effect on γ, although pairs of levels in which $v_2=0$ seem to be accounted for by a constant γ. When more bands are available a dependence of γ on v_1 and v_2 will undoubtedly be found. The expression for γ given in table 4 gives the fit shown in table 5. Column 4 gives the band centers after the resonance correction has been applied to the upper-state levels. The bands with upper states that resonate are indicated by a bracket. In cases where only one-half the resonating pair has been observed, the other half has been calculated and included in the table. The fit obtained in this work is superior to either of the two previous determinations with the exception of the bands, (0,0,5) and (2,0,3). The possibility of wrong assignments is extremely unlikely. The difficulty is believed to arise from the omission of terms cubic in the vibrational quantum numbers from eq (2). For instance, a coefficient of v_3^3 as small as 0.1 cm^{-1} would make a difference of 12.5 cm^{-1} in the calculated value of the (0,0,5) band and drastically affect the perturbed levels. With present data, it is not possible to evaluate the cubic terms in eq (2). It is felt that the excellence of the fit for other bands is sufficient justification for the inclusion of the resonance interaction.

TABLE 5. *Vibrational spectrum of* C_2D_2 *bands involving only* v_1, v_2, *and* v_3

Observed	Upper state v_1 v_2 v_3	Calculated	
		Unperturbed	Perturbed
cm^{-1}			
	1	1769.62	
2439.24	1	2439.24	
	1	2705.29	
4190.58	1 1	4190.58	
5097.19	1 1	5097.19	
6828.89	1 1	6828.89	
	3	[7240.32]	7236.84
7730.60	2 1 1	[7730.24]	7733.70
8550.12	1 2 1	8550.11	
8952.89	1 3	[8955.10]	8952.87
9444.51	2 1 1	[9442.30]	9444.53
9794.06	1 3	[9803.59]	9794.19
10347.92	3 1	[10338.39]	10347.79
	2 3	[10659.40]	10658.14
11146.0	2 2 1	[11143.88]	11145.15
11492.66	1 1 3	[11498.73]	11492.64
12036.87	3 1 1	[12030.81]	12036.90
11905.34	5	11938.20	11924.21
12344.50	2 3	12341.96	12338.61
	4 1	12921.96	
13181.9	1 2 3	13183.39	13179.93
	3 2 1	13712.75	13716.21

As a result of the analysis of several hot bands in the course of this work it is possible to evaluate some of the interaction terms in eq (2) between the stretching modes and the bending modes. For example, from ν_3 and $\nu_3+\nu_4^1-\nu_4^1$, X_{34} can be obtained, and from $\nu_2+\nu_3+\nu_4^1-\nu_4^1$ the sum of X_{24} and X_{25} can be obtained. Likewise from ν_3 and $\nu_3-\nu_4^1$ a value for ν_4^1 can be obtained. The interaction terms that could be determined unambiguously are given in table 4. In addition, P- and R-branch transitions were resolved for several bands involving ν_4^1 and ν_5^1, for which only Q-branches were previously reported. The band centers of these bands are also listed in table 2. Only bands for which improved values could be obtained are included. It is felt that there are not enough bands, in which ν_4 and ν_5 are excited, to make it worthwhile to evaluate all the anharmonic and interaction terms at this time. It seems highly likely, as ν_4^1 and ν_5^1 are separated by only 27 cm^{-1}, that there should also be a second-order resonance between levels with quantum numbers $(v_1v_2v_3v_4v_5^l)$ and $(v_1v_2v_3v_4^l+2,v_5^l-2)$. Such an interaction, if present, cannot be found in the presently available data. Although this work accounts for a large part of the spectrum, there is still much work to be done before the spectrum is completely understood. This will have to await the precise measurement of a sufficient number of appropriate bands.

In conclusion, the authors express their appreciation to M. Hellman for preparing the compound, and to Joseph Cameron and Carroll Dannemiller for carrying out the computations on SEAC.

5. References

[1] B. D. Saksena, J. Chem. Phys. **20,** 95 (1952).
[2] R. M. Talley and A. H. Nielsen, J. Chem. Phys. **22,** 2030 (1954).
[3] N. H. Nordin and R. N. H. Haslam, Can. J. Research [A] **26,** 279 (1948).
[4] H. C. Allen, Jr., and E. K. Plyler, J. Chem. Phys. (in press).
[5] N. Gailar and E. K. Plyler, J. Research NBS **48,** 392 (1952) RP2327.
[6] E. K. Plyler, L. R. Blaine, and W. S. Connor, J. Opt. Soc. Am. **45,** 102 (1955).
[7] W. G. Cochran and S. P. Carroll, Biometrics **9,** 447 (1953).
[8] B. T. Darling and D. M. Dennison, Phy. Rev. **57,** 128 (1940).
[9] W. S. Benedict and E. K. Plyler (private communication).
[10] H. C. Allen, Jr., E. D. Tidwell, and E. K. Plyler, J. Chem. Phys. (in press).

Washington, December 12, 1955.

Journal of Research of the National Bureau of Standards Vol. 56, No. 5, May 1956 Research Paper 2676

Heat Capacity of Polyisobutylene From 0° to 380° K [1]

George T. Furukawa and Martin L. Reilly

Measurements of the heat capacity of polyisobutylene of the viscosity average molecular weight of 1.35×10^6 were made from about 14° to 380° K by means of an adiabatic calorimeter. The glass-transformation temperature was estimated to be 199° K. The values of the heat capacity above the glass-transformation temperature can be represented within ±0.2 percent by

$$C(\text{abs j deg}^{-1}\text{ g}^{-1}) = 0.844 + 3.03\times10^{-3}T + 2.24\times10^{-6}T^2.$$

The data were used to obtain smoothed values of heat capacity, enthalpy, entropy, and Gibbs free energy from 0° to 380° K.

1. Introduction

This paper deals with one of a series of heat-capacity investigations on rubber polymers and related substances to obtain thermodynamic information. Ferry and Parks [1] [2] measured the heat capacity of polyisobutylene of an average molecular weight of about 4,900, as determined from cryoscopic measurements, in the range from 118° to 295° K. The heat-capacity measurements presented in this paper were made from about 14° to 380° K on a polyisobutylene sample of the viscosity average molecular weight of 1.35×10^6. The results above the glass-transformation temperature (199° K) were found to be representable within ±0.2 percent by a quadratic equation. The data were used to obtain a table of smoothed values of heat capacity, enthalpy, entropy, and Gibbs free energy from 0° to 380° K.

2. Apparatus and Method

The measurements of the heat capacity were made by means of an adiabatic calorimeter similar in design to that described by Southard and Brickwedde [2]. Details of the design and operation of the calorimeter and accessory apparatus have been given previously by Scott et al. [3]. Briefly, the experimental method was as follows: The polymer sample was sealed in a copper container provided with vanes to promote rapid dissipation of heat and with a central well for a platinum-resistance thermometer and heater assembly. The container was suspended within the evacuated adiabatic shield system which was maintained at the same temperature during the heat-capacity experiments as that of the sample container surface by controlling shield heaters, using multiple junction constantan-chromel-P thermocouples to integrate surface temperatures. The outer surface of the container and the adjacent shield surface were gold-plated and polished to minimize heat transfer by radiation. The vacuum surrounding the container and shield was 10^{-5} mm of Hg or better. The electric-power input to the calorimeter heater (100 ohms) was measured by means of a Wenner potentiometer in conjunction with a volt box. The duration of each heating interval was measured with an interval timer operated on 60-cycle standard frequency furnished by the Radio Section of the Bureau. The timer was compared periodically with time signals from the Bureau's Time Section and was found to vary not more than 0.02 sec for a heating period that was never less than 2 min.

The temperature measurements were made by using a platinum-resistance thermometer in conjunction with a Mueller bridge. The thermometer was calibrated above 90° K in accordance with the 1948 International Temperature Scale [4], and between 10° and 90° K with a provisional scale [5], which consists of a set of platinum-resistance thermometers calibrated against a helium-gas thermometer. The provisional scale, as used in the calibration, was based on the value of 273.16° K for the temperature of the ice point and 90.19° K for the temperature of the oxygen point.

3. Sample

The polyisobutylene investigated was a portion of a larger sample designated as Vistanex B–100, which had been selected from a regular production run at the Esso Standard Oil Co. plant at Elizabeth, N. J. The molecular weights of this polymer determined from the average of intrinsic viscosities and from the light-scattering measurements have been reported by Marvin [6] to be, respectively,

$$M_v = 1.35\times10^6$$

and

$$M_w = 1.56\times10^6.$$

Information regarding other physical properties of this polymer sample can be found in the reference cited [6]. According to the analysis made by Esso Standard Oil Co., the sample contained 0.01 percent of ash and about 0.1 percent of paratertiarybutylcresol as stabilizer. The sample was used in the heat-capacity investigations without further treatment.

The polyisobutylene sample was cut, as in the previous heat-capacity studies of polymers [7,8,9], to fit between the vanes of the calorimeter sample

[1] The work discussed herein was performed as a part of the research project sponsored by the National Science Foundation, Polymer Research Group, in connection with the Government synthetic rubber program.

[2] Figures in brackets indicate the literature references at the end of this paper.

container. After filling, the sample was pumped at high vacuum for several weeks to eliminate as much of the volatile impurities as possible. The sample (40.736 g) was finally sealed in the container, along with a small quantity of helium gas to permit rapid thermal equilibrium during the calorimetric experiments.

4. Results

The heat-capacity measurements were made from about 14° to 380° K. The experimental details concerning heat treatments, temperature range of the measurements, and temperature drifts are summarized in table 1. The observed values of the heat capacity are given in table 2 and plotted in figure 1. As in the previous heat-capacity studies of polymers of butadiene and styrene [7,8,9] the polyisobutylene sample was subjected to two different rates of cooling prior to the heat-capacity experiments in order to obtain information on how the heat capacity was dependent upon the thermal history. In one series of measurements, by immersing the calorimeter in liquid nitrogen with helium gas in the space surrounding the sample container, the polymer was cooled from room temperature to 90° K in about 30 min and to 80° K in an additional 30 min. By this procedure a large portion of the polymer molecules was expected to be "frozen" in the higher states of energy.

In the second series of experiments, the polymer was cooled slowly over several days by maintaining a high vacuum in the space surrounding the container and by using different refrigerants successively. In the previous heat-capacity studies of polymers [7,9] that did not crystallize, the heat capacity in the region below the glass-transformation temperature seemed to be significantly dependent only upon the rate of cooling in the temperature range of the glass transformation. The polymer sample concerned in this investigation of the glass-transformation temperature 199° K, was cooled slowly only to 165° K and rapidly to lower temperatures (see table 1, run 5). The slow-cooling process was expected to allow more time for the polymer molecules to transform into states of lower energy.

TABLE 1. *Heat treatments and observations with polyisobutylene, Vistanex B–100*

Run	Treatment of sample	Temperature range of measurements	Temperature drift observations
		° K	
1	Cooled slowly to 80°, then rapidly to 53° K.	53 to 89	No drift.
2	Cooled slowly to 80°, then rapidly to 14° K.	14 to 62	Do.
3	Cooled rapidly from room temperature to 81° K.	81 to 218	Upward drift from 144° to 199°. Downward drift from 205° to 218°.
4	Cooled rapidly from room temperature to 205° K and heated to 213° K.	213 to 331	No drift.
5	Cooled slowly from room temperature to 165° K in 4 days. Cooled rapidly to 136° K, and heated to 143° K.	143 to 220	Downward drift from 160° to 220°.
6	Cooled slowly from 220° to 180° K, and heated to 208° K.	208 to 220	Downward drift from 208° to 220°.
7	Cooled slowly from 100° C to room temperature.	325 to 355	No drift.
8	Left at room temperature over night.	300 to 320	Do.
9	Left at room temperature for 2 days.	320 to 380	Do.
10	Cooled slowly to 300° K	300 to 330	Do.

TABLE 2. *Observed heat capacity of polyisobutylene, Vistanex B–100*

°K=°C+273.16°

T	C	T	C
Run 1		Run 4—Continued	
°K	*abs j deg⁻¹g⁻¹*	°K	*abs j deg⁻¹g⁻¹*
53.71	0.2627	242.80	1.711
54.55	.2679	252.99	1.752
56.22	.2773	263.00	1.794
59.16	.2941	272.88	1.838
62.68	.3146	282.59	1.878
65.85	.3336	292.23	1.920
69.35	.3545	302.85	1.968
73.59	.3804	314.27	2.019
78.06	.4091	325.56	2.070
82.65	.4390		
87.35	.4706	Run 5	
Run 2		147.46	0.8404
		156.18	.8939
14.43	0.0502	165.28	.9449
15.71	.0579	174.52	1.006
17.15	.0663	184.02	1.032
18.66	.0753	191.06	1.142
20.11	.0838	195.63	1.228
21.76	.0935	199.98	1.430
23.65	.1045	204.60	1.578
25.58	.1156	209.43	1.630
27.53	.1262	215.78	1.627
29.75	.1383		
32.40	.1526	Run 6	
35.48	.1688		
38.80	.1856	210.28	1.513
42.59	.2044	216.45	1.604
46.33	.2242		
50.16	.2445	Run 7	
54.92	.2700		
60.03	.2991	331.06	2.097
Run 3		341.38	2.142
		351.47	2.188
83.24	0.4439		
88.55	.4781	Run 8	
94.97	.5192		
102.40	.5698	305.21	1.981
111.49	.6256	314.42	2.021
120.63	.6844		
129.71	.7418	Run 9	
139.40	.8003		
148.54	.8575	325.41	2.072
157.88	.9111	346.24	2.166
168.14	.9701	366.68	2.257
178.01	1.022	377.14	2.301
187.55	1.073		
195.70	1.153	Run 10	
202.37	1.450		
208.56	1.576	310.59	2.004
215.23	1.603	321.39	2.054
Run 4			
216.56	1.609		
224.35	1.638		
233.33	1.673		

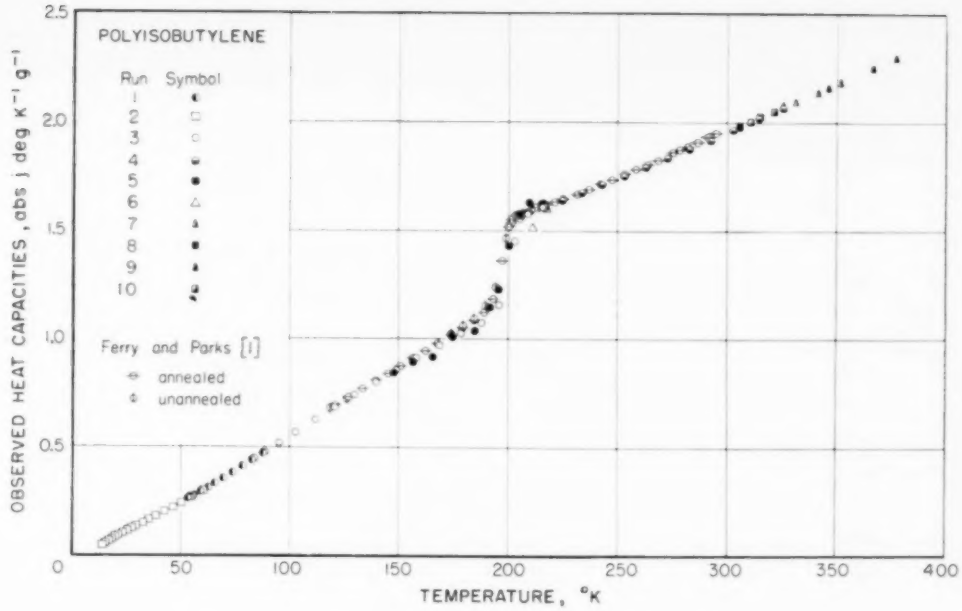

FIGURE 1. *Observed heat capacities of polyisobutylene.*

The measurements of run 3, with the sample shock-cooled, showed upward temperature drifts from about 144° to 199° K and downward drifts from about 205° to 219° K. The results of runs 5 and 6, made with the sample slowly cooled, showed downward temperature drifts from 160° to 220° K. It seems from these results that downward temperature drifts occurred in the temperature range from about 205° to 220° K, regardless of previous heat treatment. In run 4, however, when the sample was cooled rapidly from room temperature to 205° K and heated to 213° K, no drifts were observed in this range. Downward temperature drifts have been observed above the glass-transformation temperature with polymers that crystallize [7,8]. As the polymer melted slowly at certain temperatures above the glass-transformation temperature, heat was absorbed accompanied by downward temperature drifts. The downward temperature drifts from about 205° to 220° K observed with this polymer, however, are probably associated with glass transformation

During the initial measurements, the temperature drifts in the region of the glass-transformation temperature were followed for several hours. The results indicated that temperature equilibrium would not be attained within a reasonable length of time. Similar observations were made during heat-capacity measurements on other polymers [7,8,9]. Consequently no attempt was made in subsequent measurements on the polymer to reach temperature equilibrium in the region of the glass-transformation temperature. However, any reasonable change in the time intervals used is considered not to alter the general nature of the heat-capacity results obtained

The values of the heat capacity, in the region (210° to 380° K) above the glass-transformation temperature can be represented within ±0.2 percent (the average deviation being 0.1 percent) by the quadratic equation

$$C(\text{abs j deg}^{-1}\,\text{g}^{-1}) = 0.844 + 3.03\times10^{-3}T + 2.24\times10^{-6}T^2.$$

The constants were obtained by the method of least squares. Although the deviation of the observed heat-capacity values from this equation shows a small systematic trend, no attempt was made to obtain a better equation.

The heat-capacity data were used to obtain smoothed values of heat capacity, from which were derived the values, relative to 0° K, of enthalpy, entropy, and Gibbs free energy given in table 3. The values of the heat capacity below 14° K were obtained by extrapolation, using a Debye function fitted to the experimental values in the lowest temperature range. The method by which the derived thermal properties were obtained from the values of smoothed heat capacity has been described previously [7].

Upon consideration of various sources of errors, such as reproducibility of the physical state of the polymer, energy input, heat leak, and thermometry, the uncertainty in the heat-capacity values given in tables 2 and 3, except in the vicinity of the glass-transformation temperature and below 90° K, was estimated to be 0.3 percent. Below 90° K the uncertainty increases to 1 percent at 14° K. The uncertainty in the values of enthalpy, entropy, and Gibbs free energy, relative to 0° K, derived from the heat capacity was estimated to be 0.3 to 0.4 percent.

TABLE 3. *Heat capacity, enthalpy, entropy, and Gibbs free energy of polyisobutylene, Vistanex B–100*

T	C	$(H_T-H_{0°K})$	$(S_T-S_{0°K})$	$-(F_T-F_{0°K})$
°K	abs j deg^{-1}g^{-1}	abs j g^{-1}	abs j deg^{-1}g^{-1}	abs j g^{-1}
0	0	0	0	0
5	0.0023	0.0015	0.0007	0.0019
10	.0180	.0453	.0061	.0153
15	.0536	.2215	.0197	.0734
20	.0831	.5645	.0393	.2210
25	.1123	1.053	.0610	.4710
30	.1397	1.684	.0839	.8331
35	.1663	2.449	.1074	1.311
40	.1918	3.345	.1313	1.908
45	.2177	4.368	.1554	2.625
50	.2439	5.522	.1797	3.463
55	.2705	6.808	.2042	4.423
60	.2980	8.231	.2289	5.505
65	.3283	9.790	.2540	6.712
70	.3583	11.52	.2794	8.046
75	.3895	13.38	.3052	9.507
80	.4215	15.41	.3314	10.99
85	.4544	17.60	.3579	12.82
90	.4872	19.95	.3848	14.68
95	.5198	22.47	.4120	16.67
100	.5520	25.15	.4395	18.80
105	.5842	27.99	.4672	21.07
110	.6163	30.99	.4951	23.47
115	.6483	34.15	.5232	26.02
120	.6802	37.48	.5515	28.70
125	.7122	40.96	.5799	31.53
130	.7436	44.60	.6085	34.50
135	.7748	48.39	.6071	37.62
140	.8056	52.34	.6658	40.87
145	.8361	56.45	.6946	44.28
150	.8660	60.70	.7235	47.82
155	.8950	65.11	.7524	51.51
160	.9236	69.65	.7812	55.34
165	.9522	74.34	.8101	59.32
170	.9804	79.17	.8389	63.45
175	1.008	84.15	.8677	67.71
180	1.035	89.26	.8965	72.12
185	[a] 1.06			
190	1.10			
195	1.18			
200	[a] 1.42			
205	1.54			
210	1.58			
215	1.60			
220	1.620	144.0	1.161	113.1
225	1.640	152.2	1.205	118.9
230	1.661	160.4	1.241	125.1
235	1.681	168.8	1.277	131.4
240	1.702	177.2	1.313	137.9
245	1.722	185.8	1.348	144.5
250	1.743	194.5	1.383	151.3
255	1.764	203.2	1.418	158.3
260	1.785	212.1	1.452	165.5
265	1.806	221.1	1.486	172.8
270	1.827	230.2	1.520	180.4
273.16	1.840	235.9	1.542	185.2
275	1.848	239.3	1.554	188.1
280	1.870	248.6	1.588	195.9
285	1.891	258.0	1.621	203.9
290	1.913	267.5	1.654	212.1
295	1.934	277.2	1.687	220.5
298.16	1.948	283.3	1.708	225.8
300	1.956	286.9	1.720	228.0
305	1.978	296.7	1.752	237.7
310	2.000	306.7	1.784	246.5
315	2.022	316.7	1.817	255.5
320	2.045	326.9	1.849	264.7
325	2.067	337.2	1.880	274.0
330	2.090	347.6	1.912	283.5
335	2.112	358.1	1.944	293.1
340	2.135	368.7	1.975	302.9
345	2.158	379.4	2.007	312.9
350	2.181	390.3	2.038	323.0
355	2.204	401.2	2.069	333.3
360	2.227	412.3	2.100	343.7
365	2.250	423.5	2.131	354.2
370	2.274	434.8	2.162	365.0
375	2.297	446.2	2.192	375.8
380	2.321	457.8	2.223	386.9

[a] The values between 185° and 215° K, inclusive, were obtained graphically from the best curve drawn through the observed heat capacities.

5. Discussion

Ferry and Parks [1] previously determined the heat capacity of polyisobutylene of the number-average molecular weight of 4,900 from 118° to 295° K. Their results (see fig. 1) are generally about 1 to 2 percent higher than those obtained in the present investigation on a polyisobutylene sample of the viscosity average molecular weight of 1.35×10^6. The glass-transformation temperature (197° K) reported by Ferry and Parks is essentially the same as that (199° K) estimated from the results of the present measurements, the transformation temperature being taken as the temperature at the "half-height" of the upward sweep in heat capacity. The sharp decrease in heat capacity at the glass-transformation temperature was estimated to be about 26 percent. This percentage decrease is similar to those found in other polymers previously investigated [7, 8, 9].

The temperature drifts observed (see table 1), in the region of the glass-transformation temperature and immediately below, were similar to those of polymers previously investigated [7, 8, 9]. The discussion regarding these temperature drifts that are associated with glass transformation can be found in the references cited [7, 8, 9].

When the polymer sample was previously cooled rapidly (run 3), the enthalpy change obtained between 180° and 220° K was 53.27 abs j g^{-1}; when cooled slowly (run 5), the enthalpy change was 54.77 abs j g^{-1}. The difference indicates qualitatively the degree of the relaxation effects associated with glass transformation under the conditions of the experiments discussed. In a previous investigation [9], the enthalpy changes between 195° and 225° K, obtained under similar experimental conditions on a butadiene-styrene copolymer containing 22.61 weight percent of bound styrene, were 40.39 and 41.95 abs j g^{-1} when the sample was rapidly and slowly cooled, respectively.

6. References

[1] J. D. Ferry and G. S. Parks, J. Chem. Phys. **4,** 70 (1936).
[2] J. C. Southard and F. G. Brickwedde, J. Am. Chem. Soc. **55,** 4378 (1933).
[3] R. B. Scott, C. H. Meyers, R. D. Rands, Jr., F. G. Brickwedde, and N. Bekkedahl, J. Research NBS **35,** 39 (1945) RP1661.
[4] H. F. Stimson, J. Research NBS **42,** 209 (1949) RP1962.
[5] H. J. Hoge and F. G. Brickwedde, J. Research NBS **22,** 351 (1939) RP1188.
[6] R. S. Marvin, Proceedings of the Second International Congress on Rheology, No. 18, p. 156, July 26–31, 1953.
[7] G. T. Furukawa, R. E. McCoskey, and G. J. King, J. Research NBS **50,** 357 (1953) RP2425.
[8] G. T. Furukawa and R. E. McCoskey, J. Research NBS **51,** 321 (1953) RP2460.
[9] G. T. Furukawa, R. E. McCoskey, and M. L. Reilly, J. Research NBS **55,** 127 (1955) RP2610.

WASHINGTON, December 6, 1955.

Journal of Research of the National Bureau of Standards Vol. 56, No. 5, May 1956 Research Paper 2677

Preparation of Barium Titanyl Oxalate Tetrahydrate for Conversion to Barium Titanate of High Purity[1]

W. Stanley Clabaugh, Edward M. Swiggard, and Raleigh Gilchrist

A procedure is described for preparing barium titanyl oxalate tetrahydrate, $BaTiO(C_2O_4)_2 \cdot 4H_2O$, in which the mole ratio of TiO_2 to BaO is unity. To achieve this ratio the salt must be precipitated from solutions that do not contain sodium, potassium, or ammonium ions.

Ignition of barium titanyl oxalate tetrahydrate produces barium titanate, $BaTiO_3$. To prepare barium titanate free of strontium, the barium chloride used must be specially purified.

1. Introduction

Titanium forms an extensive series of compounds called titanates in which the titanium plays the role of an acidic constituent. Of particular interest have been barium titanate, $BaTiO_3$, and various titanates in which the barium has been partially replaced by strontium, magnesium, calcium, etc., and the titanium by zirconium or other acidic metals.

Owing to the possession of desirable dielectric and piezoelectric properties, these titanates, in recent years, have come into very extensive use in various electronic devices. In spite of their wide use the relationship between composition and electrical characteristics has not yet been fully worked out, in part because of the presence of minor components originating as impurities in the titanium dioxide and the barium carbonate used as starting materials in commercial production. The usual method of preparing barium titanate dielectrics is to calcine at specified temperatures mechanically-ground, intimate mixtures of titanium dioxide and barium carbonate.

The ultimate object of the work here described was to prepare barium titanate in which the mole ratio of barium to titanium was exactly unity and in which the impurities were reduced to an insignificant amount. This would enable the ceramic engineer to determine systematically the effect of various substituting elements on the electrical properties and to arrive at a composition that would reproducibly give the most desirable product.

2. Preparation of Barium Titanyl Oxalate, $BaTiO(C_2O_4)_2 \cdot 4H_2O$

Double oxalates of barium and titanium of the composition $BaC_2O_4 \cdot TiO(C_2O_4) \cdot xH_2O$ would be expected to yield on ignition a barium titanate in which the ratio of barium to titanium is exactly unity.

It has been known for some time that barium and titanium form an oxalate, described as a dihydrate, $BaTiO(C_2O_4)_2 \cdot 2H_2O$. This compound is said to be formed by the reaction of $K_2TiO(C_2O_4)_2$ with barium chloride [1].[2] Attempts to prepare this compound were not successful because potassium was not completely replaced by barium. The product always contained less barium than the stoichiometric amount. However, it was found possible to get the desired composition by slowly adding an aqueous solution of titanium tetrachloride and barium chloride, in which the two compounds are in nearly equimolar proportion but with barium in slight excess, to a hot solution of oxalic acid containing about 10 percent more of the acid than required for the desired double oxalate. The slight excess of barium and the somewhat greater excess of oxalate were intended to minimize competing reactions that might result in the formation of insoluble partially hydrolyzed compounds of titanium. The salt prepared in this way had the composition $BaTiO(C_2O_4)_2 \cdot 4H_2O$. The detailed procedure used in preparing it in batches of 240 g was as follows.

2.1. Procedure

Add 100 ml of highly purified titanium tetrachloride [2], drop by drop, to 100 to 150 ml of distilled water which is cooled in an ice bath. If the titanium tetrachloride is added slowly to the rapidly stirred distilled water, the resulting solution will be perfectly clear and free of hydrolyzed titanium. Dilute this solution to 500 ml and determine its titanium content. The exact titanium content must be known because the quantities of barium chloride and of oxalic acid to be used are based on this value. Dissolve 165 g (0.675 mole) of barium chloride dihydrate in 1,600 ml of distilled water and cool the solution to room temperature. To this solution add the volume of titanium tetrachloride solution that contains exactly 32 g (0.668 mole) of titanium. The barium chloride solution must be stirred constantly during the mixing and the temperature maintained at or below 30° C to prevent hydrolysis of the titanium.

Dissolve 185 g (1.47 moles) of oxalic acid dihydrate in 1,000 ml of distilled water in a 4-liter beaker, and heat the resulting solution on the steam bath to 80° C. It should be noted that the quantity of barium is 1 percent in excess and the quantity of

[1] Financial support of this work was furnished by the Diamond Ordnance Fuze Laboratories.

[2] Figures in brackets indicate the literature references at the end of this paper.

oxalate is 10 percent in excess of the stoichiometric amounts required to produce $BaTiO(C_2O_4)_2 \cdot 4H_2O$. This oxalate solution must be stirred constantly during the addition of the solution containing barium and titanium chloride. The use of a mechanical stirrer is recommended. Add the barium-titanium solution slowly. A convenient way to do this is by means of a separatory funnel mounted above the beaker. The rate of addition is readily adjusted by means of the stopcock on the funnel.

When the solution of barium-titanium chlorides first mixes with the solution of oxalic acid, a white flocculent precipitate forms which redissolves on stirring. The slow addition of the barium-titanium solution is continued until a dense crystalline form of barium titanyl oxalate tetrahydrate begins to precipitate. At this point the rate of addition may be increased slightly. However, the rate should not be increased to the point where the flocculent precipitate that first forms will not redissolve and form the desired dense precipitate. From 2 to 3 hours are required for the addition of the 2 liters of barium-titanium solution. At the end of the operation of mixing the 4-liter beaker is removed from the steam bath and the clear supernatant liquid decanted through a filter paper on a Büchner funnel. The precipitate is then washed by decantation with distilled water 5 or 6 times, transferred to the Büchner funnel, and again washed 5 or 6 times with distilled water. This precipitate will dry in the air and produce a fine, dry granular salt free of lumps or cakes. The drying may be hastened by drawing clean air through the salt for 3 to 4 hours.

The foregoing method was used many times in the preparation of batches of barium titanyl oxalate tetrahydrate which later were ignited to barium titanate. The mole ratio of TiO_2 to BaO, calculated from the results of the chemical analysis of the barium titanate resulting from the ignition of various batches of barium titanyl oxalate tetrahydrate, is given in table 1.

TABLE 1. *Mole ratio of* Ti *to* Ba *as calculated from the determinations of* TiO_2 *and* $BaSO_4$ *on 0.5000-g samples of* $BaTiO_3$ *formed by the ignition of various preparations of* $BaTiO(C_2O_4)_2 \cdot 4H_2O$ [a]

Batch	Sample	$BaSO_4$ found		TiO_2 found		Ratio of Ti to Ba
		g	*Mole*	*g*	*Mole*	
I	1	0.4995	2.140×10^{-3}	0.1712	2.143×10^{-3}	1.001
II	2	.4998	2.141	.1712	2.143	1.001
III	3	.5010	2.146	.1713	2.144	0.999
IV	4A	.5001	2.142	.1715	2.146	1.002
	4B	.5001	2.142	.1715	2.146	1.002
V	5A	.5004	2.144	.1712	2.143	1.000
	5B	.5004	2.144	.1713	2.144	1.000
VI	6A	.5004	2.144	.1713	2.144	1.000
	6B	.5005	2.144	.1713	2.144	1.000
VII	7A	.5003	2.143	.1712	2.143	1.000
	7B	.5004	2.144	.1712	2.143	1.000
VIII	8	.5008	2.145	.1712	2.143	0.999
IX	9	.5010	2.146	.1714	2.145	1.000
X	10	.5003	2.143	.1713	2.144	1.001
XI	11	.5008	2.145	.1712	2.143	0.999
XII	12	.5009	2.146	.1712	2.143	.999

[a] The 12 batches of $BaTiO(C_2O_4)_2 \cdot 4H_2O$ were finally placed in a single container and mixed by tumbling. A sample was removed and ignited to $BaTiO_3$. The oxalate compound was again tumbled and sampled. This operation was repeated a third time. Analysis of the three samples of $BaTiO_3$ gave the following results for the ratio of Ti to Ba: 1.000, 1.001, and 1.000.

3. Determination of Barium and Titanium in Barium Titanate

To determine barium and titanium, samples of the various batches of barium titanyl oxalate tetrahydrate were first ignited to barium titanate. Conversion was done by heating the oxalate salt in a furnace at 900° C, for convenience, overnight. A shorter period of ignition would probably have sufficed, but it was more convenient to heat overnight.

3.1. Analytical Procedure

Digest a 0.5-g sample of barium titanate with 15 ml of concentrated hydrochloric acid by heating it gently with a burner until the yellow color of the solution disappears. Add 15 ml of water and boil the solution gently until the sample dissolves completely.

It was observed that if the amount of basic constituent, on a mole basis, was equal to or greater than the amount of acid constituent the above procedure would effect complete solution of the sample.[1]

Dilute the solution containing the barium and titanium with 100 ml of water and add 50 ml of a solution of ethylenediamine tetraacetic acid made by dissolving 1.5 g of the reagent in 50 ml of water with enough ammonium hydroxide to effect solution. Next, adjust the acidity of the barium-titanium solution to *p*H 3.5 to 4.0 with diluted ammonium hydroxide. Heat the resulting solution to boiling and precipitate the barium as barium sulfate by adding 20 ml of a 25-percent aqueous solution of ammonium sulfate. This large excess of ammonium sulfate is necessary to precipitate the barium completely at *p*H 3.5 to 4.0 in the presence of the complexing agent. Digest the solution on the steam bath until the barium sulfate settles and the supernatant liquid becomes clear. Remove the precipitate by filtration, wash it with water, ignite it, weigh it as $BaSO_4$, and calculate its BaO content.

Acidify the combined filtrate and washings with 20 ml of concentrated sulfuric acid, cool the resulting solution to 10° C, and precipitate the titanium with cupferron. Ignite the precipitate and weigh it as TiO_2.

The use of ethylenediamine tetraacetic acid in the analytical separation of barium from titanium is essential because in its absence barium sulfate, even when precipitated from strongly acid solution, was found by qualitative spectrochemical examination to be contaminated by titanium. When the separation was made in the presence of the sequestering reagent, the qualitative spectrochemical examination indicated that the contamination was only 0.01 to 0.1 percent. The value of the mole ratio of Ti to Ba, when determined on the same batch of barium

[1] If, on the other hand, the acidic constituent was in excess, an insoluble residue would remain. Experience in analyzing the oxalate compound showed that when the titanium content significantly exceeded the unit ratio the resulting barium titanite did not dissolve completely. This behavior on solution furnished a rapid means of indicating excess titanium.

titanate, was 0.991 in the absence of ethylenediamine tetraacetic acid and 1.000 in the presence of the reagent.

4. Effect of Alkali Elements on the Composition of Barium Titanyl Oxalate

Titanium forms complexes with organic compounds such as oxalates, citrates, tartrates, etc., and this behavior is made use of to advantage in analyzing materials containing titanium. Ions such as potassium, sodium, ammonium, barium, etc., increase the stability of these titanium complexes. For example, if aqueous solutions of titanium tetrachloride and oxalic acid are mixed and boiled, the titanium will precipitate, even though a large excess of oxalic acid is present. The precipitated titanium will not redissolve in excess of either organic or mineral acid. If the acidity of the solution is made about *p*H 5 to 6 by adding sodium, potassium, or ammonium hydroxide, and the solution then heated, the titanium precipitate will redissolve. Once a solution of titanium is obtained by digesting with an alkali oxalate at *p*H 5 to 6, this solution can be boiled without the titanium precipitating, even if the acidity is increased to a value more acid than *p*H 1.

Attempts were made to prepare barium titanyl oxalate by adding solutions of barium chloride to hot solutions of alkali titanium oxalate, as well as by adding solutions of the alkali titanium oxalate to hot solutions of barium chloride. In each instance the amounts taken were such that the mole ratios were 1 barium to 1 titanium to 2 oxalate. The barium titanyl oxalates so prepared were then analyzed. The oxalate was determined by titrating with 0.1 *N* potassium permanganate in a perchloric acid solution. The barium and the titanium were determined as described in section 3. If the difference is assumed to be water, the compound had the formula $BaTiO(C_2O_4)_2 \cdot 4H_2O$. Results of the analysis of the salts prepared by means of the sodium, the potassium, and the ammonium titanium oxalates are given in table 2.

TABLE 2. *Composition of barium titanyl oxalate tetrahydrate prepared by means of sodium, potassium, and ammonium oxalates*

Batch	Ba per gram of salt	TiO per gram of salt	C_2O_4 per gram of salt	Molar ratio	
				C_2O_4/TiO	TiO/Ba
	Mole	*Mole*	*Mole*		
I [a]	2.107×10^{-3}	2.261×10^{-3}	4.534×10^{-3}	2.005	1.073
	2.089	2.278	4.566	2.004	1.090
II [b]	2.055	2.313	4.632	2.003	1.126
	2.095	2.273	4.549	2.001	1.085
III [c]	2.113	2.226	4.462	2.004	1.053
	2.158	2.231	4.471	2.004	1.034
	2.210	2.223	4.449	2.001	1.006

[a] Prepared from the sodium titanium oxalate.
[b] Prepared from the potassium titanium oxalate.
[c] Prepared from the ammonium titanium oxalate.

The results show that in each salt the mole ratio of titanium to oxalate was 1 to 2, within the limits of experimental determination. However, in each salt the mole ratio of barium to titanium was not 1 to 1, but the titanium was always in excess. Samples of each preparation were ignited at 900° C. The ignition products of the salts formed from the potassium salt dissolved completely when treated with hydrochloric acid, as previously described, and the solutions were found to contain potassium. A similar situation existed in the case of the sodium product. The ignited products of the salts formed from the ammonium salts did not dissolve completely, but left a white insoluble residue, which was undissolved titanium oxide.

The explanation of these observations is that some of the barium in the $BaTiO(C_2O_4)_2 \cdot 4H_2O$ is replaced by the alkali element. In the cases of sodium and potassium these elements are not lost on ignition but form Na_2TiO_3 and K_2TiO_3, which are soluble in solutions of hydrochloric acid. This is not the situation with the ammonium compound. In this case it is TiO_2 and not $(NH_4)_2TiO_3$ that is formed on ignition. This ignited TiO_2 is not soluble in hydrochloric acid. The observation was made that if the number of moles of basic constituents in the ignited titanates is equal to or greater than that of the acid constituents, the titanates will be soluble in solutions of hydrochloric acid.

5. Preparation of Barium Titanate of High Purity

In preparing barium titanate of high purity, highly refined titanium tetrachloride, specially purified strontium-free barium chloride, and specially purified oxalic acid were used. To ascertain whether reagent grade barium chloride and reagent grade oxalic acid, complying with the specifications of the American Chemical Society, would be suitable, barium titanate was likewise prepared from these reagents. The only difference between the products, when tested spectrochemically, was that the one prepared with reagent chemicals was found to contain a small amount of strontium estimated qualitatively to be between 0.01 and 0.1 percent.

If one desires a product free of strontium, the barium salt used must be specially purified to remove strontium before making the barium titanyl oxalate.

6. References

[1] Gmelins Handbuch der Anorganischen Chemie, Titan **41**, 455 (1951); based on original work of E. Péchard, Compt. rend. **116,** 1513 (1893) and of A. Rosenheim and O. Schütte, Z. anorg. Chem. **26,** 253 (1901).

[2] W. S. Clabaugh, R. T. Leslie, and R. Gilchrist, J. Research NBS **55,** 261 (1955) RP2628.

WASHINGTON, February 1, 1955.

Journal of Research of the National Bureau of Standards Vol. 56, No. 5, May 1956 Research Paper 2678

A Five-Band Recording Spectroradiometer

C. S. McCamy

In a project[1] undertaken to determine the properties of flames that might be utilized in the detection of accidental fires in aircraft engine compartments, an instrument was constructed to measure and record the radiant energy emitted by flames in five separate wavelength regions from 0.23 to 2.5 microns. The radiant intensity of several types of hydrocarbon flames was determined in each spectral region. The frequency distribution of the fluctuations in the radiant intensity (flicker) was also determined.

1. Introduction

An accidental fire in an aircraft engine compartment can be dealt with successfully only if the fire is detected within a few seconds after it starts. Many methods of detecting such fires have been devised but most of them have been unsatisfactory, primarily because of inadequate coverage and false alarms. Because it is so difficult to predict where accidental flames will strike, devices that require flame contact can be properly placed only after actual fire test in a typical installation. Because accidental fires may occur in many places, an excessive number of such detectors is required for adequate coverage.

Devices that respond to the radiant energy from flames have received considerable attention because a single unit can detect fires anywhere within a large space. Such detectors must, of course, be able to discriminate between the radiant energy from flames and that from the sun or hot engine parts. To accomplish this, the use of two characteristics of flame radiation has been proposed: the spectral distribution of the energy and the fluctuations in the radiant intensity known as "flicker."

Most accidental engine fires involve the burning of hydrocarbons. Although most of the radiation from the flames is in the near infrared, there is a small amount in the visible spectrum and in the ultraviolet. Because hot engine parts radiate practically no energy in the ultraviolet, and because the ozone in the earth's upper atmosphere filters out solar radiation of wavelengths below 0.29 μ, this region is free of interference from these sources. A detector employing a Geiger-Müller-type photon counter, which is sensitive in a part of this spectral region only, has been patented [1].[2] However, difficulties such as the ultraviolet absorptance of the oil films inevitable in engine spaces have, so far, prevented the use of this part of the spectrum.

The characteristic flicker of flames has been used to distinguish them by another system that operates in the near infrared [2]. Unfortunately, the effectiveness of the lead-sulfide cell used to detect radiation in this system is greatly diminished at the high ambient temperatures encountered in engine spaces.

It appeared that other parts of the spectrum or other flame characteristics might be found more useful. In order to explore some of the possibilities, an instrument was built to record the radiant intensity of flames in several broad regions of the spectrum and to determine the frequency distribution of the flicker in each region.

2. Design Considerations

Five regions of the spectrum were selected on the basis of the following considerations: Because even a thin layer of air absorbs practically all ultraviolet radiation at wavelengths shorter than 0.18 μ, this region appeared to be of no significance in fire detection. The region just below 0.29 μ was of particular interest because, as noted earlier, it is practically free of solar and thermal-radiation interference. Hence, one of the regions chosen was that between 0.23 and 0.29 μ. Two regions were selected in the visible spectrum, the blue region from 0.41 to 0.55 μ and the yellow region from 0.55 to 0.70 μ. These were selected so that the instrument might differentiate between blue flames, which usually occur when the fuel is premixed with air, and yellow flames, which usually occur when the air is merely allowed to diffuse into the flame. The infrared region selected extended from the red end of the visible spectrum, 0.70 μ, to the long wavelength limit of sensitivity of the sensing element, 2.5 μ. The remaining ultraviolet region from 0.30 to 0.41 μ was used to complete the spectrum from 0.23 μ in the ultraviolet to 2.5 μ in the infrared. Because the sensitivity of most of the available high-speed photosensitive devices was limited to the five selected regions, it was there that immediate practical applications seemed most likely, even though most of the energy radiated by flames is in the infrared at wavelengths beyond 2.5 μ [3]. Instruments were set up to record the five response signals simultaneously and to measure the frequency and amplitude of the flicker.

The general functional design of the whole instrument is indicated in the block diagram, figure 1.

[1] This work was sponsored by the Wright Air Development Center, Air Research and Development Command.

[2] Figures in brackets indicate the literature references at the end of this paper.

379949—56——4

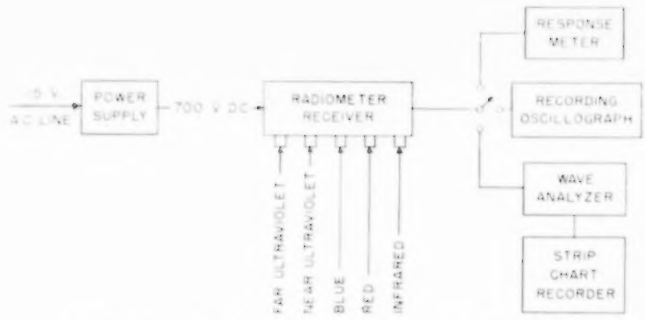

FIGURE 1. *Block diagram of spectroradiometer.*

3. Radiometric System

The receiver consisted of the radiation detectors, resistors for the voltage supply, and optical filters to isolate the wavelength regions, all in a compartmented enclosure. A rear view of the receiver with the back cover removed is shown in figure 2. The sensitive areas of the detectors were placed close together so that a radiant source could be viewed from nearly the same direction by all of them.

Four of the detectors were RCA type 1P28 photomultiplier tubes, the other, used for the infrared region, was a Kodak Ektron, type I, lead sulfide photoconductive cell with a 4- by 4-mm sensitive area.

All of the filters were commercially available except the one for the region from 0.23 to 0.29 μ. This one was made up of three liquid solutions in fused-quartz cells and a glass filter, as follows: (1) 2 cm of an aqueous solution containing 30 g of nickel sulfate per 100 ml, (2) 1 cm of an aqueous solution of 5×10^{-5} molar 4,4′-diaminobenzophenone, (3) 1 cm of an aqueous solution containing 20 mg of 1,4-diazepine-2,3-dihydro-5,7-dimethyl perchlorate in 100 ml of solution, and (4) a Corning glass filter, number 7–54.

Kasha [4] used a compound similar to that in the third cell described above to isolate this region but found a small amount of transmission at 0.347 μ. The second liquid cell mentioned above was used here to eliminate a corresponding defect at 0.355 μ. There was no significant change in transmittance of the filter during 1 year of use.

A Photovolt filter, No. 5264, was used for the region 0.30 to 0.41 μ; two Corning filters, Nos. 5–56 and 3–73, were used for the 0.41- to 0.55-μ region; a Corning 3–67 filter covered the 0.55- to 0.70-μ region; and a Photovolt filter, No. 5263, was used for the region from 0.70 to 2.5 μ.

These filters with the corresponding detectors produced the relative spectral responses shown in figure 3.

The field of view of each of the sections of the instrument was measured. The field angle was defined as the angle subtended at the receiver, in a plane with the normal to the center of the filter, between the opposite positions of a small source angularly displaced to reduce the response to 90 percent of the maximum value. In some cases, the field angle in some planes was greater than the minimum values given below. The field angle for the liquid filter system was about 13°, that for the photomultipliers with glass filters was about 22°, and that for the infrared system was about 30°.

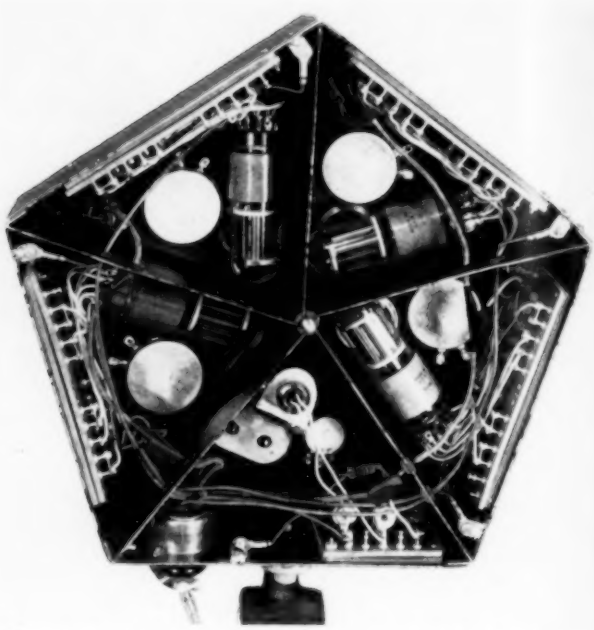

FIGURE 2. *Spectroradiometer receiver, rear view of interior.*

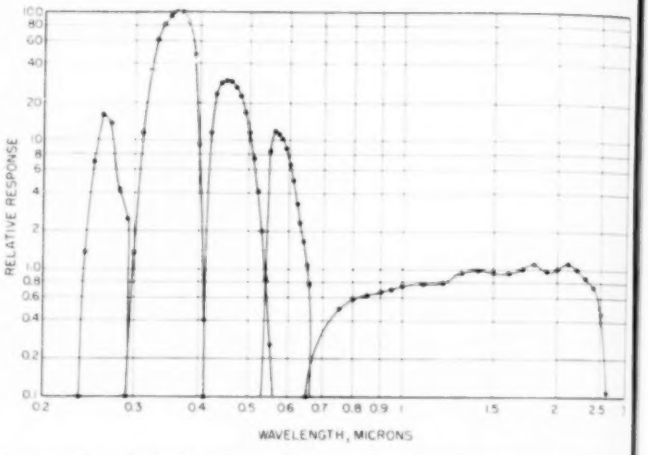

FIGURE 3. *Relative spectral response of the spectroradiometer.*

The circuit diagram of the receiver and power supply is given in figure 4. The high-voltage (plate) transformer was shielded from the other components of the power supply and the connections to this transformer and all output leads were shielded to prevent induced interference. The power supply provided a potential difference of 700 v, d-c, with an alternating component of less than 0.001 percent.

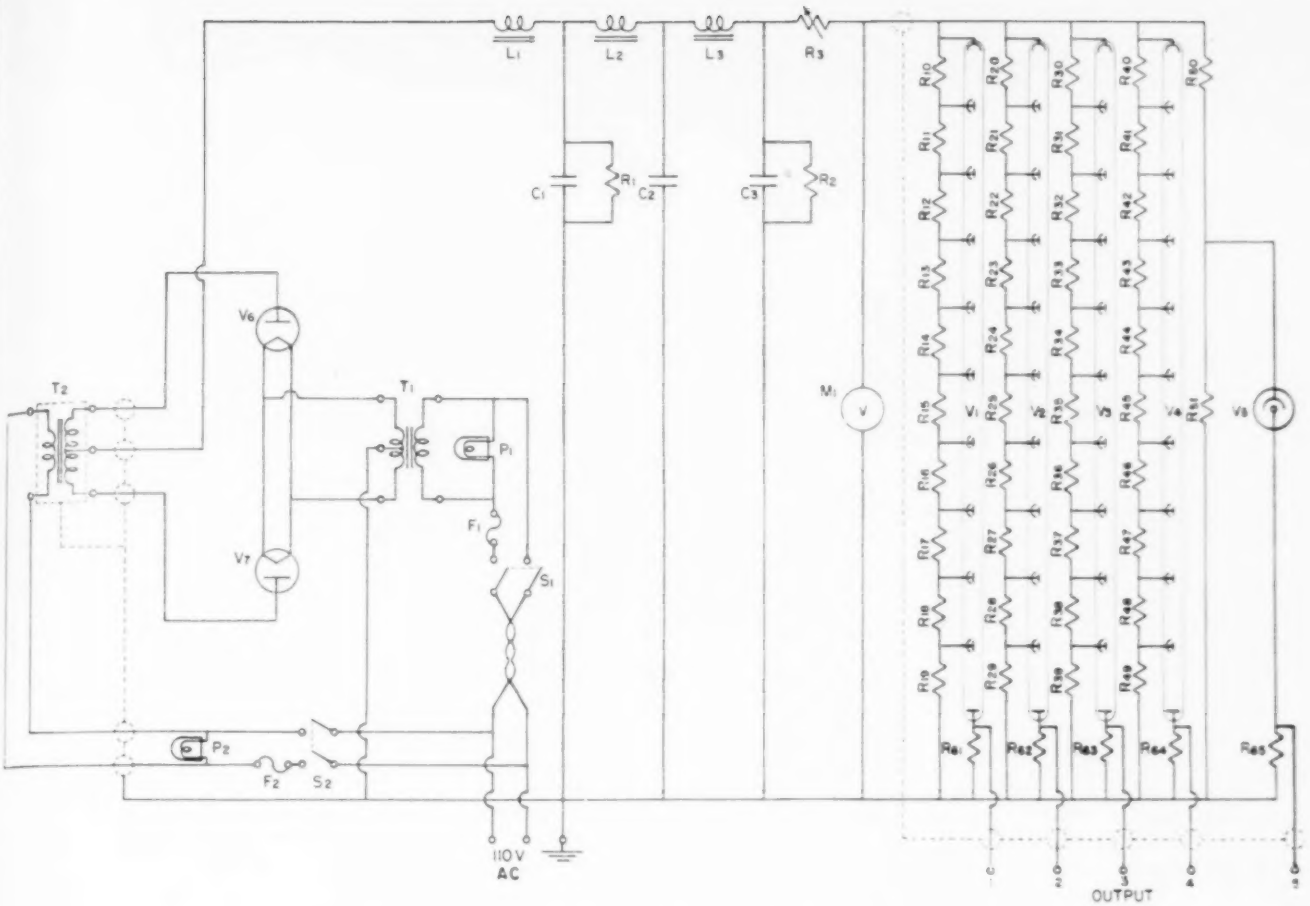

FIGURE 4. *Circuit diagram of power supply and receiver.*

C_1=9 μf.
C_2=8 μf.
C_3=16 μf.
F_1=¾-amp fuse.
F_2=2-amp fuse.
$L_{1,2,3}$=30 h, 35 ma dc, 2-kv insulation.
M_1=0 to 1,500-v d-c meter.
$P_{1,2}$=3-w, 120-v panel lamps.
R_1=4.9 megohms.
R_2=10 megohms.
R_3=0 to 10,000 ohms.
$R_{10,11,12,14,15,16,17,18}$=20,000 ohms.
$R_{27,21,22,24,25,26,27,28}$=20,000 ohms.
$R_{30,31,32,34,35,36,37,38}$=20,000 ohms.
$R_{40,41,42,44,45,46,47,48}$=20,000 ohms.
$R_{19,29,39,49}$=39,000 ohms.
$R_{13,23,33,43}$=11,000 ohms.
R_{50}=348,000 ohms.
R_{51}=40,000 ohms, 1 percent, 1 w.
$R_{61,62,63,64}$=510 ohms.
R_{65}=400,000 ohms, ½ percent, 1 w.
$S_{1,2}$=dpst toggle switch.
T_1=2.5-v center tap filament transformer, 10 amp.
T_2=plate transformer 700-0-700 v, 180 ma.
$V_{1,2,3,4}$=1P28 photomultiplier tubes.
V_5=Kodak Ektron PbS cell, 4×4 mm.
$V_{6,7}$=866A rectifier tubes.

4. Auxiliary Equipment

4.1. Measuring Equipment

The block diagram of the instrument shown in figure 1 indicates several ways in which the radiometric response potentials were utilized.

The potentials could be read directly, one at a time, on a suitable millivoltmeter. This method was used during the preparations for experiments and during the radiometric calibration procedure.

In order to obtain a permanent record of the instantaneous values of all five response signals simultaneously, the signals were put into a recording oscillograph [5]. This instrument was essentially a row of 2-in. cathode-ray oscilloscopes facing a camera in which 35-mm film was continually exposed as it moved at a constant speed of about 2 in./sec. at right angles to the deflection of the spots on the tubes. A continuous trace was produced for each of the response signals. The output of a fixed-frequency oscillator was connected with one cathode-ray tube to provide a time scale. A sample of the record film is shown in figure 5. (On the film shown, the radiant energy indicated on trace E was so small that the instrument noise appeared quite large when the signal was amplified in the recorder.)

In figure 5 it may be seen that the radiant energy in the five wavelength regions fluctuated with practically the same fundamental frequency. For this reason, the flicker frequency was analyzed in only one region, the infrared region, where most of the energy was found. The response potential was applied to a General Radio type 762-B Vibration Analyzer having a frequency range 2.5 to 750 cps. To facilitate the determination of the average amplitude for each frequency, the output of the wave analyzer was continuously recorded. The effect of flicker frequency on the response of the infrared radiometric system was measured. The response

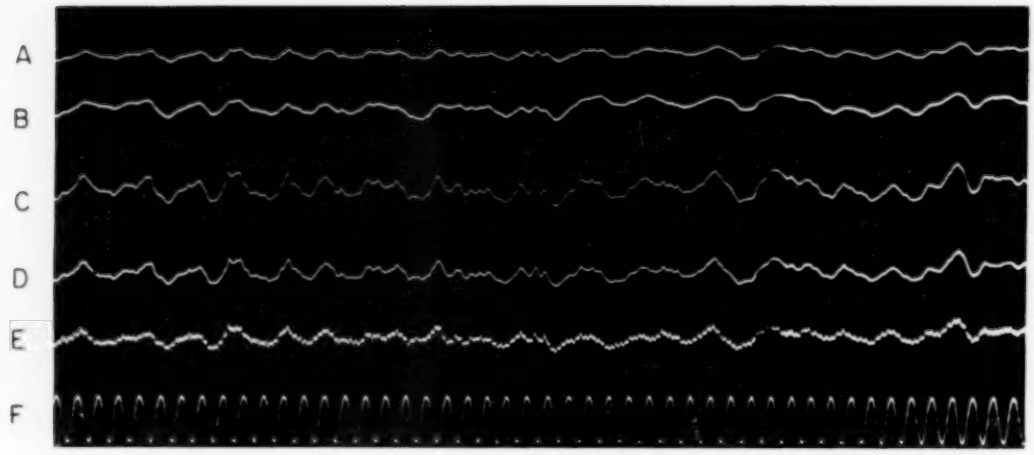

FIGURE 5. *Oscillograph record of variations in radiant intensity in five wavelength regions.*
A, 0.70 to 2.5 μ; B, 0.55 to 0.70 μ; C, 0.41 to 0.55 μ; D, 0.30 to 0.41 μ; E, 0.23 to 0.29 μ; F, 40-cps timing trace.

was found to be essentially constant from 1 to 50 cps, and to diminish smoothly to 85 percent at 133 cps and 30 percent at 1,700 cps.

4.2. Burners and Fuels

The burner used in most of the work was an open stainless-steel cylinder 6 in. in diameter and 2 in. deep, with a water-cooled brass bottom. Liquid fuel was introduced through an inlet in the bottom and the fuel level was maintained automatically. The vapor on the free surface of the liquid fuel mixed with the air by natural diffusion as it burned. The fuels used in this burner were 80 octane gasoline, 100/130 aviation gasoline, Air Force Nos. 1010 and 1100 lubricating oils, and petroleum base hydraulic fluid, Mil Spec 0–5606. A 30-in. fan was used to produce wind speeds up to 20 mph at the burner. The areas of these flames projected on a vertical surface, as viewed by the receiver, were estimated to range from 200 to 600 cm^2.

Some flames were produced in a ram-jet-type burner, which premixed the vaporized fuel and air and preheated the mixture or injected liquid fuel into preheated air. The fuels were 80 octane gasoline, 100/130 aviation gasoline, and JP–4 jet engine fuel. It was estimated that the projected areas of the jet burner flames, as viewed by the receiver, ranged from 1,000 to 2,500 cm^2.

5. Radiometric Calibration

The relative spectral response of each of the cells, installed in the instrument without a filter, was measured with a double-quartz-prism spectroradiometer. The relative spectral response of the instrument with a filter (fig. 3) was found by multiplying the relative response of the cell by the transmittance of the filter at each wavelength.

The variation of the response with the irradiance at the receiver was measured. The average deviation from proportionality over the range used was 1.5 to 3 percent of full scale for the four photomultiplier tubes and 4 percent for the lead sulfide cell. To reduce the effect of nonlinearity when the intensities of sources were compared, the viewing distances were chosen so the deflections were approximately the same.

The quantitative significance of the oscillograph deflections was determined by calibration with respect to a standardized mercury-vapor lamp, a General Electric type H 100–A4. The 0.365-μ line, used to calibrate the photomultiplier tubes, was isolated with a Corning 5860 filter. The 0.578-μ line, used to calibrate the lead sulfide cell, was isolated with a combination of Corning 4784 and 3480 filters.

The intensity of the flame was compared to that of an incandescent lamp, and later the intensity of the incandescent lamp was compared to that of the standard lamp. This indirect procedure was adopted because the standard lamp, which emitted energy of one wavelength, would affect only one section of the instrument unless the filters were removed, whereas the incandescent lamp, with a continuous spectrum, produced a response in all five sections with the filters in place. With the incandescent lamp, calibration traces could be obtained on the oscillograph for all of the cells quickly and conveniently. The filters were removed for the observations on the standard lamp.

As is always the case in abridged spectroradiometry, no single sensitivity could be assigned for the whole interval covered by a cell without taking into account the relative spectral radiance of the source to be observed. Because the relative spectral radiance of the flames was unknown, it was necessary, for purposes of calibration, to assume some spectral radiance curve. For simplicity of analysis, the radiance was taken to be constant and equal to its average value over the wavelength interval involved. In such a case, the response, computed wavelength by wavelength, is the same as that computed by using the average sensitivity over the wavelength range.

Therefore, the average sensitivity was used for calibration purposes.

If the flame radiance were actually constant with respect to wavelength, the method would be exact. Moreover, it can be shown that if the spectral response of the receiver is symmetrical (a condition roughly approximated in this case in all but one region), the flame radiance need not be constant but merely linearly increasing or decreasing with wavelength. Because diffusion flames, the type usually involved in accidental fires, emit essentially continuous spectra, this method gives results of sufficient accuracy for fire-detector engineering. Measurements on other types of spectra must be interpreted on the basis of the spectral response curves (fig. 3).

6. Experimental Results

6.1. Measured Radiant Intensities

The measured radiant intensities of several flames, in the five wavelength regions, are given in tables 1 and 2. The tables indicate that some intensities were less than the minimum measurable values. The minimum value depended upon the viewing distance, which was adjusted to keep the largest response within the range of proportionality.

6.2. Flicker Frequencies

The flicker amplitude of each flame was recorded for about 20 sec at each of a number of frequencies between 2.5 and 750 cps. The average relative amplitudes, observed at frequencies in the range where there were appreciable amplitudes, are shown for two flames in figures 6 and 7.

In many cases the flicker amplitude had a sharp maximum at some frequency between 3 and 15 cps, and in some cases the peak amplitude was 100 times the average amplitude over the range from 2.5 to 750 cps. In the analysis of one flame that flickered with great regularity, second and third harmonics were observed (see fig. 6). None of the flames observed had appreciable flicker amplitude at frequencies above 150 cps, and the jet flames were the only ones having any significant part of the distribution above 25 cps. The distributions for the diffusion flames had sharper peaks and higher relative maxima than those for the premixed flames. The most broadly and evenly distributed flicker curves were those for the premixed jet flames, which had maxima only 3 or 4 times the average over a 100-cps band. A wind over the burner increased the amplitude and frequency of flicker of flames on the surface of liquid fuels. The principal flicker maxima were observed at frequencies between 3 and 10 cps for flames on liquids and between 5 and 25 cps for the jet flames.

The ratio of flicker amplitude to the average radiant intensity was determined by measuring the root-mean-square value of the alternating component and the average direct component of the output of the spectroradiometer and taking their ratio. For burning liquids, this ratio ranged from 0.25 for a gasoline fire in a closed room to 0.41 for a hydraulic-fluid fire in 20-mph wind. The ratio ranged from

TABLE 1. *Radiant intensity of various premixed flames in the jet burner*

Fuel-air ratio	Fuel rate	Fuel-air mixture		Flame couple	Radiant intensity (watts per steradian)				
					0.23 to 0.29 μ	0.30 to 0.41 μ	0.41 to 0.55 μ	0.55 to 0.70 μ	0.70 to 2.5 μ
Gasoline and air premixed and preheated									
	lb/min	*° F*	*ft/sec*	*° F*					
0.0473	1.41	300	137	2,520	0.0026	0.059	0.046	<0.001	21
.0479	4.53	300	397	2,290	.0061	.14	.090	<.001	14
.0702	6.60	300	397	3,390	.028	1.0	.95	.50	(a)
.1062	3.27	300	144	2,810	.032	0.78	.98	.51	(a)
.0984	6.60	300	294	3,150	.037	1.2	1.9	1.04	157
Gasoline injected into preheated air									
0.0460	2.32	[b]113	[b]171	2,150	0.18	0.26	0.49	3.2	233
.0471	3.14	115	221	2,600	.20	.27	.52	2.3	175
.0470	4.43	121	301	2,859	.21	.61	.70	1.7	265

[a] Not measured. [b] Air temperature and velocity.

TABLE 2. *Radiant intensity of various diffusion flames in the six-inch cylindrical burner*

Fuel	Fuel rate	Wind speed	Radiant intensity (watts per steradian)				
			0.23 to 0.29 μ	0.30 to 0.41 μ	0.41 to 0.55 μ	0.55 to 0.70 μ	0.70 to 2.5 μ
	lb/min	*mph*					
Gasoline	0.053	0	$<1\times10^{-4}$	2.2×10^{-2}	0.21	2.1	21
Do	.16	20	$<1\times10^{-4}$	1.8×10^{-2}	1.5	4.3	176
Hydraulic fluid	.017	0	$<1\times10^{-4}$	$<1\times10^{-3}$	0.0032	0.71	237
Do	.072	20	$<1\times10^{-4}$	2.6×10^{-2}	.095	5.2	303
1100 lube oil	.025	0	$<1\times10^{-4}$	6.7×10^{-3}	.0087	0.22	31
Do	.030	10	$<1\times10^{-4}$	1.8×10^{-2}	.88	5.0	135

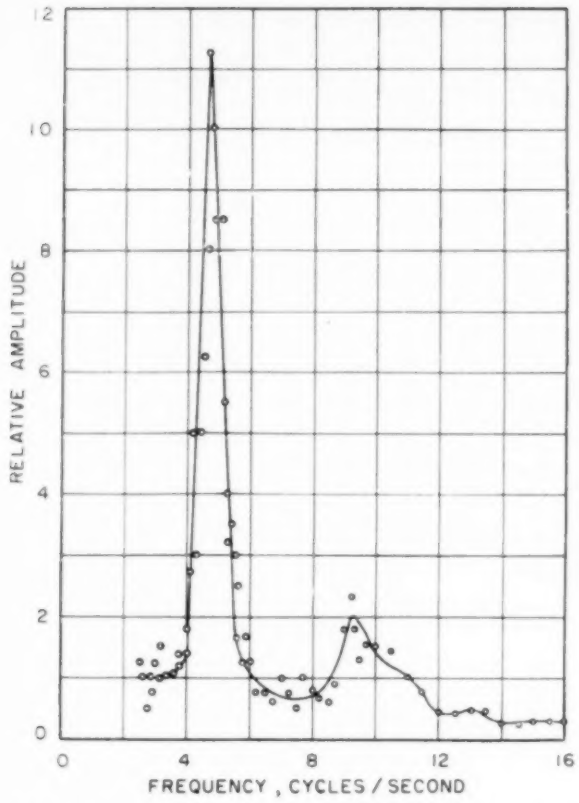

FIGURE 6. *Wave analysis of natural-gas diffusion flame.*

0.05 to 0.15 for premixed jet flames and from 0.1 to 0.3 for the flames resulting from liquid-fuel injection.

6.3. Rate of Increase of Radiant Intensity

The rate of increase in the infrared radiant intensity, just after ignition, was measured, using diffusion flames on gasoline and hydraulic fluid in the 6-in. burner. Figure 8 shows a typical record of the radiant intensity of a gasoline diffusion flame from the instant of ignition, together with a 40-cps timing trace. The first maximum occurred about 0.2 sec after ignition of gasoline fires and about 0.3 sec after ignition of hydraulic-fluid fires. In many cases the successive maxima increased gradually for a few seconds, presumably as a result of an increased rate of evaporation of the liquid fuel upon heating.

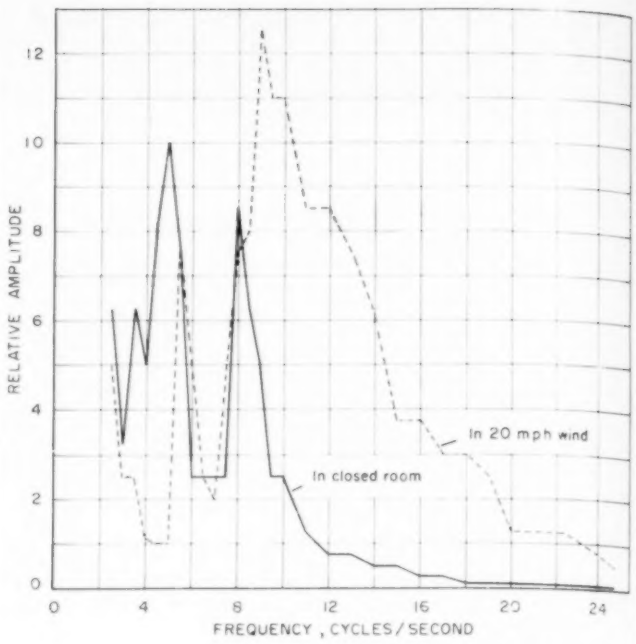

FIGURE 7. *Wave analysis of gasoline diffusion flame.*

Generally, the first recorded maximum value was about the same as the average steady-state value; consequently, the approximate initial rate of increase in the radiant intensity may be calculated by dividing the values reported in table 2 by 0.2 in the case of gasoline or 0.3 in the case of hydraulic fluid.

Using a radiation pyrometer [6] as a receiver, and Pyrex, quartz, and fluorite lenses and filters, some measurements were made in the spectral regions extending to 2.5, 3.6, and 9.5 μ. Only about 10 percent of the energy from premixed flames and 30 to 50 percent of the energy from diffusion flames was found in the region covered by the spectroradiometer. This must be kept in mind when considering the data presented here.

The observation that the flicker occurs in the various regions of the spectrum with practically the same amplitude and frequency indicates that flicker detectors need not necessarily operate in a restricted wavelength interval. The ratio of the flicker amplitude to the average radiant intensity should be of value in the design of flicker discriminating cir-

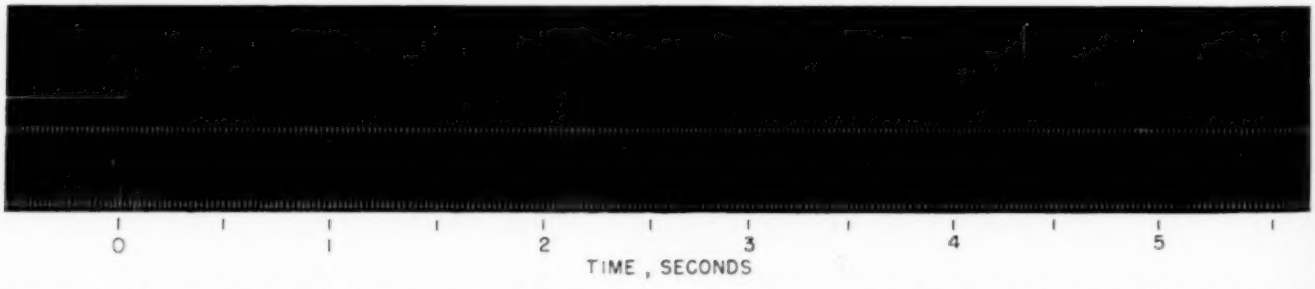

FIGURE 8. *Oscillograph record of radiant intensity of a gasoline diffusion flame during several seconds after ignition and a 40-cps timing trace.*

cuitry. Information concerning the amount of energy in the various parts of the spectrum should aid in designing for discrimination on the basis of spectral distribution. The characteristic rate of increase in radiant intensity upon ignition of the fires studied appears to be a valuable discriminating criterion heretofore overlooked.

Although the instrument described was designed, built, and used to solve a particular problem, its rapid response and the ease with which the wavelength regions could be changed suggest the possibility of its application to other problems. By the use of narrow-band filters, the instrument could produce a continuous record of the intensity of selected spectral lines or bands. With suitable broadband filters for the visible region, the instrument could be used to obtain data on rapidly changing color phenomena. The ultraviolet sensitivity of the instrument suggests possible applications in fluorescence measurements.

Among those who assisted with this work were C. F. Mijal, who synthesized the perchlorate used in the liquid filter, and W. F. Roeser, the leader of the project of which this work was a part.

7. References

[1] P. B. Weisz, Automatic fire alarm, U. S. Patent No. 2,507,359 (May 9, 1950).
[2] E. D. Reddan, Electronic eye spots engine fires, Aviation Age **24,** 150 (Oct. 1955).
[3] A. G. Gaydon and H. G. Wolfhard, Flames (Chapman and Hall, Ltd., London, 1953).
[4] M. Kasha, Transmission filters for the ultraviolet, J. Opt. Soc. Am. **38,** 929 (1948).
[5] The Naval Ordnance Laboratory six-trace cathode-ray oscillograph, AIEE Technical Paper 48–217.
[6] Temperature, its measurement and control in science and industry (Reinhold Publishing Corp., New York, N. Y., 1941).

Washington, January 9, 1956.

Journal of Research of the National Bureau of Standards Vol. 56, No. 5, May 1956 Research Paper 2679

Polarographic Determination of Lead and Cadmium in Zinc-Base Alloys, Using Electrolytic Separations at Controlled Potential

John K. Taylor and Stanley W. Smith

A method is described for the polarographic determination of lead and cadmium in zinc-base alloys. It involves the separation of the metals from the zinc by electrolysis at controlled potential, using a mercury cathode. Fresh electrolyte is substituted for the residual solution and the metals are anodically redissolved from the mercury by controlled-potential electrolysis and determined by polarographic measurement. For lead and cadmium contents of a few ten-thousandths of a percent and greater, the determinations can be made with the usual precision of polarographic measurements.

1. Introduction

The determination of lead and cadmium in spelter and zinc-base alloys, in many cases, is most conveniently and accurately performed by polarographic methods. Several procedures of this type have been described [1, 2] [1] and a method has been recommended by the American Society for Testing Materials [3].

All of the published methods are inapplicable when the copper content of the sample greatly exceeds that of lead and cadmium, because the copper wave precedes the waves of these metals and interferes with their determination. Methods have been described previously in which copper is made nonreducible by formation of the cyanide complex [4] or precipitated as copper acetylide [5], but these have not proved to be entirely satisfactory in the application described in this paper.

Even for alloys of low-copper content, the existing methods have a serious disadvantage when very small amounts of the metals are to be determined. In this case, it is necessary to increase the size of the sample and decrease the final volume of the test solution to obtain greater concentration of the metals and hence increased sensitivity. It is obvious that the concentration of zinc salts in the test solution will vary directly with the size of sample and inversely with the final volume of the solution. For example, the concentration of zinc salts will be 1.2 molar if a 2-g sample is contained in 25 ml, but 3 molar if the final volume is 10 ml. Such large variations in the composition of the supporting electrolyte have a considerable effect on the diffusion-current constants of lead and cadmium [6] causing the calibration factor to vary with the size of sample.

The difficulties described above can be avoided and increased sensitivity can be obtained by separating the metals to be determined from the zinc by electrolysis at controlled potential, using a mercury cathode. When electrolysis is complete, the electrolyte may be discarded and the metals may be anodically dissolved in a suitable volume of the supporting electrolyte. By proper selection of the potential, any interfering copper can be retained in the mercury anode and subsequently dissolved in a suitable electrolyte for polarographic determination.

[1] Figures in brackets indicate the literature references at the end of this paper.

2. Experimental Details

Polarographic measurements were made by using a Sargent model XII photographic-recording polarograph and a Sargent model XXI pen-recording instrument. Electrolyses at controlled potential were performed using the potentiostat described by Greenough, Williams, and Taylor [7]. The electrolysis cell used is shown in figure 1. The cathode consisted of a pool of mercury, and the anode was a cylinder of platinum gauze. A small motor-driven stirrer was located at the mercury-solution interface to minimize concentration-polarization effects. The

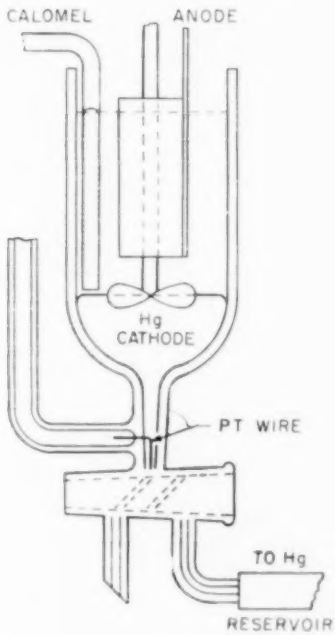

FIGURE 1. *Cell used for electrolysis with mercury cathode at controlled potential.*

saturated-calomel reference electrode used was provided with an agar plug saturated with potassium chloride at the junction tip. This tip was placed close to the mercury-pool electrode to minimize *iR* corrections.

The cell was provided with a platinum contact located as close as possible to the drain stopcock. It was thus possible to maintain electrical connection until virtually all of the mercury was drained. This is necessary to prevent partial resolution of electrolyzed material during the draining process. The capacity of the cell was 50 ml, with a minimum usable volume of about 20 ml. A polyethylene sheet provided with holes for introducing the stirrer and electrodes served as a cover to minimize loss of solution by spraying.

Solutions for calibrating the polarographic measurements were made by dissolving appropriate quantities of the pure metals. NBS Standard Samples and previously analyzed alloys were used to test the precision of the method.

All polarographic measurements were made by using comparative methods [6].

3. Procedure

The sample is dissolved in hydrochloric acid with the addition of a small amount of nitric acid or hydrogen peroxide, if necessary, to ensure complete solution. After boiling the solution to remove oxides of nitrogen (if present), it is cooled and transferred to the electrolysis cell. Approximately 0.1 g of hydrazine dihydrochloride is added to serve as an anodic depolarizer [8]. The calomel electrode is inserted as already described, the potentiostat is connected, and the electrolysis is performed at a cathode potential of 0.9 v with respect to the saturated calomel electrode. This effectively separates the copper, lead, cadmium, and tin from zinc, which remains in the solution. Upon completion of the electrolysis, the current decreases to a small constant value approaching zero. While electrolysis is maintained, the mercury layer is drained from the cell and collected in a small clean beaker. The residual solution is removed and discarded, after which the mercury is returned to the cell and fresh electrolyte is introduced. This solution contains sufficient potassium chloride to make the final solution 0.1 *N* with respect to this salt. In addition, a few milligrams of hydrazine dihydrochloride are added to serve as a depolarizer to prevent the deposition of lead on the platinum electrode. The electrical connections are made as before but with the potential of the mercury electrode regulated to anodically dissolve the desired metals. At a potential of 0.35 v with respect to the reference electrode, lead and cadmium will be stripped quantitatively from the amalgam, and copper will be retained in the mercury.

After electrolysis is complete, the solution is removed as described above and is prepared for polarographic examination. The solution is transferred to a volumetric flask, sufficient gelatin (maximum suppressor) is added to make the final solution 0.01 percent in this constituent, and the solution is diluted to volume. The polarograms are recorded and evaluated in the usual manner.

If it is desirable to determine copper, the residual mercury from above may be returned to the cell and electrolyzed in a similar manner to redissolve this metal. The supporting electrolyte and procedure recommended by Lingane [9] are useful in the determination of copper.

Tin is not reducible in the supporting electrolyte described above and hence does not interfere with the determination of lead. If the tin content of the alloy is of interest, the solution from the final electrolysis may be treated according to the method of Lingane [10]. For small amounts of tin, however, it is necessary to increase the size of the sample rather than to concentrate the solution from the final electrolysis, as tin is lost by volatilization during this process.

4. Discussion

The accuracy and precision of the method are illustrated by the results shown in table 1. The samples analyzed, 108 and 94b, are NBS Standard Samples and contain the percentages of lead and cadmium shown. The amounts of copper in 94b and 108 were 1.01 and 0.0004 percent, respectively. Additions of large amounts of copper to solutions of sample 108 prior to electrolysis were without effect on the determined values of lead and cadmium.

TABLE 1. *Determination of lead and cadmium in zinc-base alloys*

	Pb in—		Cd in—	
	Sample 108	Sample 94b	Sample 108	Sample 94b
	%	%	%	%
Present	0.047	0.006	0.092	0.002
Found 1	.0470	.0056	.0918	.0025
Found 2	.0484	.0050	.0925	.0022
Found 3	.0461	.0056	.0898	.0026
Average	.0472	.0054	.0914	.0024
Average deviation	±.0008	±.0003	±.0010	±.0002

The method has been used for the determination of lead and cadmium in six zinc-base die-casting alloys to be used as standard samples for spectrographic analysis. The lead and cadmium contents ranged from 0.0006 to 0.010 percent, with copper contents up to 1.5 percent. The results obtained polarographically are in excellent agreement with those obtained by cooperating laboratories using more laborious methods. However, as the reports from all of the cooperating analysts have not been received, a detailed comparison cannot be made at this time.

The accuracy and precision that may be expected depend to a large extent on the design of the cell and on the ability of the operator to make the cathode-electrolyte separations quickly and exactly. It is important in the construction of the cell that the platinum contact wire should come as close as

possible to the stopcock, in order that the electric circuit be complete until nearly all of the cathode is drained. This prevents all but a very small part of the deposited metal from returning to the solution.

The method described, in comparison to many involving preliminary separations, is relatively rapid and requires little attention of the operator. After dissolution of the sample and preparation of the solution, requiring no more than a few minutes, the electrolyses require about 1 hr for completion. The polarographic determination accounts for about ¼ hr, so that about 1½ hr are required for the determination of the two metals in a single sample. As no attention is required during the electrolysis, a number of determinations can be made concurrently, provided more than one potentiostat is available.

The size of sample required varies with its composition, the capacity of the cell, and the final volume of the solution. In this work, it was convenient to use a final volume of 25 ml. A 1-g sample was adequate for Sample 94b. In the case of several of the zinc-base die-casting alloys, it was necessary to concentrate the solution after the electrolysis by evaporation on a steam bath and to adjust the final volume to 10 ml, in order to obtain adequate sensitivity with a 1-g sample.

It is advisable to limit the depolarizer left in the final solution to the smallest amount that will prevent the deposition of lead dioxide on the anode. It has been found that when hydrazine dihydrochloride is present to about 0.2 percent, the lead wave is distorted because of the presence of a maximum, and the cadmium diffusion-current plateau is not flat, making precise measurements difficult in the range of 1 to 10 μg/ml of lead and cadmium in the final solution.

The method of electrolysis at controlled potential recently has received considerable attention by analysts and is now established as an extremely useful technique. The resolution of metal from the cathode as described in this paper does not appear to have been used previously.[2] It would appear to have considerable applicability, especially for those cases in which the residual solution from an electrolysis contains elements that would interfere in subsequent analytical operations. It is limited to operations with the mercury cathode because electrolytic resolution from a platinum electrode would no doubt result in mechanical losses of deposited metal.

[2] Since completion of this experimental work and manuscript, a general paper describing electrolytic stripping has appeared, W. E. Schmidt and C. E. Bricker, J. Electrochem. Soc. **102,** 623 (1955).

5. Summary

A method for the determination of small amounts of lead and cadmium in zinc-base alloys is described. A solution of the sample is electrolyzed at controlled potential, using a mercury pool cathode. The residual solution is replaced by fresh electrolyte and the electrode potential is adjusted so that the separated metals are anodically dissolved from the mercury electrode, and determined by polarographic measurement. This method permits the determination of lead and cadmium in these alloys, down to a few ten-thousandths of a percent, with the usual polarographic precision.

6. References

[1] R. C. Hawkins and H. G. Thode, Ind. Eng. Chem., Anal. Ed. **16,** 71 (1944).
[2] W. Kilian, Analyse der Metalle, Bd. I, p. 442, Schiedsverfahren, Springer, Berlin (1942).
[3] ASTM Methods of Chemical Analysis of Metals, p. 428 (American Society for Testing Materials, Philadelphia, Pa., 1950).
[4] M. Spalenka, Z. anal. Chem. **126,** 49 (1943).
[5] M. Sherman, Foundry **78,** 94 (1950).
[6] J. K. Taylor, Anal. Chem. **19,** 370 (1947).
[7] M. L. Greenough, W. E. Williams, Jr., and J. K. Taylor, Rev. Sci. Instr., **22,** 484 (1951).
[8] J. J. Lingane and S. Jones, Anal. Chem. **23,** 1804 (1951).
[9] J. J. Lingane, Ind. Eng. Chem., Anal. Ed. **16,** 147 (1944).
[10] J. J. Lingane, Ind. Eng. Chem., Anal. Ed. **18,** 429 (1946).

WASHINGTON, February 13, 1956.

U. S. GOVERNMENT PRINTING OFFICE: 1956

Recent Publications of the National Bureau of Standards

Journal of Research of the National Bureau of Standards, Volume **56**, No. 3, March 1956 (RP2656 to RP2662 incl.). Annual subscription $4.00.

Technical News Bulletin, Volume **40**, No. 3, March 1956. 10 cents. Annual subscription $1.00.

Basic Radio Propagation Predictions for June 1956. Three months in advance. CRPL 139. Issued March 1956. 10 cents. Annual subscription $1.00.

Research Papers

*Journal of Research, volume **56**, number 3, March 1956. Single copies of the Journal vary in price. Single copies of Research Papers appearing in the Journal are not available for sale. The Superintendent of Documents, U. S. Government Printing Office, Washington 25, D. C., will reprint 100 or more copies of a Research Paper. Request for the purchase price should be mailed promptly to that office.*

RP2656. Penetration of gamma radiation from a plane monodirectional oblique source. Martin J. Berger.

RP2657. A re-entrant cavity for measurement of complex permeability in the very-high-frequency region. R. D. Harrington, R. C. Powell, and P. H. Haas.

RP2658. Fundamental factors controlling electrical resistivity in vitreous ternary lead silicates. Simon W. Strauss, Dwight G. Moore, William N. Harrison, and Lloyd E. Richards.

RP2659. Some factors affecting the precision of polarographic half-wave potential measurements. John K. Taylor and Stanley W. Smith.

RP2660. Infrared measurements from 50 to 125 microns. Earle K. Plyler and Nicolo Acquista.

RP2661. Surface tension of molten glasses in the system barium oxide-boric oxide-silica. Herman F. Shermer.

RP2662. Relationship between crystal orientation and stress-corrosion cracking in alpha and beta brasses. Hugh L. Logan.

Circulars

C568. High-temperature reactions of uranium dioxide with various metal oxides. S. M. Lang, F. P. Knudsen, C. L. Fillmore, and R. S. Roth. 20 cents.

C569. Fused-quartz fibers. A survey of properties, applications and production methods. Nancy J. Tighe. 25 cents.

Building Materials and Structures Reports

BMS146. Plasticity and water retentivity of hydrated limes for structural purposes. Ernest M. Levin, Walter F. Clarke, and Lansing S. Wells. 15 cents.

BMS144. Supplement. Sound insulation of wall, floor, and door constructions. Richard V. Waterhouse. 5 cents.

Publications in Other Journals

Mechanical impedance of the forehead and mastoid. Edith L. R. Corliss and Walter Koidan. J. Acoust. Soc. Am. (57 E. 55th St., New York 22, N. Y.) **27**, No. 6, 1164 (Nov. 1955).

Ultrasonic switch aids diversity reception. G. Franklin Montgomery. Electronics (330 W. 42d St., New York 36, N. Y.) **28**, No. 11, 1169 (Nov. 1955).

Chromium for gun bores. John P. Young. Am. Rifleman (1600 Rhode Island Ave. NW, Wash. 6, D. C.) **104**, 39 (Feb. 1956).

Automatic computation of nerve excitation. K. S. Cole, H. A. Antosiewicz, and P. Rabinowitz. J. Soc. Indust. Appl. Math. (P. O. Box 7541, Phila. 1, Pa.) **3**, 153 (Sept. 1955).

Ion-atom interchange in air. Roy F. Potter. J. Chem. Phys. (57 E. 55th St., New York 22, N. Y.) **23**, 2462 (1955).

Mathematics. An algebraic proof of the isoperimetric inequality for polygons. Ky Fan, Olga Taussky, and John Todd. J. Wash. Acad. Sci. (U. S. National Museum, Washington 25, D. C.) **45**, No. 11, 339 (Nov. 1955).

Effect of size on the inlet-system dynamics in four-stroke, single-cylinder engines. D. H. Tsai. Trans. ASME (29 W. 39th St., New York 18, N. Y.) **78**, No. 1, 197 (Jan. 1956).

Electrical and optical properties of intermetallic compounds. IV. Magnesium stannide. R. F. Blunt, H. P. R. Frederikse, and W. R. Hosler. Phys. Rev. (57 E. 55th St., New York 22, N. Y.) **100**, No. 2, 663 (Oct. 1955).

Cathode film studies by the drainage method. A. Brenner and G. Wranglen, Sartrych ur Svensk Kemish Tidskrift (Sweden) **67**, 81 (1955).

Progress in metal cleaning and finishing. A. Brenner. Metal Progr. (7301 Euclid Ave., Cleveland 3, Ohio) **68**, No. 3, 113 (Sept. 1955).

Electrodeposition of some of the less common metals from nonaqueous media. A. Brenner. Rec. of Chem. Progress (Kresge-Hooker Sci. Library, Wayne Univ., Detroit 1, Mich.) **16**, No. 4, 241 (1955).

Addition theorems for general Legendre and Gegenbauer functions. Peter Henrici. Waverly Press Inc. (Mt. Royal & Guilford Ave., Baltimore, Md.) **4**, No. 6, 983 (Nov. 1955).

Isotope analysis using dimethylmercury. Vernon H. Dibeler. Anal. Chem. (1155–16th St. NW, Washington 6, D. C.) **27**, 1958 (Dec. 1955).

Distribution of phase diagrams of interest to ceramists. Ernest M. Levin. Bull. Am. Ceram. Soc. (2525 N. High St., Columbus 2, Ohio) **34**, No. 12, 399 (1955).

Measurement of correlation coefficients in reverberant sound fields. Richard K. Cook, R. V. Waterhouse, R. D. Berendt, Seymour Edelman, and M. C. Thompson, Jr. J. Acoust. Soc. Amer. (57 E. 55th St., New York 22, N. Y.) **27**, No. 6, 1072 (Nov. 1955).

Limitations on rapid signal analysis. Edith L. R. Corliss. J. Wash. Acad. Sci. (U. S. National Museum, Washington 25, D. C.) **45**, No. 11, 359 (Nov. 1955).

Computation of vibration modes and frequencies on SEAC. William F. Cahill and Samuel Levy. J. Aeronaut. Sci. (20th and Northampton Sts., Easton, Pa.) **23**, No. 12, 837 (Dec. 1955).

A proposed index of current noise for composition resistors. G. T. Conrad. Proc. 1955 Electronic Components Symposium (8820 Bellanca Ave., Los Angeles 45, Calif.) 118 (1955).

American Dental Association specification No. 13 for self-curing repair resins. J. W. Stanford, Claire L. Burns, and G. C. Paffenbarger. J. Am. Dental Assoc. (222 E. Superior St., Chicago 11, Ill.) **51**, 425 (Oct. 1955).

Stress corrosion cracking of a gold wedding ring. Fred M. Reinhart. Corrosion (919 Milam Bldg., Houston 2, Texas) **11**, No. 12, 15 (Dec. 1955).

Automatic instrument for electron scattering measurements. L. Marton, J. Arol Simpson, and T. F. McCraw. Rev. Sci. Instr. (57 E. 55th St., New York 22, N. Y.) **26**, No. 9, 855 (Sept. 1955).

On the origin of the electronically excited C_2 radical in hydrocarbon flames. R. E. Ferguson. J. Chem. Phys. (57 E. 55th St., New York 22, N. Y.) **23**, 2085 (Nov. 1955).

Negative oxygen ions in the upper atmosphere: The affinity and radiative attachment coefficient of atomic oxygen. L. M. Branscomb and S. J. Smith. Trans. Am. Geophys. Union (1530 P. St. NW, Washington 5, D. C.) **36**, No. 5, 755 (Oct. 1955).

Cryogenics. F. G. Brickwedde, R. P. Hudson, and E. Ambler. Ann. Rev. Phys. Chem. (Annual Reviews Inc., Stanford, Calif.) **6**, 25 (1955).

Thermoelectric power of indium antimonide. H. P. R. Frederikse and Eugenie V. Mielczarek. Phys. Rev. (57 E. 55th St., New York 22, N. Y.) **99**, 1889 (1955).

Publications for which a price is indicated are available only from the Superintendent of Documents, U. S. Government Printing Office, Washington 25, D. C. (foreign postage, one-third additional). Reprints from outside journals are not available from the National Bureau of Standards but can often be obtained from the publishers.

UNITED STATES
GOVERNMENT PRINTING OFFICE
DIVISION OF PUBLIC DOCUMENTS
WASHINGTON 25, D. C.

OFFICIAL BUSINESS

PENALTY FOR PRIVATE USE TO AVOID PAYMENT OF POSTAGE, $300 (GPO)

Journal of Research of the National Bureau of Standards Vol. 56, No. 5 May 1956

Contents

		Page
Characteristics of an image-forming system. Roland V. Shack.	RP2672	245
Advances in the design and application of the radiofrequency permeameter. Alvin L. Rasmussen, Albert W. Enfield, and Alfred Hess.	RP2673	261
A new computer for calculating the water content of gases. A. W. Diniak and E. R. Weaver.	RP2674	269
Vibrational constants of acetylene-d_2. Harry C. Allen, Jr., L. R. Blaine and Earle K. Plyler.	RP2675	279
Heat capacity of polyisobutylene from 0° to 380° K. George T. Furukawa and Martin L. Reilly.	RP2676	285
Preparation of barium titanyl oxalate tetrahydrate for conversion to barium titanate of high purity. W. Stanley Clabaugh, Edward M. Swiggard, and Raleigh Gilchrist.	RP2677	289
A five-band recording spectroradiometer. C. S. McCamy.	RP2678	293
Polarographic determination of lead and cadmium in zinc-base alloys, using electrolytic separations at controlled potential. John K. Taylor and Stanley W. Smith.	RP2679	301

Single copies of the above Research Papers are not available for sale, but the Superintendent of Documents, U. S. Government Printing Office, Washington 25, D. C., will reprint 100 or more copies, and request for the purchase price should be mailed promptly to that Office.

[A list of recent NBS publications is given on page 3 of the cover.]

For sale by the Superintendent of Documents, U. S. Government Printing Office, Washington 25, D. C. Price 40 cents (single copy). Subscription price: $4 a year; $1.25 additional for foreign mailing. Single copies vary in price.

UNITED STATES GOVERNMENT PRINTING OFFICE, WASHINGTON : 1956